A close-up photograph of a micro-fabricated MEMS device on a wafer. The device consists of a grid of small, rectangular structures, each with a central nozzle-like feature. The structures are arranged in a regular pattern and are illuminated with a blue light, highlighting their intricate details. The background is dark and out of focus, showing the edges of the wafer and the surrounding environment.

Department of Precision and Microsystems Engineering

Design, Fabrication and Characterization of MEMS Micro-resistojet Thrusters

Sampuran Inder Singh

Report no : 2023.095
Coach : Dr. Angelo Cervone
Professor : Dr. Murali Ghatkesar
Specialisation : MNE
Type of report : Master's Thesis
Date : 14 November 2023

Sampuran Inder Singh

Design, Fabrication and Characterization of Microresistojet Thrusters

MASTER'S THESIS

submitted to
Delft University of Technology

SUPERVISORS

Dr.Ir. A. Cervone - Supervisor from Department of Space Engineering, Faculteit Luchtvaart- en Ruimtevaarttechniek

Dr. M.K. Ghatkesar - Supervisor from Department of Precision and Microsystems, Faculteit Werktuigbouwkunde, Maritieme Techniek & Technische Materiaalwetenschappen

Dr.Ir. H.W. van Zeijl - Supervisor from Electronic Components, Technology and Materials group, Faculteit Elektrotechniek, Wiskunde en Informatica

EXTERNAL REVIEWERS

Ir. B.T.C. Zandbergen - Department of Space Engineering, Faculteit Luchtvaart- en Ruimtevaarttechniek

Dr.Ir. T. Manzaneque Garcia - Department of Microelectronics, Faculteit Elektrotechniek, Wiskunde en Informatica

Abstract

Small satellites require efficient propulsion systems for attitude and orbit control. This thesis focuses on the development and characterization of two distinct types of micro-resistojet thrusters, namely Vaporizing Liquid Micro-resistojet (VLM) and Low Pressure Micro-resistojet (LPM). Both concepts are developed at TU Delft and are designed to use water as a propellant, conforming to launch-safety, simplicity, and cost-effectiveness criteria.

In VLM, liquid water is vaporized and accelerated through a convergent-divergent nozzle. In contrast, LPM operates by reducing water vapor pressure to below 300 Pa and then accelerating it through expansion slots under a rarefied flow regime. Both types of thrusters are built on Micro-Electro-Mechanical Systems (MEMS) chips to accommodate the size constraints of nano- and pico-satellites.

The thesis introduces refined designs for both VLM and LPM thrusters. Specifically, the VLM design features an optimized nozzle shape and improved inlet flow, while the redesigned LPM assembly is more space-efficient. These modifications increase the thrust-to-size ratio for both thruster types.

The thesis presents a fabrication process for these thrusters, employing an anodic bonded silicon-glass wafer stack with a capped microfluidic channel. Fabrication was executed at the EKL lab, using a simplified manufacturing process that is detailed within the report.

Post-fabrication, the thrusters underwent mechanical and electrical characterization. The results indicate incremental improvements in both design performance and manufacturability. The new VLM design yielded an 18% increase in simulated thrust efficiency, while the new LPM assembly reduced the occupied volume by 31%. These outcomes, along with a comprehensive evaluation of the setup and results, are elaborated upon in this report.

Acknowledgements

Upon the successful completion of this thesis, I bring to a close my academic journey as a Master of Science student in Mechanical Engineering, specializing in High-Tech Engineering, at the prestigious Technical University of Delft. I dedicate this section to acknowledging the instrumental contributions of individuals who have enriched my research experience over the course of this year-long project.

Foremost, I owe a debt of gratitude to my supervisor, Angelo, who introduced me to the compelling domain of microthrusters. His steadfast confidence in my abilities, coupled with his deep-seated expertise in the field, significantly influenced the trajectory and quality of my research. His mentorship proved invaluable in comprehending novel subjects and in adhering to rigorous scientific standards. His prompt and insightful responses to my queries, however trivial, allowed for a conducive dialogue around my work.

I extend my deepest appreciation to Henk, my mentor from EWI, whose involvement was indispensable for the successful fabrication of my thrusters at EKL (Else Kooi Lab). His comprehensive understanding and expertise in MEMS fabrication processes consistently endowed me with nuanced clarity. Project related discussions were not only enjoyable but also stimulating, as we navigated the diverse and challenging facets of my research. His meticulous attention to detail consistently directed my efforts toward meaningful outcomes, guiding me through the intricacies of my work. His presence in the cleanroom and assistance with the various processes were crucial. Remarkably, despite undergoing multiple surgeries over the course of the year, his enthusiastic return to work and sustained energy levels were an inspiration and a delight to collaborate with. I am certain that the project's success is attributable to his unwavering support and expertise.

My gratitude extends to Murali for his influential mentorship. In fact, it was Murali who, in my first year at TU Delft, introduced me to the fascinating world of MEMS and micro-fabrication. Without his counsel, I would likely still be entangled in peripheral tasks related to my work. His seasoned experience and practical guidance not only optimized my research trajectory but also was invaluable in managing my timelines and in formulating contingency plans for anticipated obstacles—a foresight that proved crucial as I encountered the very issues he had predicted. I find myself deeply indebted to him, and I could not have asked for a better mentor.

Acknowledgment is also due to the entire team at EKL, Delft (with special thanks to Silvana, Mario, Johannes, Daniel, Tom, Dylan, and Bianca), for their exceptional support in equipping me with the necessary laboratory skills and resources. The successful fabrication of these components owes a significant debt to the meticulous upkeep of a sterile cleanroom

environment, a task diligently performed by the team. Their cumulative years of expertise greatly expedited my decision-making process, as I could readily consult their seasoned knowledge for optimizing processes and identifying suitable methodologies. Additionally, their willingness to accommodate flexible training schedules on each piece of equipment, as per my requirements, was deeply appreciated.

Finally, I would like to express my heartfelt gratitude to my family back in India who made this journey possible in the first place. Also to my friends of old and those I made during this challenging journey in the Netherlands, for their unconditional support and love throughout this journey. Their unwavering support and encouragement have been the bedrock upon which my academic and personal growth has been founded.

Sampuran Inder Singh

Delft, November 2023

Contents

1	Introduction	1
1.1	Background	2
1.2	Problem Statement and Motivation	2
1.3	Research Objectives	4
1.4	Thesis Outline	5
2	Literature Preliminaries	6
2.1	Propulsion: Terminology and Mathematics	7
2.2	Micro-Spacecraft	8
2.3	Micro-Resistojet thrusters	8
2.3.1	VLM - Vaporizing Liquid Microthruster	9
2.4	MEMS (Micro-Electro-Mechanical Systems)	11
2.5	Summary and Research Gap	12
3	Design of MEMS Vaporizing Liquid Micro-resistojet Thrusters	13
3.1	Introduction	14
3.1.1	Working Principle: Vaporizing Liquid Micro-thruster	14
3.1.2	Design Calculations for Vaporizing Liquid Micro-thruster	15
3.2	Inlet Design for efficient Flow	16
3.3	Acceleration Chamber and Heater Design Selection	17
3.4	Optimized Nozzle Design Selection	18
3.4.1	Convergent Divergent Nozzle	18
3.4.2	Aerospike Nozzle	20
3.5	Results and Summary	21
3.5.1	Inlet Design	21
3.5.2	CD Nozzle Selection	22
3.5.3	Aerospike Nozzle Selection	23
3.6	Conclusion	24
3.6.1	Areas of Improvement	24
4	Fabrication and Characterisation of VLM Microthrusters	26
4.1	Introduction	27
4.1.1	VLM Microthrusters	27
4.1.2	MEMS fabrication of microthrusters	27
4.1.3	Fabrication state of the art	27
4.2	Fabrication of VLM thruster	28

4.2.1	Design for fabrication	28
4.2.2	Wafer Layout and Mask Fabrication	29
4.2.3	Detailed MEMS fabrication process	30
4.2.4	Assembly	31
4.2.5	Fabrication Challenges and Concerns	32
4.3	Mechanical Characterization	32
4.3.1	Methodology for Mechanical Characterization	32
4.3.2	Results for Mechanical Characterization	33
4.4	Electrical Characterization	35
4.4.1	Methodology for Electrical Characterization	35
4.4.2	Results for Electrical Characterization	36
4.5	Discussion	36
4.5.1	Comparison to previously fabricated thrusters	36
4.6	Conclusion	37
5	Low-Pressure Microthruster Design and Fabrication Process	39
5.1	Introduction to Low-Pressure Micro-resistojet Thrusters	40
5.2	Literature Prerequisites for Design of LPM thruster	41
5.3	Design of LPM thruster	43
5.4	LPM thruster - CFD modeling and analysis	43
5.5	Wafer Fabrication Process	45
5.6	Final Design and Discussion - LPM	47
6	Conclusions & Recommendations	48
6.1	Conclusions	49
6.2	Evaluating Research Objectives	49
6.3	Recommendations	51
	References	53
A	Literature	56
A.1	Assumptions	56
A.1.1	Propulsion calculations	56
A.2	Purpose of Propulsion in Micro-Spacecraft	57
A.2.1	Attitude control	57
A.2.2	Drag compensation	57
A.2.3	Station keeping	58
A.2.4	Orbit adjustment	58
A.3	History of Satellite miniaturization	59
A.4	History of VLM Development	61
B	Fabrication	63
B.1	Complete Fabrication Flowchart - New VLM Design	63
C	Charecterization	76
C.1	Backup SEM Images	76
D	LPM and VLM previous Results	87

List of Figures

2.1	Schematic of variables in Propulsion	7
2.2	Schematic of a simple VLM system with feed and thruster components	9
2.3	Parallel multi-shaped channel VLM, 2018	10
2.4	Sensor integrated VLM, 2021	10
3.1	CAD model of proposed microfluidic interface	16
3.2	A possible configuration of the proposed modular microfluidic interface	16
3.3	Serpentine chamber	17
3.4	Micro-Heater shape as developed by Spervovasilis et al.	18
3.5	Convergent Divergent Nozzle Parameters	18
3.6	Mesh generated for a CD Nozzle	19
3.7	CD Nozzle Simulation Convergence	19
3.8	Output plane used for thrust calculation	20
3.9	Aerospike Nozzle Parameters	21
3.10	Velocity distribution in conventional inlet vs. new integrated inlet	22
3.11	Velocity streamlines in conventional inlet vs. new integrated inlet	22
3.12	Pressure drop across conventional inlet vs. new integrated inlet	22
3.13	Value of thrust for all values of CD parameters	22
3.14	Results for CD Nozzle	23
3.15	Results for for optimal Aerospike	24
4.1	Parallel multi-shaped channel VLM, 2018	28
4.2	Inlet Design for VLM	28
4.3	Serpentine Channel dimensions for one section	28
4.4	Mask Image layout	29
4.5	Wafer configuration	30
4.6	Fabrication of VLM thrusters on a Silicon Wafer	31
4.7	SEM - Aluminium bonding pads on Titanium heater on Oxide layer	33
4.8	Aluminum on Titanium morphology	33
4.9	Magnified view of a 50m CD nozzle throat	34
4.10	A serpentine channel inlet for the test wafer	34
4.11	SEM imaging of heater features	34
4.12	Stitched 3D imaging from laser microscope	34
4.13	Roughness measurement - Top surface	34
4.14	Roughness measurement - Etched surface	34
4.15	Dimension Comparison to Design	35
4.16	Some minor defects in the Silica	35

4.17 Schematic of Probe Station	36
4.18 Electrical characterization methodology	36
4.19 Final fabricated wafer	37
4.20 Glass bonded pilot wafer	37
5.1 Schematic of the LPM. Left: the complete system - tank, feed system and thruster. Right: The detailed microchannel and the particle behavior	40
5.2 LPM MEMS Chips	40
5.3 LPM Wafer with large slots chips after manufacturing and dicing process, 2018	41
5.4 CAD model of simple LPM thruster assembly	43
5.5 SCCM or mass flow rate vs Plenum Pressure	44
5.6 Experimental thrust (Appendix D) vs Simulated Thrust of current LPM design	44
5.7 Section plane showcasing MEMS fabrication sequence for LPM thruster	46
5.8 Final LPM Design	47
5.9 Molecular flux across the LPM holes	47
6.1 Render of possible integrated valve to inlet assembly	51

List of Tables

3.1	CFD Simulation Parameters for Evaluating Mi-crochannel Inlet Flow	17
3.2	Maximum temperature of micro-heaters from different materials	18
3.3	CD Nozzle Design Variables	18
3.4	CD Nozzle Parametric Sweep	19
3.5	Parameters to build a model of CD Nozzle	20
3.6	Aerospike Nozzle Design Variables	20
3.7	Aerospike Nozzle Parameter Variation	21
3.8	Performance of selected CD nozzles	23
3.9	Optimized Aerospike Nozzle parameters	24
3.10	Performance of selected Aerospike nozzles	24
4.1	Selected Dimensions for simple CD nozzle	29
4.2	Selected Dimensions for Aerospike nozzle	29
4.3	Root mean Square surface roughness - Top layer	34
4.4	Root mean square surface roughness - Bottom layer	35
4.5	Resistance Measurement - Individual Resistors	36
4.6	Final Results of Charecterization	38
5.1	Effect of reducing Plenum height	45

1 | Introduction

“The further conquest of space will make it possible, for example, to create systems of satellites making daily revolutions around our planet at an altitude of some 40,000 kilometers, and to assure universal communications and the relaying of radio and television transmissions. There is no such thing as an unsolvable problem.”

– Sergei Korolev, 1906-1966

1.1 Background

In recent years, the deployment of nano- and pico-satellites for various space missions has witnessed a surge, elevating the importance of integrated propulsion systems within these miniature spacecraft. Micro-propulsion systems are no longer a mere auxiliary component; they are critical for extending mission longevity, enhancing operational capabilities, and widening the scope of mission objectives. The incorporation of micro-propulsion systems provides a marked increase in satellite functionality by enabling a range of in-orbit operations, such as attitude adjustment, precise positioning, station-keeping, and orbit transfers. In more ambitious projects, micro-propulsion systems even hold the potential to facilitate deep space exploratory missions. A detailed explanation of the purpose of micro-propulsion systems in various miniature spacecraft is included in [section A.2](#).

However, the development of micro-propulsion systems for nano- and pico-satellites presents a complex set of engineering challenges due to stringent size, mass, and power constraints inherent in these classes of spacecraft. The constraint-driven nature of these systems necessitates a multidisciplinary approach involving material science, fluid dynamics, control engineering, and power management. Achieving high performance within these limitations is non-trivial and calls for innovations in micro-system engineering and thruster design. Addressing these challenges requires a comprehensive understanding of both theoretical principles and practical applications of propulsion systems.

The aim of this research is not merely to create a functional prototype. It is to establish a robust framework that will contribute to future advancements in micro-propulsion technology. As nano- and pico-satellites continue to become increasingly crucial in fields like space exploration, scientific research, and telecommunications, the need for efficient, reliable, and scalable micro-propulsion systems intensifies.

This thesis first focuses on a specific type of micro-propulsion system known as Vaporizing Liquid Micro-resistojet (VLM) thrusters. VLM is a micro-resistojet propulsion system that utilizes a resistive heating element to vaporize a propellant, subsequently generating a high-speed jet of exhaust to create thrust. The report provides an optimized design iteration for this thruster, followed by a comprehensive account of its fabrication at EKL Labs, Delft. Lastly, the mechanical and electrical performance of the fabricated thrusters will be characterized. Next, a similar study is carried out for a Low Pressure Micro-resistojet (LPM) thruster. A Low Pressure Microresistojet (or Free Molecule Micro-Resistojet) thruster operates by electrically heating a low pressure propellant to produce high-velocity gas molecules, which are then expelled through a nozzle to generate thrust in the free-molecule flow regime.

1.2 Problem Statement and Motivation

While neither thruster type (neither VLM nor LPM) has reached a level of technical readiness suitable for commercial applications, several critical areas require attention to accelerate development and achieve market viability. This section outlines the priority shortcomings that this thesis aims to study and improve. These focal points constitute the problem statement for this research.

Vaporizing Liquid Microresistojet thrusters have been developed using Micro-Electro-Mechanical Systems (MEMS) technologies. However, several key aspects of these thrusters remain sub-optimal, presenting challenges that affect performance and manufacturability. Specifically:

- **Inlet Flow Dynamics:** The flow characteristics at the thruster inlet have neither been optimized nor rigorously tested, and the current design is frugal and extremely simple with no empirical data or computational fluid dynamics (CFD) analysis.
- **Outlet Nozzle Geometry:** The prevalent mathematical models for nozzle design are inapplicable for MEMS-manufactured VLM thrusters with rectangular cross-sectional nozzles. Existing equations predominantly target cylindrical converging-diverging (CD) nozzles, leaving a theoretical gap for MEMS-appropriate design. The state of the art does not explore if the nozzle geometry is optimized for this application.
- **Manufacturing Process Inefficiency:** The current MEMS manufacturing process for VLM thrusters is complex, involving multiple etching steps, and exhibits significant deviations from the original design specifications. This not only increases production costs but also introduces performance unpredictability.

Optimizing the flow dynamics, nozzle geometry, and manufacturing process for MEMS-based VLM thrusters could lead to significant advancements in micropropulsion technology. The implications extend to various high-impact applications, including nano- and pico-satellites, where size, weight, and power are crucial parameters. Furthermore, these enhancements could reduce manufacturing costs and variability, promoting the adoption of VLM thrusters in a broader range of aerospace applications.

Low-Pressure Micro-Resistojet (LPM) thrusters offer promise in the realm of micropropulsion especially when these thrusters are to be used in parallel with VLM thrusters, yet key challenges remain to be addressed for optimizing their performance and manufacturability. Specifically:

- **Numerical Model for Flow Simulation:** There is a lack of a CFD (computational Fluid Dynamics) model that can accurately simulate the flow characteristics inside LPM thrusters. The existing numerical models are either too generalized or lack the capability to deal with specific geometric conditions, making it challenging to predict thruster behavior accurately.
- **Thruster Size Reduction:** One of the primary design advantages of LPM thrusters is their size. The goal is to minimize the unit's dimensions while still providing sufficient thrust. As of now, the designs have not been optimized in terms of thrust per unit size, and there is potential for improvements that could make them more suitable for integration with other micropropulsion systems.

Addressing these issues could not only enhance the functionality of LPM thrusters but also make them more compatible for use in parallel systems with VLM thrusters. Optimizing the numerical models would allow for better design strategies and more reliable performance predictions. Size optimization would contribute to making these thrusters more versatile and applicable to a broader range of aerospace missions where size, weight, and power are critical factors.

The motivation for this research is twofold:

1. **Technical excellence:** To bridge the existing gaps in the theoretical understanding and practical implementation of MEMS-manufactured VLM thrusters, thereby achieving higher performance standards.
2. **Broad applicability:** To create a robust, cost-effective, and scalable manufacturing process for VLM thrusters, thereby extending their utility in diverse aerospace missions requiring precision and miniaturization.

The proposed thesis aims to address these critical issues through comprehensive research methodologies, combining computational modeling, experimental testing, and process optimization.

1.3 Research Objectives

Based on the Improvement areas and Motivation discussed in the previous section the primary aim of this research is to address the overarching research question:

How can the optimization of flow dynamics, time-effective fabrication techniques, and design fidelity collectively enhance the performance and manufacturing accuracy of MEMS Micro-resistojet thrusters?

To tackle the complexities of this problem, it is divided into the following sub-questions:

SQ1: *What is the quantifiable impact on performance-to-size ratio when flow dynamics are optimized in existing MEMS Micro-resistojet thrusters?*

This sub-question seeks to explore the impact of flow dynamics on the efficiency of MEMS Micro-resistojet thrusters. Utilizing computational fluid dynamics simulations followed by empirical validations, the goal is to quantify the effects of different flow optimizations on thruster performance in relation to size.

SQ2: *What fabrication techniques can be employed to improve time-efficiency and design fidelity in MEMS Micro-resistojet thrusters?*

This investigation explores various manufacturing processes for optimization in terms of cost, time, and fidelity. Techniques such as additive manufacturing, etching, and lithography will be assessed. The objective is to pinpoint methods that meet design specifications without sacrificing accuracy or time-efficiency.

SQ3: *What is the degree of deviation between the manufactured MEMS Micro-resistojet thrusters and their initial design specifications?*

This sub-question focuses on the validation aspect. It aims to quantify the differences, if any, between the designed and fabricated thrusters. Various characterization methods, such as scanning electron microscopy and electric probes, will be employed to assess this.

Successfully answering the following sub-questions will not only fulfill the research objectives but will also provide quantifiable metrics that are crucial for advancing the technical readiness level of MEMS Micro-resistojet thrusters. These metrics will yield a definitive understanding of performance and fidelity, thus solving the central research question in a measurable way.

1.4 Thesis Outline

This chapter offers a concise overview of micro-thruster applications in the aerospace industry. It delves into their background, associated challenges, and identifies a research gap. Additionally, this chapter outlines the research objectives of this thesis.

Chapter 2 provides the necessary literature preliminaries to comprehend the design and fabrication processes detailed in this thesis.

Chapter 3 adopts a paper-like format with publication in mind, focusing on the design aspects of the VLM thruster. Some redundancies may exist in the introduction section to ensure it functions as an independent entity.

Similarly, Chapter 4, which covers the fabrication and characterization of VLM thrusters, also follows a paper-like format. It strives to be fully comprehensible as an independent entity, which may result in some redundancies in the introduction and explanations of the design to be fabricated.

Chapter 5 elucidates the design and fabrication process for LPM thrusters, with less in-depth coverage due to the similarity in the fabrication process. The literature for these types of thrusters is introduced in the chapter itself, so it too may be read independently of the previous chapters.

The thesis concludes in Chapter 6, providing a comprehensive synthesis of the research - elaborating upon the scientific contributions made in this thesis and addressing the research question. Possible improvements and future work are also discussed.

Those who wish to read this report as a continuous entity can skip the following sections:

- 3.1.1 Working Principle: Vaporizing Liquid Micro-thruster
- 4.1.1 VLM Microthrusters
- 4.2.1 Design for Fabrication

2 | Literature Preliminaries

“We are like dwarfs sitting on the shoulders of giants. We see more, and things that are more distant, than they did, not because our sight is superior or because we are taller than they, but because they raise us up, and by their great stature add to ours.”

– John of Salisbury, *12th century*

2.1 Propulsion: Terminology and Mathematics

Propulsion refers to the act of "pushing forward" or "driving an object forward." A propulsion system is a machine designed to produce thrust, propelling an object in a particular direction. The generation of thrust often relies on Newton's third law, which states that for every action, there is an equal and opposite reaction.[1]

In simpler terms, propulsion involves generating a reaction force to move an object. The vehicle moves forward by changing its momentum in the opposite direction to the ejected propellant. In specific cases like aircraft and boats, the engines generate propulsion by exerting force against air and water, respectively.

According to ideal rocket theory, the **thrust equation** encapsulates two critical factors: the momentum change imparted by the engine to the working fluid and the pressure differential between the exhaust and incoming air, which is multiplied by the area of the nozzle. Mathematically, the thrust F_T is given by:

$$F_T = \dot{m}_e v_e - \dot{m}_0 v_0 + (p_e - p_0) A_e \quad (2.1)$$

where \dot{m} symbolizes the mass flow rate (dm/dt), v stands for velocity, p stands for pressure, and A is the nozzle area. The subscript "e" denotes variables at the exit, and the subscript "0" refers to variables at the entry or initial state. Refer to [Figure 2.1](#) for a graphical representation of these variables.



Figure 2.1: Schematic of variables in Propulsion

In order to write the thrust equation in a more compact way, an equivalent jet velocity is usually defined, indicated by v_{eq} in the equation, which accounts for both the momentum and pressure terms in the equation. Further, the input mass-flow and outlet mass-flow are equal. Hence, the updated equation becomes:

$$F_T = \dot{m} v_{eq} \quad (2.2)$$

Specific impulse is the change in momentum per unit mass for a rocket fuel. It is expressed in units of seconds and indicates the effectiveness of a propulsion system in converting the energy stored in propellant into useful kinetic energy. Mathematically, for steady state (v_{eq} is taken as average(v_{eq}) = V_{eq} = constant) Total and Specific Impulse I_{sp} can be represented as follows:

$$\text{Total Impulse} = I_t = F_T \Delta t = \int F_T dt = \int \dot{m} v_{eq} dt = m V_{eq} \quad (2.3)$$

$$\text{Specific Impulse} = I_{sp} = \frac{\text{Total Impulse}}{\text{Weight}} = \frac{I_t}{mg_0} = \frac{V_{eq}}{g_0} = \frac{F_T}{\dot{m}g_0} \quad (2.4)$$

The specific impulse of a propellant, when used with a particular rocket engine, describes how long the engine can accelerate its own initial mass at 1 g. Consequently, the higher the specific impulse, the greater the change in velocity Δv imparted to the system.

In simpler terms, specific impulse can be thought of as the amount of thrust generated per unit mass of fuel consumed. A higher specific impulse means the rocket can achieve the same thrust while using less fuel, making it a vital parameter for the design and evaluation of rocket propulsion systems. Since in rocket systems the only reaction mass is the propellant itself, hence specific impulse is defined as the thrust integrated over time per unit weight-on-Earth of the propellant[2].

2.2 Micro-Spacecraft

Miniaturized satellite platforms serve as a cost-effective and agile alternative to traditional large-scale systems, particularly reducing launch and fabrication expenses. The small size significantly cuts down material and labor costs during construction, allowing for rapid development cycles and quick deployment. This makes them particularly useful for testing experimental technologies and undertaking missions with higher risk profiles.

The adaptability and modular design of these small platforms make it easier to integrate a variety of instruments and payloads. This feature encourages multi-disciplinary research and fosters international collaborations by simplifying the integration process.

In terms of operations, deploying these satellites in a distributed network, commonly referred to as a satellite swarm or constellation, offers several unique advantages. These constellations excel in applications like fine-grained scientific data collection, real-time Earth observation, and robust communication relays. The distributed architecture provides built-in redundancy, which significantly improves the system's overall robustness and reliability.

The capability for multi-point data capture provides a more comprehensive view of phenomena that vary either spatially or temporally. Additionally, advancements in power management and solar technology contribute to making these miniature satellites more energy-efficient, further reducing long-term operational costs.

In summary, the lower financial barriers and shorter development cycles associated with these small satellite platforms are democratizing space exploration. They enable not just established space-faring nations but also smaller countries and private entities to contribute significantly to the fields of space exploration and commercialization.

2.3 Micro-Resistojet thrusters

A resistojet is a method of spacecraft propulsion that provides thrust by heating a propellant by sending electricity through a resistor, with the expanded gas expelled through a conventional nozzle.[3]

The working principle is based on resistance heating a propellant which is accelerated and expelled into space. The propellants are usually stored in a liquid or solid phase, then a phase change accompanies the heating process. The phase change is controlled by the conditions of pressure and temperature so as to allow sublimation or vaporization to take place. Based on the inlet pressure at which the device works two main types of micro-resistojets are identified: Vaporizing Liquid Microthruster (VLM) and Low-Pressure Microresistojet (LPM). The governing flow regime also differentiates the two. The VLM accelerates the gas in a convergent-divergent nozzle(adiabatic expansion). The flow is considered continuous and can be modeled as such. (Ivanov et al., 1999 [4]) theorize that a statistical method such as DSMC (Direct Simulation Monte-Carlo) is more accurate than the Navier-Stokes equations for the nozzle design. The LPM works at very low inlet pressure(<300 Pa) and a high Knudsen number. The flow must be modeled in the transitional flow regime.

2.3.1 VLM - Vaporizing Liquid Microthruster

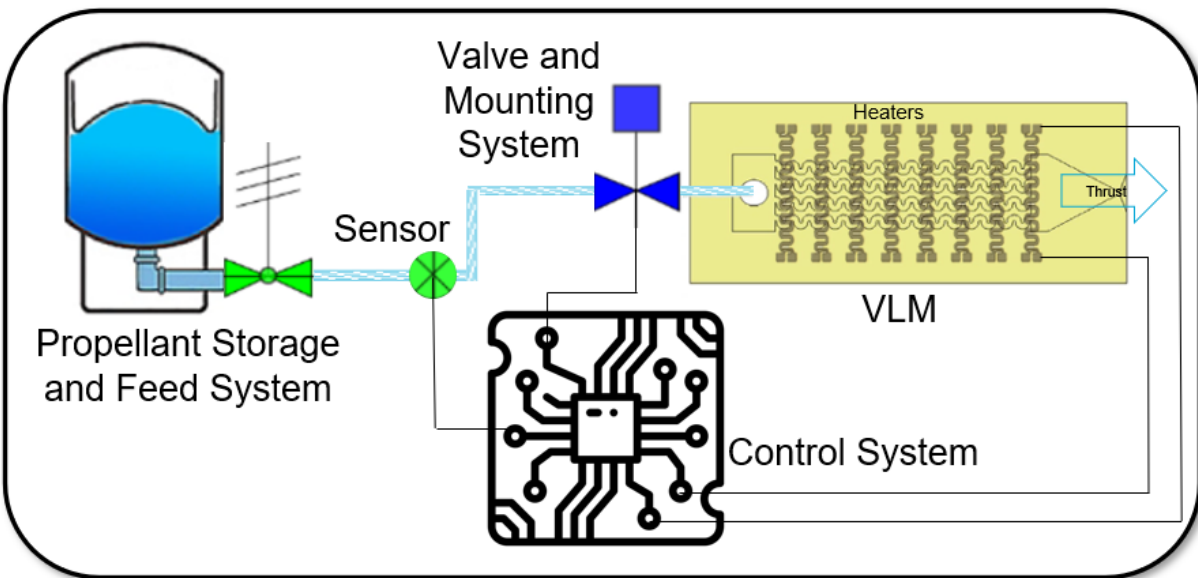


Figure 2.2: Schematic of a simple VLM system with feed and thruster components

VLMs are the most common microresistojet concepts. It is generally manufactured using MEMS processes in silicon or ceramic wafers. The propellant is fed through an inlet into an accelerating chamber with a heater, it undergoes a phase change and accelerates into a convergent-divergent nozzle where it achieves supersonic velocities.

The first VLM devices were theorized in the 1990s, the history of its development is detailed in Appendix [section A.4](#). The relevant state-of-the-art started when Silva et al. [5] from TU Delft developed a water-propelled VLM with integrated molybdenum heaters and temperature sensing in 2018. This work forms one of the bases for this thesis. Pallichadath et al.[6] designed and assembled the aforementioned VLM such that it can be accommodated in the pico-satellite platform Delfi-PQ, based on the PocketQube standard. They described the requirements and design of the complete micro-propulsion demonstrator and validated the performance characteristics of the thruster achieving a TRL of 4.

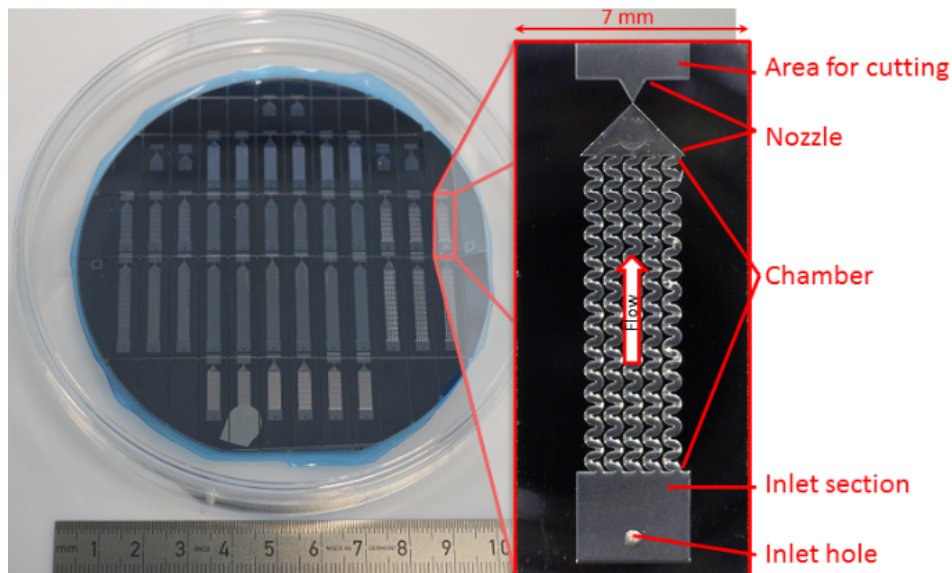


Figure 2.3: Parallel multi-shaped channel VLM, 2018 [5]

Karthikeyan et al.[7] designed and manufactured a VLM using low-temperature co-fired ceramic (LTCC) as the material due to the good electrical conductivity of printed metallization and a relatively low production cost. Cheah and Low[8] successfully tested a high-temperature co-fired ceramic (HTCC) microthruster characterized by a platinum-based microheater integrated on a three layers structure.

Liu et al.[9] developed a tubular concept of a VLM equipped with a micro-heater core, an excitation coil, a vaporizing chamber, and the micro-nozzle, all integrated into a glass tube obtaining a thrust of $680 \mu\text{N}$ at 5 mg/s . Kwan et al.[10] designed a water-fed VLM operating in the Leidenfrost boiling regime. The device was equipped with miniature molybdenum heating elements located inside the vaporization chamber producing a thrust of 2 mN with a specific impulse of 51 s .

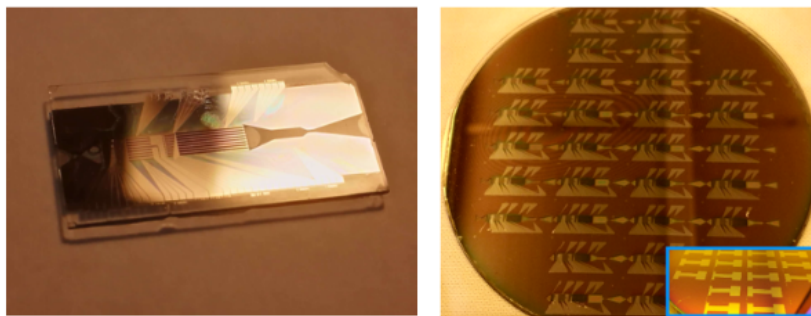


Figure 2.4: Sensor integrated VLM, 2021 [11]

Fontanarosa et al.[11] at the University of Salento designed and fabricated a silicon-based water-propellant VLM equipped with embedded microsensors for real-time monitoring of the in-channel vapor/liquid fraction and fluid temperature during its operation. Further, a secondary low-power platinum thin-film resistive heater was placed inside each of the eight channels, allowing for localized precision fluid heating and flow control. A preliminary charac-

terization of the embedded sensors demonstrated the operational feasibility of the fabricated microthruster, enabling a fine heating effect localization and vaporization control.

Most of the devices are tested with water due to its accessibility, safety and the fact that it can be stored as a liquid in CubeSats and PocketQubes conditions.(Guerrieri et al., 2017[12]). Water also has the best Δv per volume. The downside of water as a propellant is its high power consumption because of its high heat of vaporization. Current devices are able to deliver thrust in the range from around 1 mN to around 7 mN while consuming from 1 W to 10 W which might be high depending on the type of mission in consideration.

2.4 MEMS (Micro-Electro-Mechanical Systems)

Micro-Electro-Mechanical Systems(MEMS) are a unique combination of microelectronics and micro-mechanics. The fabrication of MEMS devices involves a series of processes that allow the integration of mechanical elements, sensors, actuators, and electronics on a common silicon substrate. This integration is achieved through the application of microfabrication technology, primarily adapted from integrated circuit (IC) technology.

MEMS fabrication is founded on the principles of photolithography, a precision patterning technique where a photosensitive polymer (photoresist) is exposed to UV light through a photomask, defining geometric patterns. Subsequent development, etching, or deposition processes utilize this patterned substrate to build intricate micro and nano-scale structures.

Brief Overview of the MEMS Fabrication Processes[13]:

1. Bulk Micromachining: This involves the selective removal of parts of the silicon wafer, using either wet or dry etching methods. The most well-known process in this category is the anisotropic wet etching of silicon, where certain crystallographic planes of silicon etch slower in specific chemical solutions, enabling precise geometries.
2. Surface Micromachining: This method builds microstructures by depositing and etching thin films on the substrate. The technique typically employs a sacrificial layer (often made of silicon dioxide or polysilicon), which is subsequently etched away to free the movable parts of the MEMS device.
3. High Aspect Ratio (HAR) Micromachining: Techniques such as deep reactive-ion etching (DRIE) fall under this category, allowing for the creation of deep, narrow structures on the silicon substrate. DRIE uses alternating cycles of etching and passivation to achieve these high aspect ratios.
4. Wafer Bonding: This process involves bonding two wafers or a wafer and another substrate (like glass) to create multi-layer structures. There are various techniques, such as anodic bonding and fusion bonding, each suitable for specific applications.
5. Package and Integration: Once the MEMS device is fabricated, it needs to be encapsulated to protect it from external environmental factors.

The MEMS fabrication process is intricate and varies based on the desired device's design and application. Successful fabrication requires rigorous process control to ensure repeatability, reliability, and optimal device performance.

2.5 Summary and Research Gap

Propulsion systems are fundamentally based on generating thrust, with their basic definition rooted in Newton's third law. The thrust equation and its elements elucidate this, particularly highlighting the role of a rocket fuel's specific impulse. Shifting the focus to micro-spacecraft, the literature brings out the usefulness of miniaturized satellite platforms. The emphasis largely falls on the economic benefits they bring—primarily cost savings—and their expedited development cycles. Satellite constellations or swarms, a concept intrinsic to these platforms, are gaining traction. Complementing these advancements is the progress in power management, which ensures enhanced energy efficiency.

Micro-resistojet thrusters, a subset of propulsion systems, operate based on electric heating of propellant. They can be categorized primarily into Vaporizing Liquid Microthrusters (VLMs) and Low-Pressure Microresistojets (LPMs). The distinction between the two is evident in the pressure at which they function and subsequently their phase-change mechanisms and the governing flow regimes. Diving deeper into VLMs, they are known for a distinct manufacturing process and operation principle. Historical insights reveal the trajectory of VLM development, with notable contributions like the 2018 study from TU Delft that spotlighted a water-propelled VLM. Further mentions include the design efforts to integrate the design in the Delfi-PQ pico-satellite platform.

With the increasing demands of space missions, the drive for enhancing efficiency, reducing size, and ensuring reliability has become paramount, where MEMS Micro-resistojet shows significant promise. Yet, several aspects need addressing. First, there is no consistent mapping between the thruster shape and its performance, largely influenced by flow dynamics in rectangular nozzles. Optimizing flow can potentially lead to breakthroughs in thruster efficiency while maintaining a compact size. Next, while there have been strides in design innovation, there is a clear need to advance fabrication techniques that are both time-effective and maintain design fidelity. Current fabrication methods often lead to deviations from the initial design, affecting the overall efficiency and reliability of the thruster. Addressing these gaps is crucial for the next wave of space exploration missions and for elevating the technical readiness level of MEMS Micro-resistojet thrusters. It is on the basis of these areas of improvement that the research question ([section 1.3](#)) was based.

3 | Design of MEMS Vaporizing Liquid Micro-resistojet Thrusters

“Any intelligent fool can make things bigger and more complex... It takes a touch of genius - and a lot of courage to move in the opposite direction”

– E.F. Schumacher, 1973

Re-designing rectangular cross-section MEMS Vaporizing Liquid Micro-resistojet Thrusters for Numerically Optimized Flow Performance

S.I. Singh*, A. Cervone[†], M.Ghatkesar*, H. van Zeijl[‡]

*Precision Mechanism Engineering, Mechanical Engineering Faculty, Mekelweg 2, 2628CD Delft, TU Delft, The Netherlands

[†]Space Engineering Department, Aerospace Engineering Faculty, TU Delft, Kluyverweg 1, 2629HS Delft, The Netherlands

[‡]Else Kooi Laboratory, EEMCS Faculty, TU Delft, Feldmanweg 17, 2628CT Delft, The Netherlands

Abstract—This paper conducts an in-depth study aimed at flow optimization in Vaporizing Liquid Micro-resistojet (VLM) thrusters, utilizing Computational Fluid Dynamics (CFD) across an expansive design space tailored for MEMS rectangular nozzles. The investigation results in a modified VLM thruster design that incorporates an inlet with a 40% enhancement in the flow uniformity across the inlet. The new design includes optimized nozzle dimensions to maximize thrust for a given mass flow rate without changing the original size of the thruster. An 18% increase in thrust and specific impulse, both key performance metrics, over previous iteration validates the efficacy of numerical optimization techniques in improving MEMS-based thruster capabilities.

Index Terms—microthruster, CFD, VLM, nozzle, inlet, flow-optimization

I. INTRODUCTION

Vaporizing Liquid Microresistojet (VLM) microthrusters have increasingly become the focus of attention in the field of small-scale satellite propulsion, attributed to their compact form factor, precise control capabilities, and high-performance metrics. One of the pivotal aspects in leveraging these advantages lies in the selection and optimization of the inlet and nozzle designs, which are critical for the overall propulsion efficiency and mission success. Minimizing propellant mass (with respect to total impulse produced) can markedly lower the launch mass of a satellite or spacecraft. This results in cost reductions due to the employment of smaller launch vehicles needed to transport a specified mass to a designated orbit [1].

In this context, the paper first addresses inlet design modifications to achieve a more streamlined and well distributed flow with minimal transitional phase and high consistency. Subsequently, the study engages in a comprehensive investigation aimed at determining optimal dimensions for two distinct types of nozzle configurations: the aerospike and the convergent-divergent (CD) nozzles. Notably, the study is necessitated by the rectangular cross-sections of the nozzles, a characteristic dictated by the MEMS manufacturing process, which renders traditional cylindrical nozzle calculations inapplicable [2].

The aerospike nozzle, characterized by its spike-like form, circumvents the need for an external divergent section, utilizing boundary layer expansion for efficient propellant expulsion [3]. In contrast, the CD nozzle, a time-tested design prevalent in micro-propulsion systems, employs a convergent section for

accelerating the propellant to Mach 1, followed by a divergent section that expands flow, optimizing thrust generation [4].

Computational Fluid Dynamics (CFD) simulations, executed on the COMSOL platform, are employed to assess the performance and efficiency of these thruster designs under realistic operating conditions, taking into account specific propellant properties and geometric constraints. The insights derived from this study are intended for practical application in the fabrication of VLM thrusters at Else Kooi Labs (EKL), Delft, serving as a foundational framework for future development in this domain.

A. Working Principle: Vaporizing Liquid Micro-thruster

A VLM thruster is a specialized propulsion system designed for micro- and nanosatellite applications. Operating on the principle of resistojet propulsion, electrical energy is applied to heat a fluid propellant. The resistive heating process results in rapid vaporization of the liquid propellant, which is then expulsively ejected through a nozzle to produce thrust [5]. The fundamental design of a VLM thruster includes the following sub-components:

External Modules:

Propellant Storage: A tank designed to store the liquid propellant under pressure, with material selection influenced by the specific propellant in use and its storage requirements.

Propellant Feed System:

- (a) Piping: A setup to transport the fluid from the reservoir to the thruster through a series of flow controllers and valves.
- (b) Valves: Solenoid or piezoelectric valves regulate the flow of the propellant, actuated by commands from the control system.

Electrical Control Systems:

- (a) Power Supply: Provides the electrical energy required for resistive heating.
- (b) Control Systems: A microcontroller that orchestrates operational sequencing such as valve actuation and heating element modulation, allowing for real-time thrust adjustments.
- (c) Sensors: Incorporates temperature, pressure, and flow sensors for real-time feedback and control.

Internal Components:

Inlet: Microfluidic interconnect where the propellant enters the thruster.

Vaporization Chamber: Specifically designed to maximize the surface area for effective heat transfer, a crucial parameter affecting both power consumption and thermal performance.

Micro-Resistive Heaters: These heaters are designed to achieve the requisite vaporization temperatures without compromising structural integrity.

Nozzle Exit: Engineered to accelerate the propellant, optimizing thrust generation.

B. Design Calculations for Vaporizing Liquid Micro-thruster

To establish a numerical model for the VLM thruster, we need to derive essential mathematical relationships. Definitions for terms and variables used are provided for clarity.

1) Definitions and Assumptions:

- n/V : Number of moles per unit volume [mol/m³]
- p : Pressure [Pa]
- T : Temperature [K]
- R_A : Gas constant [J/(K·kmol)]
- M_W : Molecular mass [kg/kmol]
- γ : Ratio of specific heats of the propellant
- ρ : Density [kg/m³]
- a : Velocity of Sound [m/s]
- M : Mach number
- A : Cross-section area nozzle throat(A_t) or exit(A_e)

The propellant employed in this study is water, with a molecular weight of 18 g/mol. Water is selected due to its availability and favorable thermodynamic properties. The ratio of specific heats (γ) for water is identified as 1.33 for the selected temperature range [6]. In line with ideal rocket theory, the velocity at the throat — the juncture where the nozzle cross-section is at its minimum — is postulated to be Mach 1, signifying sonic conditions [7]. The chosen design target temperature is set at 700 K. This temperature is derived based on a combination of thermodynamic efficiency, material constraints, and desired performance outcomes. Accompanying this, an input pressure of 6 bar has been established. This pressure value is determined by balancing the need for increased thrust and the operational limits of the system components.

2) Ideal Gas Equations [4]:

$$\begin{aligned} \frac{p}{V} &= \frac{p}{R_A \cdot T}, \\ p &= \rho \frac{R_A}{M_W} \cdot T, \\ c_p &= \frac{\gamma}{\gamma - 1} \cdot \frac{R_A}{M_W}, \\ a^2 &= \gamma \cdot \frac{p}{\rho} \end{aligned} \quad (1)$$

3) Vandekerckhove function [8]:

$$\Gamma(\gamma) = \sqrt{\gamma \cdot \left(\frac{1 + \gamma}{2} \right)^{\frac{1 + \gamma}{1 - \gamma}}} \quad (2)$$

4) Mass Flow Rate (choked nozzle) [9]:

$$\dot{m} = \frac{p \cdot A_t}{\sqrt{\frac{R_A}{M_W} \cdot T}} \cdot \Gamma(\gamma), \quad (3)$$

Here, choked flow implies a compressible flow effect that the flow at the throat of the nozzle reaches sonic condition. By inserting the values for R_A , M_W , T , and p_c , we find for throat width of 50 μm ($A_t = 7.5 \times 10^{-9} \text{ m}^2$, since the height of the rectangular throat in this study is fixed at 150 μm):

$$\dot{m} \approx 2.6 \times 10^{-6} \text{ kg/s for } w_t = 50 \mu\text{m} \quad (4)$$

5) *Power Requirement for Heating:* The power required for heating the liquid propellant to its vaporized state is given by:

$$P_h = \frac{p \cdot A_t \cdot \Gamma(\gamma)}{\sqrt{\frac{R_A}{M_W} \cdot T}} [c_{pL} \cdot (T_{\text{boil}} - T_0) + L_h + c_{pG} \cdot (T_C - T_{\text{boil}})] \quad (5)$$

Substituting the values yields $P_h \approx 2.798 \text{ W}$. This quantifies the power requisite to elevate the propellant's temperature to 700K. Notably, this represents an idealized scenario. To validate its feasibility, an experimental determination of the necessary power—prior to accounting for losses—is essential. Subsequently, this value should be assessed against the system's design parameters as outlined by Silva et al. [10].

6) *Thrust, Specific Impulse and Efficiency:* Having discussed the idealized equations pertinent to the previous calculations, it is imperative to transition to a more comprehensive definition of thrust. Unlike the aforementioned idealizations, this definition encapsulates the full complexities inherent in thrust generation without any simplifying assumptions. For a CD nozzle, the thrust (F) is derived from a surface integration of the momentum flux of the propellant. Specifically, this integration spans across a defined output area, which in this analysis corresponds to the exit of the nozzle. Mathematically, this can be represented as:

$$\begin{aligned} \mathbf{F} &= - \iint_{A_e} \mathbf{V}(\rho \mathbf{V} \cdot \mathbf{n}) dA_e - \iint_{A_e} ((p - p_\infty) \mathbf{n}) dA_e \\ &+ \iint_{A_e} (\boldsymbol{\tau} \cdot \mathbf{n}) dA_e \end{aligned} \quad (6)$$

The third term (due to viscous stress state) does not contribute to the value much for this scenario and hence can be ignored. In space $p \approx p_\infty$, hence the second term will contribute only a small percentage of the total thrust but is included for higher accuracy. The sign is for direction and is inconsequential to the magnitude. Hence it is possible to understand the thrust performance of a nozzle by simply finding the value of the following surface integral across the nozzle exit cross-section:

$$F = \iint_{A_e} (\mathbf{V}(\rho \mathbf{V} \cdot \mathbf{n}) + (p - p_\infty) \mathbf{n}) dA_e \quad (7)$$

The Specific Impulse I_{sp} is then given by:

$$I_{sp} = \frac{F}{\dot{m} \times g_0} \quad (8)$$

The ideal rocket theory definition of nozzle exit velocity is:

$$V_{e-ideal}^2 = \frac{\gamma \cdot R_{gas} \cdot T_c}{\gamma - 1} \cdot \left[1 - \left(\frac{p_e}{p_c} \right)^{\frac{\gamma-1}{\gamma}} \right] \quad (9)$$

This would give the Ideal specific impulse as:

$$I_{sp-Ideal} = V_{e-ideal}/g_0 \quad (10)$$

Using these, the nozzle efficiency η_n can be calculated as:

$$\eta_n = \frac{I_{sp}}{I_{sp-Ideal}} \quad (11)$$

II. INLET DESIGN FOR EFFICIENT FLOW

The transition from macroscopic environmental conditions to microscopic components constitutes a significant engineering challenge in the realm of microfluidic devices. This interface is commonly referred to as the macro-to-micro interface, interconnect, or the world-to-chip interface.

In earlier iterations of MEMS micro-thrusters, rudimentary inlets were often designed as simple wells at the termini of fluidic channels [11]. An advancement over this design employs integrated interconnects capable of accommodating applied pressure or vacuum to facilitate fluid flow, enhancing the functionality of the device. Consequently, several multi-functional devices can be linked for more complex fluidic analyses.

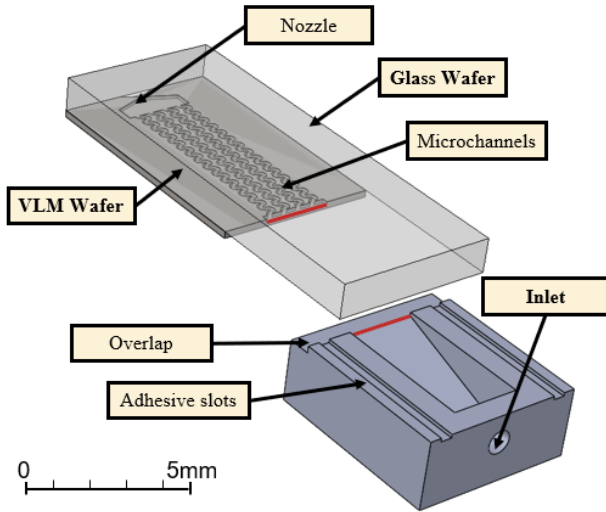


Fig. 1: CAD model of proposed microfluidic interface - the edges highlighted would mate on assembly

In the quest to enhance fluidic device interconnectivity, several design options were considered. Upon analyzing this advantage, a subsequent design iteration was conceptualized that integrated the inlet flow geometry with the microchannel geometry. This adaptation not only facilitates smoother fluid

flow but also improve the compactness of the overall thruster. The design was iteratively improved through testing, specifically in terms of flow rate consistency and resilience against fluidic back-pressure. This assessment also took into account factors such as ease of integration, overall size, and the potential for modularity. The results of a comparative study between the final and initial designs (explained in subsection V-A) unequivocally indicated that the new, integrated interconnect, design was superior in multiple facets.

While the original interface served its purpose within its limitations, the newly proposed design, showcased in Figure 1, emerges as a significant improvement. It offers enhanced functionality, adaptability, and efficiency, making it a promising choice for future fluidic applications.

The next iteration of this design employs modular interfaces that are, to a large extent, independent of the material composition of the device. This modularity permits the incorporation of multiple, or even diverse types of, thrusters onto a single framework equipped with multi-faceted inlets and valves.

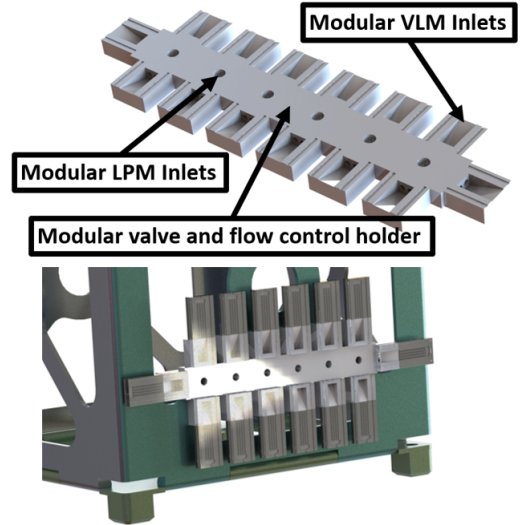


Fig. 2: A possible configuration of the proposed modular microfluidic interface for both VLM and LPM thrusters and its integration to a cube-satellite

The modular design offers a range of benefits. With its interfaces, satellites can have an array of thrusters tailored for varied tasks, from orbital adjustments and station-keeping to intricate deep-space maneuvers. Depending on a satellite's primary function, thrusters can be tactically positioned; for example, an Earth-observing satellite could have a configuration emphasizing its orientation and altitude adjustment for prime imaging. Instead of crafting a distinct propulsion system for each satellite, there's potential to create a universal modular framework, into which different thrusters can be incorporated, markedly cutting design and fabrication expenses. This compact, integrated design also means satellites can host more instruments or payloads without major propulsion system overhauls. Furthermore, as satellite technology advances, new thruster models or tech can be smoothly added to the existing

frameworks, ensuring propulsion is always at the forefront of innovation.

Illustrating this concept, a modular thruster assembly that synergistically combines Vaporizing Liquid Micro-resistojet (VLM) with Low-Pressure Micro-resistojet (LPM) thrusters is presented in Figure 2. This assembly showcases the potential for harmonizing different propulsion mechanisms in a singular, efficient structure suitable for diverse satellite applications.

From the perspective of individual thruster performance, the efficacy of these design updates is assessed based on their ability to optimize inlet fluid dynamics. Computational Fluid Dynamics (CFD) simulations are utilized to evaluate the enhancements in flow characteristics, focusing on parameters such as laminarity, flow-rate distribution across the thruster inlet, and the time to achieve flow steadiness.

Both the conventional (well-based) and new (integrated interconnect) designs were subjected to simulation using water as the propellant fluid. It is assumed that within this specific region of the thruster, no phase transition occurs. The selected parameters for the simulations are tabulated in Table I.

TABLE I: CFD Simulation Parameters for Evaluating Microchannel Inlet Flow

Parameter Type	Parameter Name	Selected Value
Geometrical	Channel exit Width	3 mm
Geometrical	Channel Thickness	150 μm
Fluid Property	Fluid Type	Water
Fluid Property	Density	997 kg/m^3
Fluid Property	Dynamic Viscosity	0.001 Pa.s
Initial Condition	Inlet Pressure	6 bar
Boundary Condition	Outlet Pressure	1 bar
Boundary Condition	Wall Type	Slip
Numerical	Time Step	0.01 s
Numerical	Grid Density	Variable
Numerical	Convergence Criteria	Residual $< 10^{-3}$

III. ACCELERATION CHAMBER AND HEATER DESIGN SELECTION

Critical to the thruster’s functionality is the heating chamber, where propellant undergoes vaporization and thermal elevation giving rise to complex two-phase flow dynamics [12]. Given that the chamber is fabricated from MEMS components, the design scope is remarkably flexible, constrained primarily by the precision limitations inherent to the chosen manufacturing technique. To select the optimal chamber geometry, the analytical insights and findings of Cervone et al. [13] were consulted.

Several chamber configurations were evaluated by the referenced study, including:

- An open rectangular cross-section devoid of internal structures.
- Channels or fins aligned with the direction of fluid flow.
- Sinusoidal or serpentine channels.
- Discrete, free-standing pillars or fins.

The selection criteria for these configurations were multifaceted, encompassing considerations such as ease of fabrication, anticipated pressure drop, thermal efficiency, and the

homogeneity of the resultant flow field. Upon review, semi-circular serpentine micro-channels were chosen for further investigation due to their superior thermal performance and consistent flow dynamics. The continuous curvature of semi-circular serpentine channels promotes uniform heat distribution, ensuring that the propellant undergoes consistent and efficient vaporization across the entire channel, minimizing cold spots and ensuring optimal thruster performance. Additionally, the design promotes a consistent flow pattern, ensuring that the vaporized propellant exits the chamber with a homogeneous flow profile, which is crucial for the stability of the thrust generated by the microthruster.

The final selected vaporization and heating chamber design for the microthruster was adapted from the design proposed by Silva et al. [14] This selection was motivated by the design’s superior performance metrics in both energy efficiency and manufacturing fidelity, as benchmarked against other prevalent designs in the literature. A comprehensive description and schematic of the adopted design are provided in Figure 3.

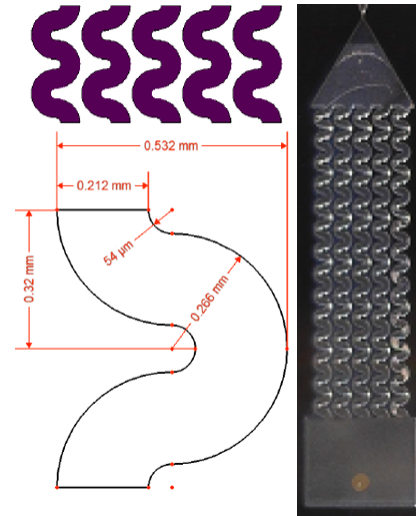


Fig. 3: Clockwise from top left: serpentine chamber modular mask; previously fabricated thruster with channel design; dimensions of a single serpentine section [14]

In MEMS devices with integrated heaters, common designs employ electrically conductive thin films, which may consist of polycrystalline semiconductor layers, thin metal films, or diffused layers in silicon. Power generation can be realized either through ohmic or inductive methods. Inductive heating has proven effective in VLM applications [15] and presents an attractive option for internal heating within micro-chambers as it eliminates the need for external wire connections, thereby reducing the risk of compromising channel sealing.

However, if the heating chamber is to be isolated from the channels, ohmic heating serves as a more direct mode of power delivery, converting 100% of the electrical energy into thermal energy. It offers the added advantage of facilitating temperature monitoring through resistance variation tracking and boasts a faster response time compared to inductive

methods.

High-temperature applications commonly utilize Titanium, Molybdenum, Platinum, or Tungsten as heater materials. Their maximum operating temperatures, outlined in Table II, depend on material linearity and oxygen exposure susceptibility, although oxygen exposure is typically irrelevant in space applications.

Mechanical stability of micro-heaters on flexible membranes is optimized with materials exhibiting low Young's modulus and high tensile strain. Thermal stress mitigation strategies include selecting materials with low thermal expansion coefficients (TECs) and matching them with insulating layers like SiN or SiO₂, along with high thermal conductivity.

Efficient heat generation mandates that the resistive layer's electrical resistivity surpasses that of the contact pads to concentrate Joule heating. Stability and response times hinge on material linearity and temperature sensitivity, respectively.

Platinum is favored for its chemical inertness but requires an adhesion layer due to poor glass bonding. Molybdenum offers high melting points and TCR but is not CMOS-compatible and needs oxidation protection above 320°C. Titanium, operable up to 700°C, provides high accuracy and simpler processing, but its reactivity with glass necessitates an adhesion layer.

TABLE II: Maximum operating temperature of micro-heaters fabricated from different materials

Micro-heater Material	Maximum Operating Temperature (°C)
Molybdenum	700 [16]
Titanium	700 [17]
Platinum	550 [18]
Tungsten	600 [19]

Upon evaluating the aforementioned considerations - material linearity, oxygen exposure susceptibility, mechanical stability, efficient heat generation, chemical inertness, adhesion layer requirements, compatibility with CMOS processes and melting points - a Titanium heating element situated on a Silicon Oxide layer was chosen for the final device architecture. The heater's physical configuration adopts the serpentine channel design as proposed by Spervasilis et al. Finite Element Method (FEM) simulations were employed to optimize the channel's pitch and width, targeting maximum temperature uniformity [20]. The shape is shown in Figure 4.

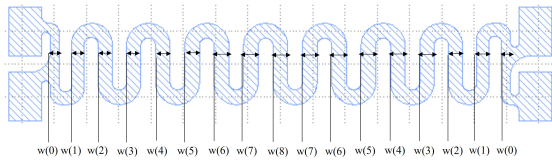


Fig. 4: Micro-Heater shape as developed by Spervasilis et al. [20]

IV. OPTIMIZED NOZZLE DESIGN SELECTION

A. Convergent Divergent Nozzle

Model: The shape of a CD nozzle is defined by parameters shown in Table III and visualized in Figure 5.

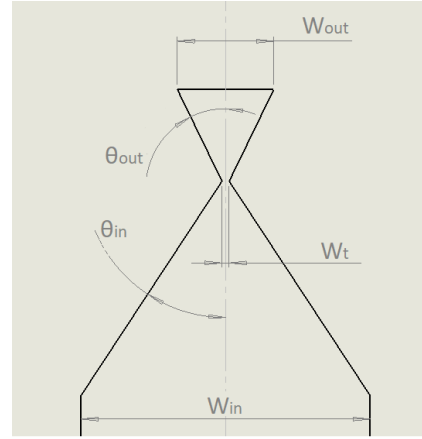


Fig. 5: Convergent Divergent Nozzle Parameters

TABLE III: CD Nozzle Design Variables

variable	symbol
Convergence half angle	θ_{in} or θ_c
Divergence half angle	θ_{out} or θ_d
Throat width	W_t
Inlet width	W_{in}
Area ratio	$\varepsilon = \frac{A_c}{A_t} = \frac{W_{out}}{W_t}$

Some assumptions made during the modeling process include:

- **Steady-state flow:** The simulation assumes that the flow through the nozzle is steady and does not vary with time. This assumption neglects any transient effects or unsteady behavior that may occur during startup or shutdown phases. However, this assumption is also validated as will be explained in subsection V-B.
- **Ideal gas behavior:** The propellant, vaporized water in this case, is assumed to behave as an ideal gas. This assumption implies that the gas molecules do not interact with each other and that the specific heat ratio (γ) remains constant.
- **Propellant properties:** The simulation assumes that the properties of the propellant, such as viscosity, specific heat, etc. remain constant throughout the nozzle. This assumption neglects any variations in properties due to temperature or pressure gradients.
- **Isentropic flow:** The flow through the CD nozzle is assumed to be isentropic, meaning there are no losses or dissipation of energy due to friction or heat transfer. This assumption simplifies the calculations but may not capture all the real-world losses.

Mesh: To accommodate the significant computational demands of running simulations across thousands of variable parameter combinations, an initial coarse mesh was chosen for the preliminary model. A mesh convergence study was conducted to assess the fidelity of the computational models. Both mesh size variations and the corresponding convergence results were recorded. Through this study, it was determined that the coarser mesh employed for the preliminary sweep study

exhibited a minor deviation, with thrust values fluctuating by approximately $\pm 3\%$. This coarser mesh was strategically utilized to approximate the optimal design parameters. Once in the proximity of the desired design, the most suitable mesh size—defined as the size where further refinements have negligible impact on results yet increase computational time—was employed to derive the final values.

For the initial coarse mesh, the parameters selected were a tetrahedral mesh with a maximum element size of 5.66×10^{-4} m, a minimum element size of 1.41×10^{-4} m, a curvature factor of 0.9, a resolution in narrow regions set to 0.4, and a maximum element growth rate of 1.3.

Given that the CFD simulations focus on a microthruster with a throat size in the order of magnitude of 25-100 μm , the mesh sizes were selected to sufficiently capture the geometric details and fluid behavior while balancing computational efficiency. The curvature factor and resolution in narrow regions were specifically chosen to offer higher fidelity in capturing the microthruster’s intricate geometric features, and to properly simulate the high-pressure differential between the 6-bar inlet and vacuum outlet. The mesh for one of the thruster models is shown in Figure 6.

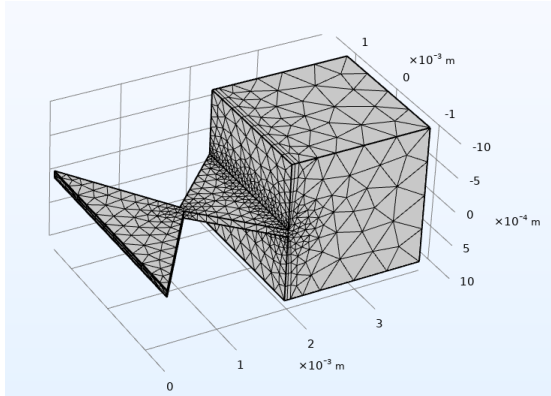


Fig. 6: mesh generated for a CD Nozzle

Parametric Sweep: In constructing the simulation model for this study, a parametric sweep was employed to systematically explore the optimal design characteristics of the convergent-divergent (CD) nozzle. The expansion ratio, converging angle, and diverging angle were chosen as key parameters for investigation. These variables were varied across all realistic geometric possibilities; specific starting values, increments, and final values for each parameter are detailed in Table IV.

TABLE IV: CD Nozzle Parametric Sweep

Parameter	Start Value	Last value	Increment
Throat Diameter (μm)	25	100	25
Convergent angle ($^\circ$)	10	80	2.5
Divergent Angle ($^\circ$)	10	80	2.5
Area Ratio	5	20	1

Other nozzle parameters were held constant for the duration of the simulations. These fixed variables were determined based on constraints dictated by the microthruster fabrication

process and heater calculations. A summary of these fixed values can be found in Table V.

In addition to these key parameters, the study considered the effects of four distinct throat diameters. Each throat diameter requires a different mass flow rate, thereby yielding different levels of thrust and, inversely, affecting propellant consumption. Therefore, these throat diameters were considered as distinct design scenarios rather than directly comparable options, and hence the selection of throat diameter is application-specific. Nonetheless, the study does identify the maximum efficiency that can be achieved for each throat diameter, which offers valuable insights for different design configurations.

Employing this comprehensive parametric sweep, the simulation model serves as a robust tool for identifying optimal nozzle designs within real-world constraints. This approach ensures the rigor and relevance of the study, making a significant contribution to the development of efficient microthrusters.

Convergence: Convergence is a critical component of Computational Fluid Dynamics (CFD) simulations, indicating that the simulated parameters—such as flow field, pressure distribution, and other relevant variables—have stabilized to a reliable state. For CFD simulations of this study achieving a stable and accurate solution is particularly important to ensure the validity of the findings. The convergence criterion was set at a solution tolerance of 1×10^{-3} . This specific choice for the error tolerance was motivated by two factors. First, this error magnitude was found to be sufficient for capturing the relevant physics of the microthruster model without significantly impacting the computational time, a critical consideration given the large number of simulations conducted. Second, preliminary tests showed that reducing the error threshold further resulted in negligible changes in the calculated thrust and flow characteristics, thus affirming the suitability of this tolerance level.

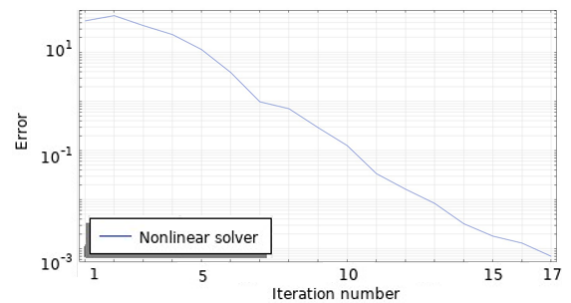


Fig. 7: CD Nozzle Simulation Convergence

An illustration of the simulation achieving convergence is presented in Figure 7, which displays a graph of error versus iteration number for a sample simulation from amongst the sweep. This graphical representation shows that each simulation iteration converged to an error less than 1×10^{-3} (convergence criterion). The trend holds consistently for all the simulation iterations carried out in this study, confirming the reliability and robustness of the simulation settings.

TABLE V: Parameters to build a model of CD Nozzle

Name	Expression	Value	Description
D_t	d [um]	d * E-3 m	Throat width (Part of Parameter Sweep)
A_ratio	ϵ	ϵ	Ratio A(exit) and A(throat);(Part of Parameter Sweep)
alpha	α [deg]	$\pi*\alpha/180$ rad	Diverging half angle (Part of Parameter Sweep)
beta	β [deg]	$\pi*\beta/180$ rad	Convergent half angle (Part of Parameter Sweep)
D_in	3 [mm]	0.003 m	Inlet width
D_out	A_ratio * D_t	0.002 m	Outlet Width
h_nozzle	150 [um]	1.5E-4 m	The total nozzle slit height
p_in	6 [bar]	6E5 Pa	Inlet pressure coming from the heating chamber
T_in	273.15 [K] + 500 [K]	773.15 K	Inlet temperature coming from the heater element
p_amb	0.00001[bar]	1 Pa	The ambient pressure and exit pressure
m_dot	3.5 [mg/s]	3.5E-6 kg/s	Mass flow rate (for crosschecking results)
L_in	$(1/2*D_{in} - 1/2*D_t)/\tan(\beta)$	0.0010153 m	Length of the converging part
L_out	$(1/2*D_{out} - 1/2*D_t)/\tan(\alpha)$	9.5E-4 m	Length of the diverging part
L_tot	L_in + L_out	0.0019653 m	Total length Nozzle
t_air	2000 [um]	0.002 m	Assumed outlet box dimensions (Space)

Post-processing: For each simulation run, corresponding to a unique parameter combination, the following results are calculated:

- 1) Velocity profile (Figure 14a)
- 2) Pressure distribution near the throat (Figure 14c)
- 3) Reynolds Number(Figure 14d)
- 4) Knudsen Number (Figure 14b)
- 5) Thrust - calculated as the surface integral of momentum flux across the nozzle exit (Equation 7)

Among these, the thrust and Knudsen number are prioritized for nozzle selection.

The velocity profile gives information about the flow acceleration through the nozzle's convergent section, serving as an indicator of the efficient conversion of pressure energy to kinetic energy. The pressure at the throat is a critical parameter for various calculations and performance metrics, which the graph helps validate. Any sudden or unexpected spikes in the pressure graph can indicate the occurrence of flow phenomena like shockwaves or flow separations, which could impact thruster performance. Reynolds Number can flag potential issues with flow regimes, low values may suggest non-continuous flow, though Knudsen Number is more reliable for this determination. High Reynolds Number values could indicate turbulence, although no turbulence was observed for nozzle shapes up to 100 μm in throat width. A visualization of these parameters for one of the parametric combinations is shown in Figure 14.

The Knudsen Number serves as a critical metric for design selection, as it is a dimensionless number that characterizes the flow regime by comparing the molecular mean free path of a fluid to a characteristic physical length scale. It is used to distinguish between continuum, transitional, and rarefied flows. A continuum flow is essential for the efficient functioning of the nozzle; therefore, any nozzle with a Knudsen Number (K_n) near the throat (see area of interest marked in Figure 14b) exceeding a threshold of 0.01 will be disqualified for further evaluation, as this value marks the transition to a non-continuum flow regime. A visualization of a qualified design (K_n in throat <0.01) is shown in Figure 14.

Lastly, to calculate the thrust for each iteration a cut plane

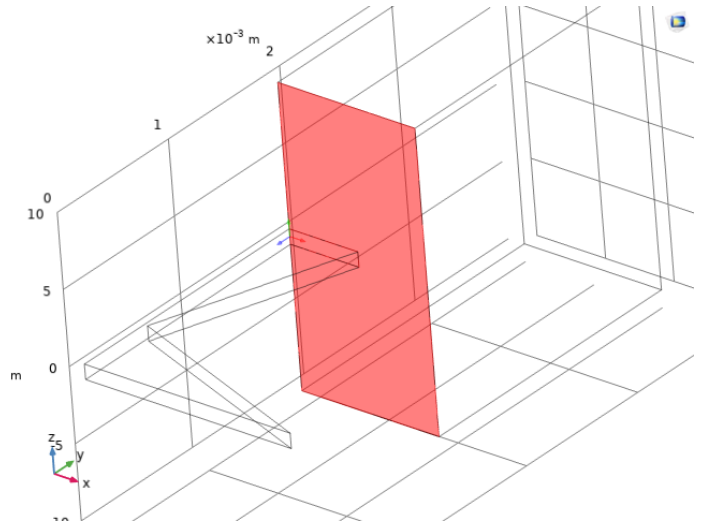


Fig. 8: Output plane used for thrust calculation

must be considered at the exit of the Nozzle. The surface integral in (Equation 7) is evaluated across this plane which is visualized in Figure 8.

B. Aerospike Nozzle

TABLE VI: Aerospike Nozzle Design Variables

variable	symbol
Outer Convergence angle	θ_1
Spike Divergence angle	θ_2
Spike Convergence angle	θ_3
Throat width	W_t
Inlet width	W_{in}
Spike inward length	L_1
Spike outward Length	W_{in}
Distance between outlets	W_{out}
Fillet Radiuses	$R_1, R_2 \text{ \& } R_3$
Truncation percentage	$1 - \frac{L_2'}{L_2}$

Model: A simplified aerospike nozzle design serves as the basis for simulating the performance impact of varying various dimensional parameters of the nozzle. These variable parameters are listed in Table VI and illustrated in Figure 9. The

TABLE VII: Aerospike Nozzle parameter variation

$W_t(\mu m)$	$W_{out}(mm)$	$L_1(mm)$	trunc	θ_1	θ_2	R_2	R_1	$\iint v dA$	
75	1.5	2.5	0.66	120	20	0.2	0.5	5.39E - 05	Reference
25	1.5	2.5	0.66	120	20	0.2	0.5	4.28E - 05	Major decrease
50	1.5	2.5	0.66	120	20	0.2	0.5	5.01E - 05	Slight decrease
100	1.5	2.5	0.66	120	20	0.2	0.5	6.48E - 05	Increase
75	1	2.5	0.66	120	20	0.2	0.5	5.21E - 05	Slight decrease
75	1	2.5	0.66	120	20	0.5	0.5	6.22E - 05	Increase
75	1.5	1.5	0.66	120	45	0.2	0.5	4.64E - 05	Decrease
75	1.5	2.5	0.33	120	20	0.2	0.5	3.54E - 05	Major decrease
75	1.5	2.5	0.66	100	20	0.2	0.5	7.28E - 05	Major increase
75	1.5	2.5	0.66	120	20	0.2	0.2	5.39E - 05	No effect

complexity in modeling this nozzle arises from its multitude of variables, including many radii, angles and lengths. Moreover, within the given dimensional constraints, the feasible design space for these variables exhibits inter-dependencies. For instance, an increase in the inlet spike angle (θ_2) constrains the allowable inlet spike length (L_1), due to the spatial limitation of the overall width of the channel. Numerous such inter-dependencies exist, making it infeasible to model the entire design space exhaustively.

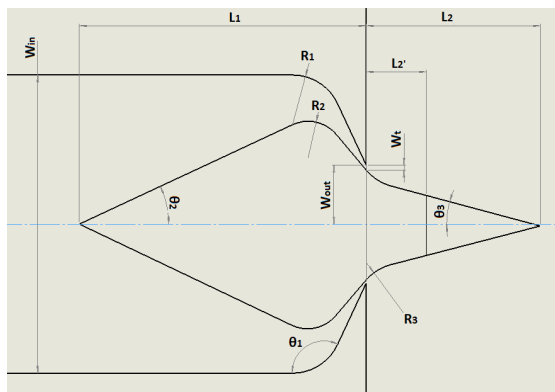


Fig. 9: Aerospike Nozzle Parameters

Mesh: Similar to the Meshing of CD nozzles given that the CFD simulations focus on an aerospike nozzle with a throat size in the order of magnitude of 25-50 μm each, the mesh sizes were selected to sufficiently capture the geometric details and fluid behavior while balancing computational efficiency. For the initial coarse mesh, the parameters selected were a tetrahedral mesh with a maximum element size of 3.18×10^{-4} m, a minimum element size of 9.8×10^{-5} m, a curvature factor of 0.8, a resolution in narrow regions set to 0.5, and a maximum element growth rate of 1.25.

Parametric Sweep: Given the geometric constraints explained above and the increased number of independent design variables, a traditional parametric sweep approach proved infeasible for exhaustively exploring all combinations. An alternative strategy was adopted, centered on a reference geometry, the parameters for which are documented in Row 1 of Table VII.

Each independent set of design variables was systematically altered while keeping others at their reference values.

The Computational fluid dynamics (CFD) simulations were conducted to calculate the corresponding thrust, enabling the formation of a correlation between thrust output and each individual parameter. The effect of varying each parameter is documented in Table VII.

The throat width was limited to only 2 discrete options - 25 μm and 50 μm . As there are two symmetric openings in a single nozzle, the mass flow rate calculation utilizes twice the throat width i.e. 50 μm and 100 μm .

Utilizing these correlations, several nozzle geometries were generated using a mix of individually optimized values ascertained through iterative testing.

Convergence: The convergence criterion was set at a solution tolerance of 1×10^{-3} for the same reasons as those mentioned for the CD nozzle.

Post-processing: The same set of results as in the previous section (for the CD nozzle) are visualized for each parametric combination of the Aerospike nozzle. There is a slight change in the way in which thrust is calculated. As in an aerospike the divergent section (where the flow is allowed to expand) is outside the nozzle exit along the spike, thrust must be calculated at some distance from the flow exit. The plane - across which the momentum flux is integrated - is set at a distance equal to 50% of the spike's length.

V. RESULTS AND SUMMARY

A. Inlet Design

1) *CFD Simulation:* In the steady-state simulations, two sets of results are of particular significance. The first pertains to the velocity distribution at the inlet of the microfluidic channel. Figure 10 illustrates that the new design achieves a more uniform flow distribution compared to the old design. Specifically, the old design exhibits high velocity near the corners of the acceleration chamber inlet and a 40% reduced velocity in the central region. In contrast, the new design maintains a velocity variation of less than 2% across the exit plane, which serves as the inlet for the microfluidic channels.

Figure 11 elucidates the cause of this velocity irregularity in the old design, revealing the presence of a backward flow that spreads outward, thereby increasing the velocity near the walls.

The second significant result is related to pressure drop across the channel, as depicted in Figure 12. Ideally, the pressure drop should be gradual. However, in the old design,

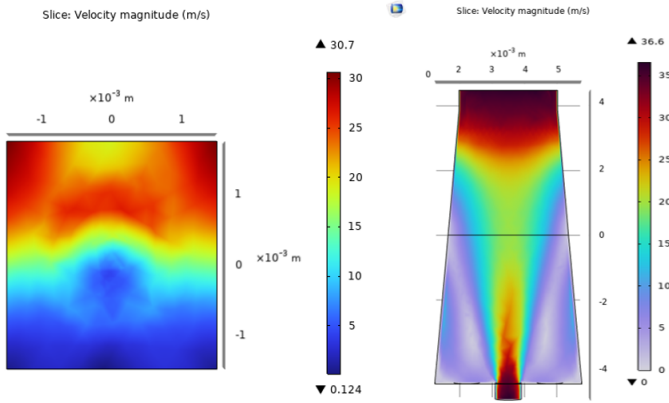


Fig. 10: Top view of Velocity distribution in conventional inlet(left) vs. new integrated inlet(right)

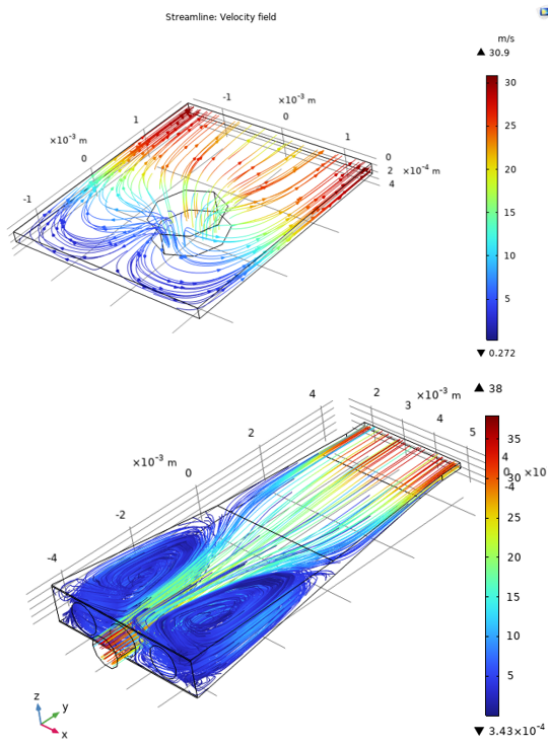


Fig. 11: Velocity streamlines showing direction and magnitude of flow in conventional inlet(top) vs. new integrated inlet(bottom)

the observed non-planar flow (also visible in Figure 11), leads to a low-pressure region near the chamber's center, which is even lower than the exit pressure. This abnormality causes deceleration near the center and could potentially introduce additional flow disturbances, thereby adversely affecting thruster efficiency.

A non-uniform pressure gradient from inlet to outlet can create inconsistent flow velocities and may lead to the development of undesirable flow patterns, causing substantial deviations in the anticipated performance of the thruster [21]. This inconsistency in the flow field is especially detrimental

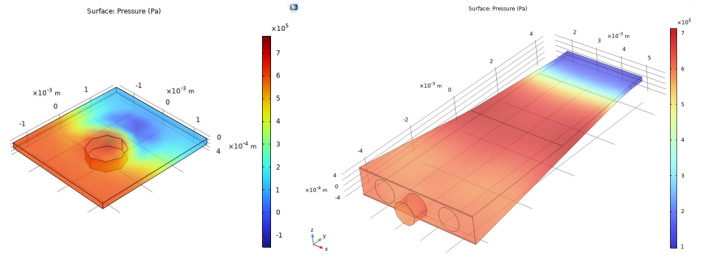


Fig. 12: Pressure drop across conventional inlet(left) vs. new integrated inlet(right)

as it can induce imbalances in the thrust produced, potentially leading to stability issues during operation. The new design addresses and mitigates these anomalies, achieving a uniform pressure drop and eliminating the occurrence of detrimental low-pressure regions, hence reflecting a marked improvement in terms of reliability and performance consistency.

B. CD Nozzle Selection

The goal of this section is to find the optimal shapes - defined as the shape that produces the most thrust for fixed input parameters - for the CD nozzle in order to shortlist them for fabrication. These optimal designs were selected based on comprehensive simulations. The selected nozzle configurations and corresponding simulation outcomes are showcased in this subsection.

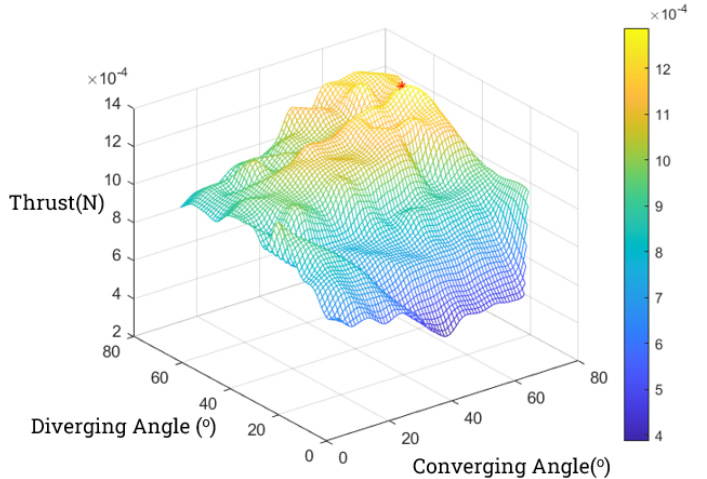


Fig. 13: Value of thrust for all values of θ_d and θ_c with a fixed $AR=10$ $W_t=50 \mu m$. The red asterisk illustrates the maxima.

The nozzle shape resulting in the highest thrust calculation - with all contributing conditions being held constant - were systematically shortlisted. The evaluation of the Knudsen number was conducted in the throat region to identify and eliminate thrusters exhibiting non-continuous flow therein, thus ensuring the seamless operation of the thruster. The culmination of this rigorous selection process yielded final nozzle designs that were predominantly determined by the thrust produced for

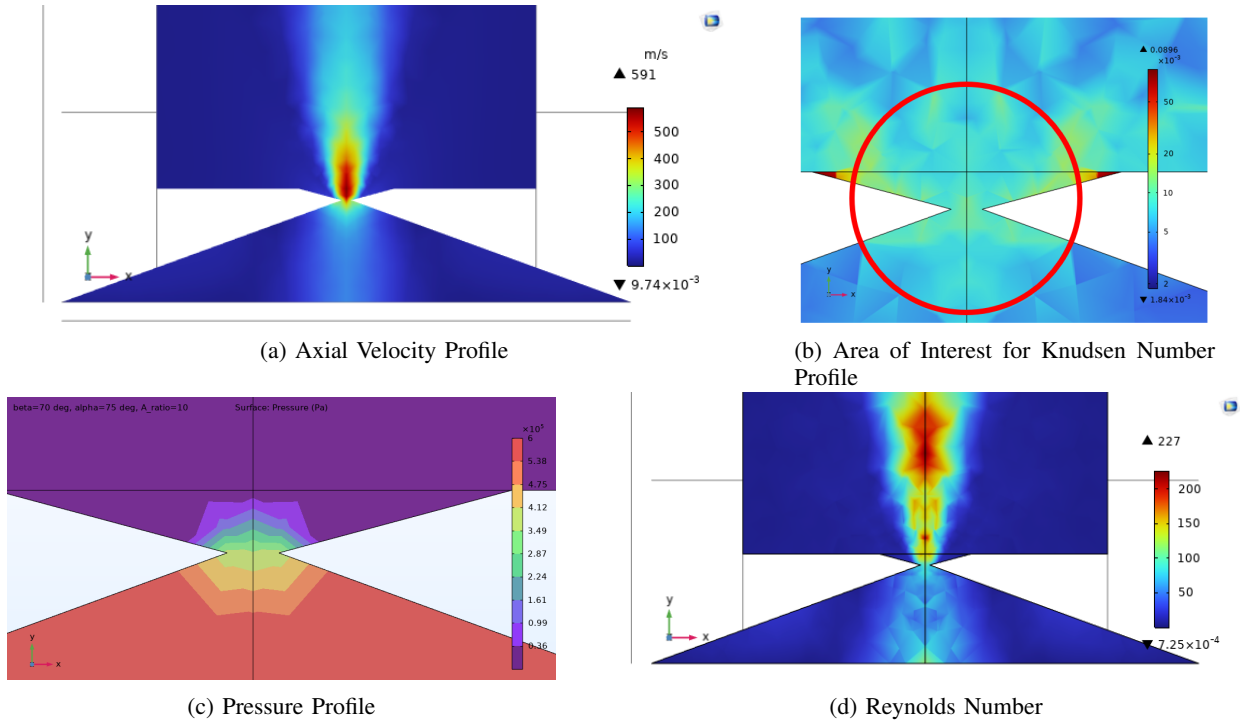


Fig. 14: Results for $\theta_d=70, \theta_c=75, AR=10, W_t=50 \mu m$

each specific throat size (and hence, the corresponding mass flow rate).

Figure 13 illustrates the relationship between thrust and the angles of convergence and divergence, given a constant expansion ratio and throat size. The maxima for this configuration is highlighted with a red mark. The idea of this graph is to show the complex nature of the output, explaining the inherent challenges in formulating a generalized equation to encapsulate the thrust produced by rectangular nozzles relative to their distinctive dimensional parameters.

TABLE VIII: Performance of selected CD nozzles

$W_{throat}(\mu m)$	θ_c	θ_d	ϵ	Thrust (N)	I_{sp} (s)	η_{th}
100	60°	75°	15	0.003558	106.4	65.9%
75	75°	75°	20	0.002661	106.48	66%
50	70°	75°	20	0.001868	112.12	69.5%
25	75°	45°	20	0.001021	122.56	75.9%

Table VIII presents the optimal nozzle configurations corresponding to each throat width, accompanied by additional data on thrust, specific impulse, and nozzle efficiency. The derivation of these values adheres to the methodologies derived in Equation 7, Equation 8 and Equation 11. Given the constraints imposed by the maximal thrust requirements of microsatellites and the overarching power allocation, throat sizes of $50 \mu m$ and $75 \mu m$ emerge as the optimal dimensions. The resultant outputs of the nozzle shape optimized for thrust at a throat width of $50 \mu m$ are illustrated in Figure 14.

In Figure 14a, we observe a distinct axial velocity distribution characterized predominantly by a narrow distribution of extremely high velocity. This is because a large component

of the velocity is directed radially outwards, underscoring the directed nature of the flow. As the nozzle's diverging angle is reduced, there is a palpable decrement in the axial velocity distribution, even though a surge in the maxima can be discerned. The thrust, which is directly influenced by the integral of the velocity, achieves its optimal value at a precise diverging angle for each throat width. Beyond this specific angle, any enhancement in the distribution adversely affects the maxima more adversely than the increase in distribution, thereby decreasing the aggregate summation and ultimately diminishing the thrust.

C. Aerospike Nozzle selection

For the Aerospike nozzles, a throat diameter of $25 \mu m$ was strategically chosen, primarily due to its superior efficiency within the requisite thrust and power range established by the design conditions for micro-satellite applications. The nature of the nozzle, being almost two-dimensional, differs from a conventional aerospike nozzle, which features a continuous circular opening. Contrarily, the MEMS nozzle has only two discrete openings, necessitating doubling of the mass flow rate calculations. The specific parameters pertaining to the elected nozzle design are cataloged in Table IX.

The performance parameters for optimized nozzles of different throat widths (i.e. thrust, I_{sp} and theoretical efficiency) are calculated and tabulated in Table X.

A MEMS aerospike nozzle with an opening of $25 \mu m$ is equivalent to a $50 \mu m$ throat width MEMS CD nozzle in terms of power and mass flow inputs. The velocity profile, pressure drop through the nozzle, the Knudsen number and

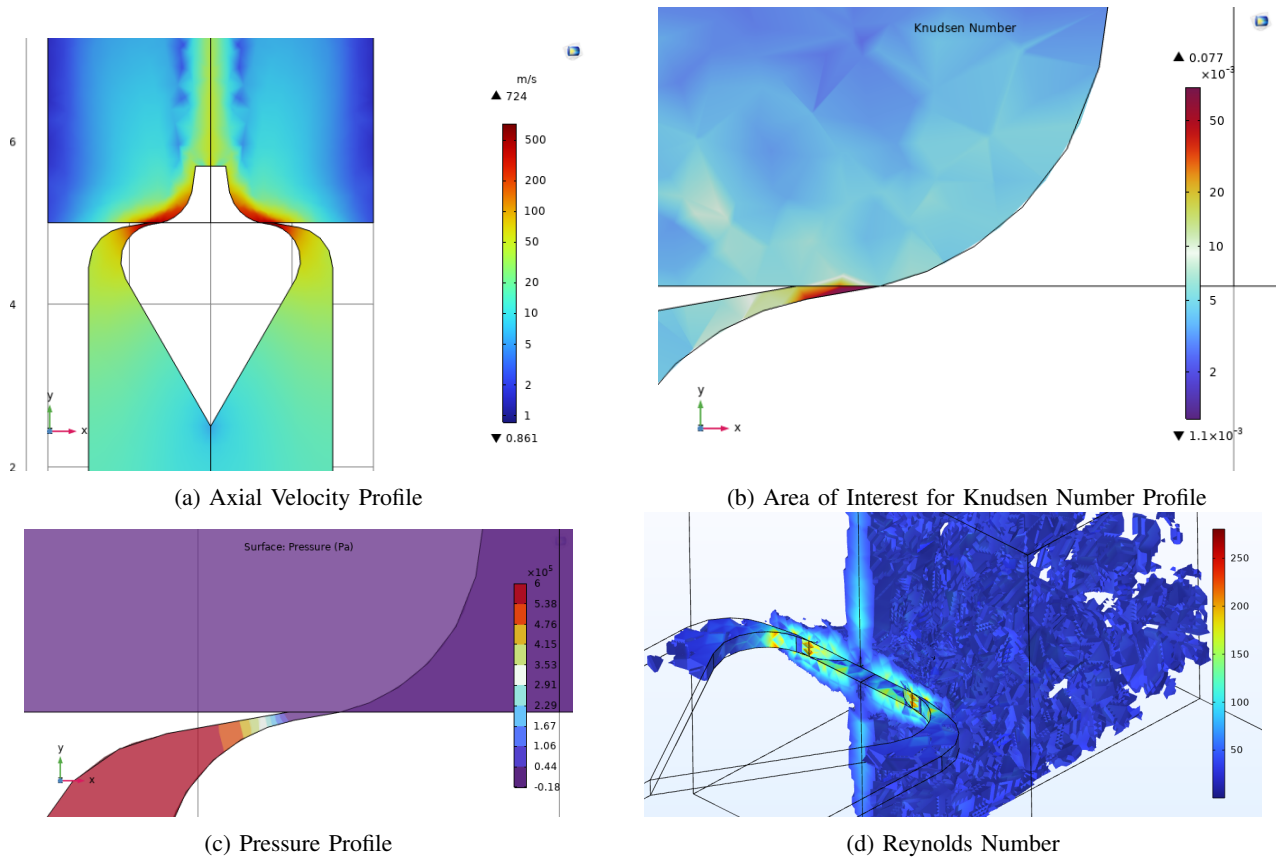


Fig. 15: Results for Optimized Aerospike shape

TABLE IX: Optimized Aerospike Nozzle Parameter Values

variable	value
Convergence angle (θ_1)	100°
Spike Divergence angle (θ_2)	45°
Spike Convergence angle (θ_3)	15°
Throat width (W_t)	$50\mu m$
Inlet width (W_{in})	$3mm$
Spike inward length (L_1)	$1.5mm$
Spike outward Length (W_{in})	$2mm$
Distance between outlets (W_{out})	$1mm$
Fillet radii (R_1, R_2 & R_3)	$0.5mm$
Truncation percentage	0.66

the Reynolds number for the aerospike nozzle shape that produced the highest thrust (all other parameters being fixed) are showcased in Figure 15.

TABLE X: Performance of selected Aerospike nozzles

Throat Width (μm)	Thrust (N)	I_{sp} (s)	η_{th}
2 X 25	0.001321	79.3	50%
2 X 50	0.001998	60	37.2%

VI. CONCLUSION

This study presents a comprehensive optimization of thruster components, culminating in a final design configuration that offers significant advancements over existing literature. Specifically, an average thrust increase of approx-

imately 18% was observed for the same input conditions and temperature, attributable solely to the nozzle redesign, while maintaining the same throat area and consequently the same input mass flow. Additionally, the inlet modifications are expected to enhance the startup flow characteristics, bringing the performance closer to the theoretically modeled results. Future work should focus on the actual fabrication of this optimized thruster design using MEMS fabrication processes to validate the simulated gains in a real-world setting.

VII. AREAS OF IMPROVEMENT

In this section, the potential inaccuracies and limitations inherent to the simulation are delineated.

The implications of the Knudsen number, a dimensionless parameter critical for characterizing the flow regime of gas or vapor propellants, and its variance due to boundary layer selection is a point of consideration. The fluid flow in these propellants is predominantly governed by molecular interactions, displaying pronounced non-continuum effects like flow separation, slip flow, and the formation of Knudsen layers.

Selection of appropriate boundary conditions to model fluid behavior near solid surfaces accurately is an important aspect in Computational Fluid Dynamics (CFD) simulations. A critical component of this selection is the treatment of velocity boundary conditions, specifically focusing on the slip/no-slip condition. The no-slip condition, often employed

for macroscopic flows dominated by molecular interactions and significant viscous effects, posits that fluid velocity is zero at the solid boundary, suggesting full adherence of the fluid to the surface. Conversely, slip conditions, suitable for nanoscale flows, permit relative motion between the fluid and the solid surface, leading to non-zero velocity at the boundary.

Advanced modeling often utilizes the Navier slip condition, incorporating slip length as a continuous function dependent on various parameters like pressure, shear rate, or surface characteristics. This condition offers a comprehensive representation of fluid behavior at the boundary, meticulously considering slip effects and underlying physics.

Given the micro-scale nature of the simulation, determining the most accurate boundary condition presents a challenge, necessitating repeated simulations under all mentioned boundary conditions. The resultant overall velocity profiles exhibited relative consistency, with minor variances observed in the velocity distribution in the throat, and the disparities in maximum velocity, velocity distribution, and produced thrust remained within a 10% delta. However, discernible discrepancies emerged in the visualization of the Knudsen number. Establishing a definitive boundary condition remains complex, with the threshold for thruster shape validity set at a Knudsen number below 0.01 (indication of continuum flow) using Navier-slip conditions with a slip length of 0.5 times the minimum element length.

REFERENCES

- Sheth, V., "Spacecraft Electric Propulsion – A review."
- Khamis, K., "Comparative Study Between MEMS and Conventional Thrusters for Small Spacecraft Micropropulsion."
- "NASA - Linear Aerospike Engine fact sheet (08/00)," publisher: Brian Dunbar. [Online]. Available: <https://www.nasa.gov/centers/marshall/news/background/facts/aerospike.html>
- Sutton, B. O. John Wiley Sons, 2017. [Online]. Available: <https://app.knovel.com/hotlink/toc/id:kpRPEE001A/rocket-propulsion-elements/rocket-propulsion-elements>
- Jahn, R. G. and Choueiri, E. Y., "Electric Propulsion," in *Encyclopedia of Physical Science and Technology*. Elsevier, 2003, pp. 125–141. [Online]. Available: <https://linkinghub.elsevier.com/retrieve/pii/B0122274105002015>
- Speight, J. G., Ed., *Lange's Handbook of Chemistry*, 17th ed. New York: McGraw-Hill Education, 2017. [Online]. Available: <https://www.accessengineeringlibrary.com/content/book/9781259586095>
- Sutton, G. P. and Biblarz, O., *Rocket propulsion elements*, 7th ed. New Delhi: John Wiley & Sons, 2014, oCLC: 914504068.
- Silvestrini, S., "Closed-loop Thrust Magnitude Control System for Nano- and Pico-Satellite Applications."
- Anderson, J. D., *Modern Compressible Flow: With Historical Perspective*, 3rd ed., ser. McGraw-Hill Series in Aeronautical and Aerospace Engineering. Boston: McGraw-Hill, 2003.
- Silva, M. A., Guerrieri, D. C., Cervone, A., and Gill, E., "A review of MEMS micropropulsion technologies for CubeSats and PocketQubes," *Acta Astronautica*, vol. 143, pp. 234–243, Feb. 2018. [Online]. Available: <https://linkinghub.elsevier.com/retrieve/pii/S0094576517304290>
- Fredrickson, C. K. and Fan, Z. H., "Macro-to-micro interfaces for microfluidic devices," *Lab on a Chip*, vol. 4, no. 6, p. 526, 2004. [Online]. Available: <http://xlink.rsc.org/?DOI=b410720a>
- Fontanarosa, D., Francioso, L., De Giorgi, M. G., and Vetrano, M. R., "MEMS Vaporizing Liquid Microthruster: A Comprehensive Review," *Applied Sciences*, vol. 11, no. 19, p. 8954, Sep. 2021. [Online]. Available: <https://www.mdpi.com/2076-3417/11/19/8954>
- Cervone, A., Zandbergen, B., Guerrieri, D. C., De Athayde Costa E Silva, M., Krusharev, I., and Van Zeijl, H., "Green micro-resistojet research at Delft University of Technology: new options for Cubesat propulsion," *CEAS Space Journal*, vol. 9, no. 1, pp. 111–125, Mar. 2017. [Online]. Available: <http://link.springer.com/10.1007/s12567-016-0135-3>
- de Athayde Costa e Silva, M., "Mems micropropulsion: Design, modeling and control of vaporizing liquid microthrusters." Ph.D. dissertation, Delft University of Technology, 12 2018, promotor: E.K.A. Gill, Copromotor: A. Cervone. [Online]. Available: <https://doi.org/10.4233/uuid:57f725e1-b3f3-455c-83ce-9156b2123c88>
- Liu, B., Li, X., Yang, X., Yang, J., Wang, Y., Li, D., and Gao, G., "A new vaporizing liquid microthruster with planar induction heating," *Sensors and Actuators A: Physical*, vol. 308, p. 112010, Jun. 2020. [Online]. Available: <https://linkinghub.elsevier.com/retrieve/pii/S0924424719307009>
- Mele, L., Santagata, F., Iervolino, E., Mihailovic, M., Rossi, T., Tran, A., Schellevis, H., Creemer, J., and Sarro, P., "A molybdenum MEMS microhotplate for high-temperature operation," *Sensors and Actuators A: Physical*, vol. 188, pp. 173–180, Dec. 2012. [Online]. Available: <https://linkinghub.elsevier.com/retrieve/pii/S0924424711006820>
- Srinivasan, R., Hsing, I., Berger, P. E., Jensen, K. F., Firebaugh, S. L., Schmidt, M. A., Harold, M. P., Lerou, J. J., and Ryley, J. F., "Micromachined reactors for catalytic partial oxidation reactions," *AICHE J*, vol. 43, pp. 3059–3069, 1997.
- Firebaugh, S. L., Jensen, K. F., and Schmidt, M. A., "Investigation of high-temperature degradation of platinum thin films with an in situ resistance measurement apparatus," *J. Microelectromech. Syst.*, vol. 7, no. 1, pp. 128–135, Mar 1998, [Online]. Available: <http://ieeexplore.ieee.org/stamp/stamp.jsp?arnumber=661395>.
- Ali, S. Z., Udrea, F., Milne, W. I., and Gardner, J. W., "Tungsten-based soi microhotplates for smart gas sensors," *J. Microelectromech. Syst.*, vol. 17, no. 6, pp. 1408–1417, Dec 2009, [Online]. Available: <https://www.researchgate.net/publication/224349026>.
- Spernovasilis, G., "Design and fabrication of smart vaporizing liquid microthruster for Cubesat applications."
- Hadjadj, A. and Onofri, M., "Nozzle flow separation," *Shock Waves*, vol. 19, no. 3, pp. 163–169, Jul. 2009. [Online]. Available: <https://link.springer.com/10.1007/s00193-009-0209-7>

4 | Fabrication and Characterisation of VLM Microthrusters

“You shouldn’t do things just because they’re different. They need to be better. If you’re going to make a product, make it beautiful”

– Elon Musk, 1971 -Present

Characterizing an Improved MEMS Fabrication Process for Vaporizing Liquid Micro-resistojet Microthrusters

S.I. Singh*, A. Cervone[†], M.Ghatkesar*, H. van Zeijl[‡]

*Precision Mechanism Engineering, Mechanical Engineering Faculty, Mekelweg 2, 2628CD Delft, TU Delft, The Netherlands

[†]Space Engineering Department, Aerospace Engineering Faculty, TU Delft, Kluyverweg 1, 2629HS Delft, The Netherlands

[‡]Else Kooi Laboratory, EEMCS Faculty, TU Delft, Feldmanweg 17, 2628CT Delft, The Netherlands

Abstract—This paper presents a comprehensive study on the fabrication and characterization of Micro-Electro-Mechanical Systems (MEMS) based Vaporizing Liquid Micro-Resistojet (VLM) thrusters. A streamlined fabrication process is introduced, significantly reducing the number of fabrication steps and time required, while enhancing the accuracy and repeatability of the produced thrusters. Following the fabrication, a rigorous characterization regime is implemented to assess both mechanical and electrical attributes of the micro-thrusters. Experimental data, including measurements from fabricated wafers, confirm noteworthy improvements in fabrication fidelity. The mechanical and electrical characterizations further validate the performance gains in the newly fabricated VLM thrusters, offering a promising advancement in MEMS-based propulsion systems. The findings not only contribute to the evolving landscape of micro-propulsion but also provide a robust and efficient fabrication process for future research and commercial applications.

Index Terms—microthruster, MEMS, VLM, fabrication, charecterization

I. INTRODUCTION

A. VLM Microthrusters

Vaporizing Liquid Micro-thrusters (VLMs) are a subclass of micro-propulsion systems specifically designed for nano- and pico-satellites. VLMs serve as highly miniaturized propulsion units capable of precise thrust modulation. The core operating principle revolves around the use of a resistive heating element to vaporize a liquid propellant. Upon vaporization, the propellant is expelled at high velocities through a micro-nozzle, generating the required thrust for various in-orbit maneuvers such as attitude control, station-keeping, and orbital transfers.

The advantages of VLMs are multi-fold: they offer a high thrust-to-power ratio, low power consumption, and are compatible with a range of liquid propellants, including green options. Owing to their architecture, VLMs can be efficiently integrated into small satellites without significantly impacting the overall mass or power budget, thereby making them an attractive propulsion option for modern, miniaturized spacecraft.

In summary, Vaporizing Liquid Micro-thrusters are an innovative class of propulsion systems that offer a compact and efficient solution for propulsive requirements of nano- and pico-satellites. Their unique operating mechanism and advantageous characteristics position them as a promising

technology in the rapidly evolving field of small satellite propulsion.

B. MEMS fabrication of microthrusters

Micro-Electro-Mechanical Systems (MEMS) fabrication is a multi-step process that combines both electrical and mechanical components at the microscale to produce highly integrated devices. Typical MEMS fabrication processes include photolithography for pattern definition, thin-film deposition for material addition, and etching for material removal. Given the extreme miniaturization involved, MEMS processes often require high precision and control.

When it comes to Vaporizing Liquid Micro-thrusters (VLMs), MEMS fabrication plays a critical role. VLMs are complex systems incorporating fluidic channels, heating elements, and nozzles, all of which need to be fabricated with high accuracy to meet the stringent performance criteria. Photolithography can be employed to define intricate channel geometries for fluid flow, whereas thin-film deposition techniques can be used to form the resistive heating elements. Subsequently, deep reactive-ion etching (DRIE) or other specialized etching techniques may be utilized to construct the micro-nozzles through which the vaporized propellant is expelled.

The MEMS fabrication process for VLMs is particularly challenging due to the need to integrate these multiple components on a single silicon wafer while ensuring that they function in harmony during operation. Any misalignment or variation in dimensions could significantly affect the thruster's performance and efficiency. Hence, MEMS fabrication techniques offer the high precision and scalability required to produce reliable and efficient VLMs suitable for space applications.

C. Fabrication state of the art

Silva et al. [1] from TU Delft fabricated a VLM with integrated molybdenum heaters and temperature sensing in 2018. Karthikeyan et al. [2] designed and manufactured a VLM using low-temperature co-fired ceramic (LTCC) as the material due to the good electrical conductivity of printed metallization and a relatively low production cost. Cheah and Low [3] successfully tested a high-temperature co-fired ceramic (HTCC) microthruster characterized by a platinum-based microheater integrated on a three layers structure.

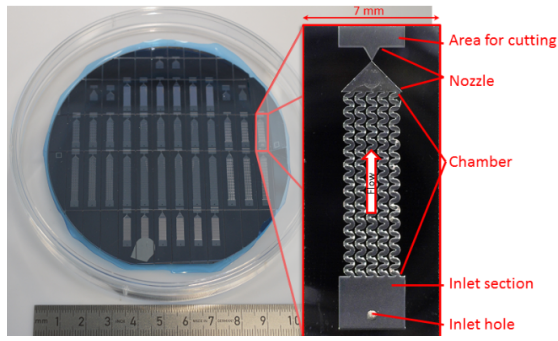


Fig. 1: Parallel multi-shaped channel VLM, 2018 [4]

Liu et al. [5] developed a tubular concept of a VLM equipped with a micro-heater core, an excitation coil, a vaporizing chamber, and the micro-nozzle, all integrated into a glass tube obtaining a thrust of $680\mu\text{N}$ at 5mg/s . Kwan et al. [6] designed a water-fed VLM operating in the Leidenfrost boiling regime. The device was equipped with miniature molybdenum heating elements located inside the vaporization chamber.

Fontanarosa et al. [7] at University of Salento designed and fabricated a silicon-based water-propellant VLM equipped with embedded microsensors for real-time monitoring of the in-channel vapor/liquid fraction and fluid temperature during its operation. Further, a secondary low-power platinum thin-film resistive heater was placed inside each of the eight channels, allowing for localized precision fluid heating and flow control. A preliminary characterization of the embedded sensors demonstrated the operational feasibility of the fabricated microthruster, enabling a fine heating effect localization and vaporization control.

II. FABRICATION OF VLM MICROTHRUSTER

A. Design for fabrication

The design for fabrication consists of 4 sub-designs. The inlet, the heating chambers, the outlet nozzles and the heating elements.

1) *Micro-fluidic Inlet*: This paper presents an evolution of inlet design in MEMS micro-thrusters. Previously, these thrusters employed basic inlets, which were simply wells at the ends of fluidic channels [8]. These inlets necessitated the fabrication of a through-hole in the silicon substrate to facilitate the attachment of the inlet component.

The newly proposed design introduces specialized interconnects that should align perfectly with the inlet. This feature elevates the device's functionality while demanding unique fabrication considerations. Specifically, within the context of MEMS thruster fabrication, this design necessitates a specialized dicing process. A portion of the silicon material must be selectively removed, a procedure executed through partial dicing, thereby leaving the underlying glass layer undisturbed. This refined dicing process sets the stage for the successful integration of the advanced inlet design,

thereby marking a departure from traditional fabrication approaches.

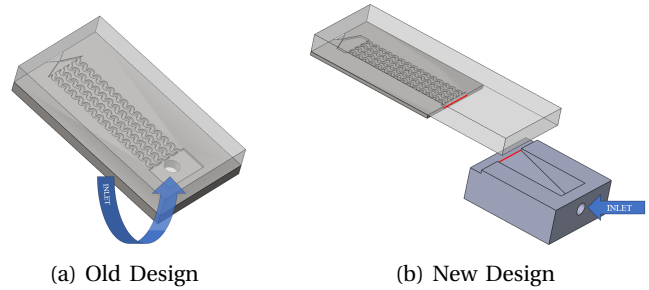


Fig. 2: Inlet Design for VLM : (a) inlet through hole for propellant delivery; (b) inlet attaches to glass (red marked edges will mate) giving in plane inflow

2) *Microfluidic Channels*: The geometry adopted for the heating and vaporization chamber is a serpentine layout designed to optimize the interaction between the heated silicon substrate and the liquid propellant. The serpentine geometry offers an increased surface area for heat exchange, thereby enhancing the efficiency of thermal transfer. Empirical models demonstrate that this configuration permits effective vaporization and subsequent heating of the propellant to approximately 700 K while minimizing power consumption. Figure 3 presents the dimensional details of a single serpentine section. To reach the target temperature of 700 K , the cumulative length of the serpentine channel is calculated to be approximately 9 mm , which necessitates 14 repetitions of the serpentine pattern. The overall channel width being 3 mm allows for 5 parallel channels. This channel geometry will be etched into the silicon substrate, located on the side opposite to the heaters. It is the conduit between the inlet and nozzle sections.

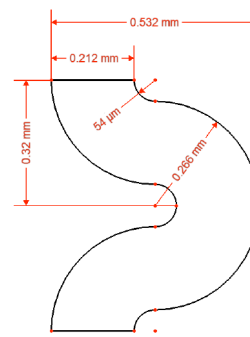


Fig. 3: Serpentine Channel dimensions for one section [1]

3) *Nozzle design*: 3 types of Nozzles were shortlisted for fabrication:

- Traditional Convergent Divergent Nozzle (CD Nozzle)
- Bell shaped CD Nozzle
- Aerospike Nozzle

Each of these shapes were simulated using CFD and the optimal shapes for each were chosen for fabrication. A few

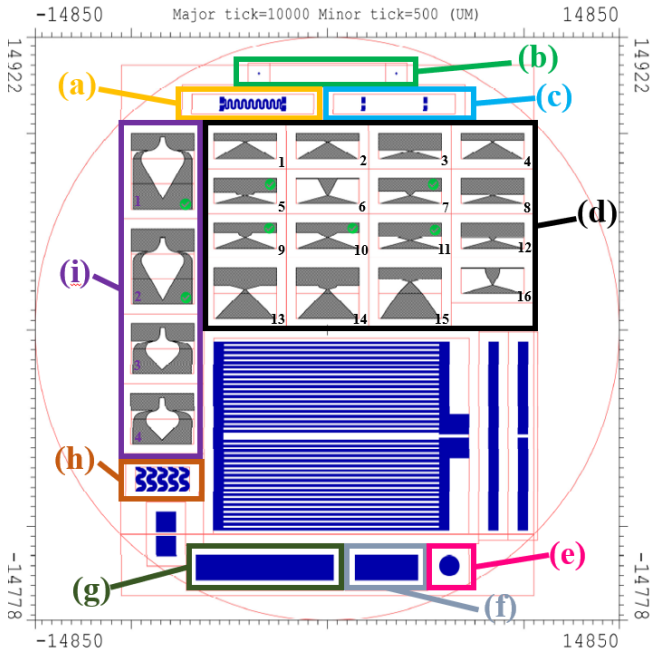


Fig. 4: Mask Image layout - left: Design and image categorization ; right: fabricated mask mirror image

different throat widths were chosen for each nozzle type for their respective mass flow rate and thrust properties. For the CD and bell shaped CD nozzles these are highlighted in Table I. For Aerospike Nozzles the selected dimensions are showcased in Table II.

Throat width	Converging angle	Diverging angle	Expansion ratio
25 μm (Figure 4(d-07))	75 $^{\circ}$	45 $^{\circ}$	20
50 μm (Figure 4(d-10))	70 $^{\circ}$	60 $^{\circ}$	20
75 μm (Figure 4(d-11))	75 $^{\circ}$	75 $^{\circ}$	20

TABLE I: Selected Dimensions for simple CD nozzle

Throat width	25 μm	50 μm
Inlet spike angle	30 $^{\circ}$	30 $^{\circ}$
Outlet spike angle	5 $^{\circ}$	5 $^{\circ}$
Inlet spike Length	2.5 mm	2.5 mm
Outlet spike Length	0.66 mm	0.66 mm
Radius inlet inner	0.45 mm	0.45 mm
Radius inlet outer	0.5 mm	0.5 mm
Radius Outlet	0.6 mm	0.6 mm
Distance between outlets	1.5 mm	1.5 mm
Angle Inlet Convergence	100 $^{\circ}$	100 $^{\circ}$

TABLE II: Selected Dimensions for Aerospike nozzle

Other nozzle layouts were also prepared, but have not been manufactured in this study and are listed in Appendix.

4) *Heater specifications*: Titanium, due to its high operating temperature, has high accuracy and relatively simple processing and is the chosen material for this work.

The Heater design was chosen for consistent temperature distribution across the resistance. The temperature distri-

bution is largely influenced by the substrate material and thickness. Silicon acts as a heat spreader and thicker silicon membranes require a smaller variation in pitch and width to achieve the same temperature uniformity [9].

The heaters are to be positioned opposite the micro-channels. in the same length of 9 mm, 8 heaters can be fit at a pitch of 1 mm.

B. Wafer Layout and Mask Fabrication

1) *Modular Cell Layout on wafer*: In the MEMS process multiple thrusters can be fabricated on a single wafer. In order to integrate multiple designs on a single wafer using a modular approach the wafer was split into cells of a customized size. Based on the serpentine channel dimension chosen, the height of the cell was chosen to fit two such sections, giving a value of 1.28 mm. The width of the cell would be the horizontal size of the thruster at 7 mm(3 mm channel width with a 2 mm wall on both sides). These cells were distributed across the wafer as shown in Figure 5.

In each of these cells a certain design of the thruster would need to be fit. This means all the components required need to be modularized into cells of the same size that can be arranged as required to produce the overall shape required.

Items that are smaller than the cell size like the heaters, bonding pads,etc. can be positioned as required within the cells. However, larger shapes like the Aerospike Nozzles would need to be designed to fit in 3 consecutive cells.

2) *Photo Mask*: A photo mask, consisting of an opaque layer of chrome on a glass substrate, was fabricated at



Fig. 5: Wafer configuration : left - an example of modular layout of thruster images in cells(black) ; right - distribution of thrusters across wafer (green signifies nozzle image, yellow is channel and blue is blank image for inlet or spacing, grey implies no image)

Compugraphics. The mask design consisted of the following designs:

- 9 simple convergent divergent nozzles (3 for fabrication, 6 for possible future use) - Figure 4(d)
- 7 bell shaped convergent divergent nozzles (3 for fabrication, 4 for possible future use) - Figure 4(d)
- 4 Aerospike nozzles (2 for fabrication, 2 for future use)- Figure 4(i)
- Heater design - Figure 4(a)
- Bonding Pads - Figure 4(c)
- Serpentine channel section - Figure 4(h)
- Blank Image channel width (3.2 mm) - Figure 4(f)
- Hole image for old inlet design - Figure 4(e)
- Blank image thruster width (7 mm) - Figure 4(g)
- Dicing markers - Figure 4(b)
- Other images for LPM (Low Pressure Micro-resistojet thrusters) - Figure 4(unmarked)

3) *Wafer Configuration*: Upon finalizing the mask images for various thruster designs, the next step involves determining their spatial arrangement on each silicon wafer. As outlined earlier, the wafer surface is partitioned into designated cells that serve as building blocks for assembling diverse thruster configurations using modular mask images. These configurations, including all the elements - nozzle outlets, acceleration chambers, heaters, old or new inlet designs - are systematically arranged within these cells. An exemplar thruster layout, consisting of a three-cell Aerospike Nozzle, a seven-cell serpentine acceleration chamber equipped with eight heaters, and an older inlet

design featuring a through-hole, is depicted in Figure 5(left).

Horizontal spacing between thruster configurations is not necessary, as each design occupies only 3.2 mm in width, whereas the cell dimensions are 7 mm. This difference in dimensions ensures adequate silicon substrate thickness between adjacent thruster units. Vertically, additional cells are left vacant to facilitate the dicing process, which separates individual thrusters. After optimizing for spatial efficiency, the layout that maximizes the number of thrusters per wafer was selected. Figure 5(right) illustrates an example layout, showcasing the distribution of 46 distinct thrusters across a 100 mm diameter wafer. This figure also provides insights into the spatial distribution of various thruster configurations on the wafer.

C. Detailed MEMS fabrication process

The microthrusters were fabricated in a Class 100 clean-room at the Else Kooi Laboratory (EKL) of TU Delft, following stringent protocols for microelectromechanical systems (MEMS) production. The base material was a 4-inch (100 mm), double-side polished silicon wafer with a thickness of 300 μm . The simplified schematic for the improved process to fabricate the new thruster design is shown in Figure 6. The fabrication steps in relation to the schematic are detailed in this section.

(a) The initial stage of the fabrication involved the deposition of a 500 nm PECVD (Plasma-enhanced Chemical Vapor Deposition) TEOS (tetraethoxysilane) layer on the front side silicon wafer, designated as the heater side, to act as an

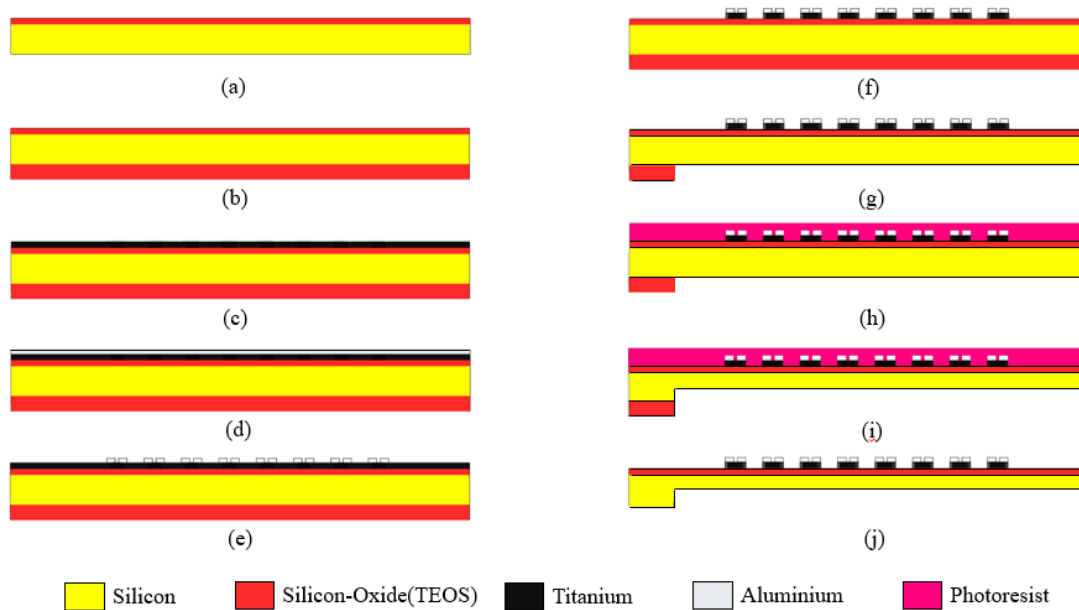


Fig. 6: Section Plane showing the various steps involved in Fabrication of VLM thrusters on a Silicon Wafer

electrical insulator between the substrate and the heater elements.

(b) On the backside of the wafer, designated as the thruster side, a $4\ \mu\text{m}$ layer of TEOS was deposited, using the same PECVD process, to serve as a hard mask for silicon etching.

(c) A $500\ \text{nm}$ layer of titanium was then sputter-deposited onto what is designated as the heater side of the wafer. This layer functions as the heating element for the microthruster. The main principle of sputter coating involves generating a metal plasma that is deposited on the sample.

(d) A $200\ \text{nm}$ layer of aluminium was also sputter-deposited atop the titanium for the formation of bonding pads. In Aluminium sputter-coating the target layer consists of of 99% Al and 1% Si due to the nature of the process.

(e) Photolithographic techniques employing photoresist were employed to define the mask patterns for the bonding pads, which were then etched using a wet-etch process with a buffered aluminium etching solution (phosphorus acid, nitric acid, acetic acid and deionized water) for 2 minutes. The photoresist was stripped using a TEPLA oxygen plasma system.

(f) A fresh layer of photoresist was applied, exposed, and developed to permit the selective etching of the titanium heaters. The titanium layer was then etched at $35\pm 1^\circ\text{C}$ for roughly 26 seconds using a titanium-specific etchant. Post etching, the photoresist was stripped again via TEPLA oxygen plasma system.

(g) On the thruster side, soft masks of the thruster design were generated using photoresist, which subsequently underwent reactive ion etching (RIE) to pattern the Silicon Oxide layer.

(h) A thick layer of photoresist, $6\ \mu\text{m}$, was coated on

the heater side to protect the heaters and the silicon oxide insulation layer during the subsequent steps.

(i) Back on the thruster side, With the oxide layer now acting as a hard mask, the thruster cavities were etched into the silicon substrate via a combination of isotropic and anisotropic deep reactive ion etching (DRIE). The isotropic etching was specifically employed to ensure that narrow channels were etched as vertically as possible.

(j) The Silicon oxide on the thruster side was completely removed using wet etching in a buffered hydrofluoric acid (BHF) bath. If HF was used directly, it would have had too fast and aggressive a action on the oxide which is why a "buffered" solution, which can keep the etch rate low and constant by moderating the PH level of the bath, was used [10]. The protective Photoresist layer is also removed in an Acetone bath, re-exposing the heaters.

Finally, the silicon wafer was anodically bonded to a glass wafer at $400\pm 5^\circ\text{C}$ and $1000\ \text{V}$, serving both as a substrate and providing visual access for internal flow dynamics studies.

The final step in the fabrication process involved dicing the bonded wafers. A two-step dicing strategy was employed; initially, partial dicing removed only the silicon layer, preserving the glass layer for inlet bonding. Subsequently, full dicing separated individual thruster units. Dicing markers were previously etched into the front-side silicon oxide layer to guide this operation.

D. Assembly

Once the wafer is diced, the individual thrusters are considered fabricated. However, to be functional, the microfluidic inlet must be assembled and hermetically sealed. As explained in the design and dicing process, $2.56\ \text{mm}$ of Silicon is diced off, leaving only the glass layer. This

removal of the Silicon layer is strategic, as it allows for a clean, unobstructed glass surface to which the new inlet component can be bonded. The new inlet component must then be aligned and bonded to this glass layer, while maintaining perfect alignment with the inlet.

For ensuring a vacuum-tight connection between components, a hermetic sealing process is applied during the inlet bonding stage. This sealing process not only provides mechanical strength but also prevents any potential leakage, ensuring the integrity of the microfluidic pathways.

In practice this would be done as a final step within the clean room processing using optical alignment and sealing using one of the following techniques:

- Using a Laminate layer
- Using an intermediary layer like Benzocyclobutene (BCB)
- Using UV-sensitive negative photoresist based on epoxy resin

In the present experiment, a simpler approach was employed as a proof-of-concept for inlet fabrication and bonding. Channels of varying depths, ranging from $25\mu\text{m}$ to $100\mu\text{m}$, were fabricated on the bonding surfaces of the inlet using Stereolithography (SLA) 3D printing technology. For adhesive bonding, LOCTITE®EA 9492 epoxy adhesive was utilized to attach the inlet to both the glass layer and the silicon substrate on the backside. This epoxy was specifically chosen for its high chemical resistance and temperature stability, making it suitable for structural bonding applications in microthruster environments. Additionally, the adhesive exhibits low outgassing characteristics, which make it an ideal intermediary for achieving a hermetic bond between resin and silica components. Moreover, the epoxy possesses enhanced thermal shock and impact resistance properties. Upon experimental validation, a channel depth of $50\mu\text{m}$ was found to be sufficient for achieving both accurate assembly alignment and a hermetically sealed bond.

E. Fabrication Challenges and Concerns

Unanticipated Oxide Deposition on Backside: During the deposition of the thick layer of TEOS oxide on the thruster side, substantial deposition was observed on the backside, predominantly around the regions near the wafer clamps. This unforeseen layer, which turned out to be discernible in subsequent processing steps, prompted a shift in the deposition step to precede the metallization steps. This arrangement meant any additional layer resulted in silicon-to-silicon contact. Given the thin nature of this unintentional layer, estimated at 50nm or below in the heater region, its impact on performance is anticipated to be minimal.

Handling Thin Wafers: Utilizing a thin wafer of $300\mu\text{m}$, essential for optimizing heater proximity to the channels, presented challenges in terms of mechanical stability. Two wafers were lost owing to fractures during the oxide

etching process. This was attributed to the mechanical clamping mechanism of the etcher, underscoring the need for gentler handling techniques or alternative clamping systems.

Adhesion Issues with Protective Photoresist: During the treatment of wafer 7, which served as a pilot for testing before scaling up, the protective photoresist layer showcased adhesion problems. Potential causes include the omission of the Hexamethyldisilazane (HMDS) adhesion promoter step or inconsistencies during the centrifugal application of the resist. This compromised protection during the final oxide removal, resulting in the loss of the insulation layer for nearly 40% of the thrusters on that wafer.

Variability in Silicon Etching: The silicon etching recipe, theoretically designed for a steady etch rate of $2.4\mu\text{m}$ per cycle, displayed a diminishing rate with increased depth. Preliminary tests on wafer 7 indicated an average depth of $130\mu\text{m}$ post 64 cycles. Subsequent wafers underwent 75 cycles to achieve the target depth of $150\mu\text{m}$. The etch profile also displayed a consistent undercut, suggesting the need for further refinement to attain a more perpendicular etch profile.

Issues with Glass Bonding: The pilot wafer displayed a noticeable crack near its center post the glass bonding process. Preliminary analysis suggests this might stem from the defects introduced due to the improperly applied photoresist layer.

Wafer Handling Considerations: Handling dual-sided wafers introduced certain defects. Enhanced care during manual wafer handling, coupled with minimizing process repetitions, which occasionally arose due to either manual mishaps or equipment malfunctions, can mitigate such defects.

These insights garnered from the fabrication process serve as pivotal learning points, offering direction for refining fabrication processes in future iterations.

III. MECHANICAL CHARACTERIZATION

A. Methodology for Mechanical Characterization

Instrumentation:

- 1) **Hitachi Regulus 8230 Scanning Electron Microscope (SEM)**
This instrument is chiefly used for its ability to provide high-resolution images, which are invaluable for the analysis of surface morphology, grain structure, and identification of defects such as cracks or voids.
- 2) **Keyence Laser Microscope**
This microscope is tailored for surface topography measurements, particularly surface roughness and in-plane feature dimensions.

3) Dektak Stylus Profiler

The Dektak profiler is employed for its proficiency in delivering detailed surface profiles and for measuring feature heights and depths.

Parameters and Procedures:

1) Surface Morphology and Grain Structure:

- **Instrument Used:** Scanning Electron Microscope (SEM)
- **Procedure:** The microthruster samples are prepared using standard protocols and are then mounted for imaging in the SEM. A meticulous examination - by imaging the various features - gives the surface morphology and grain structure.

2) Feature Dimensions (In-Plane and Depth):

- **Instruments Used:** SEM and Keyence Laser Microscope for in-plane dimensions; Keyence Laser Microscope and Dektak Stylus Profiler for feature depth
- **Procedure:** A synergistic use of all instruments is advocated for a comprehensive understanding of feature dimensions. The Keyence microscope and SEM scan and measure in-plane dimensions. To determine depth or to image different depths within a sample using the laser microscope, the focal plane of the microscope is moved vertically (z-direction) by adjusting the objective lens position relative to the sample. At each vertical position, an image is captured, corresponding to that specific depth in the sample. By collecting images at different depths, a three-dimensional representation of the sample can be constructed. The difference in position between the focal planes of these successive images provides depth information. The Dektak profiler performs physical step-height measurements to determine feature depths.

3) Surface Roughness:

- **Instrument Used:** Keyence Laser Microscope
- **Procedure:** The microthruster samples are secured on the stage of the Keyence microscope. Using the 3D topographic map, various roughness parameters can be calculated. The most common parameter, R_q (root mean square roughness), is the root-mean-square of absolute height deviations from the mean line over a specified distance.

4) Presence of Defects (Cracks, Voids):

- **Instrument Used:** SEM
- **Procedure:** SEM micrographs are scrutinized to identify any defects like cracks or voids. These defects could potentially affect the mechanical properties and performance of the microthrusters.

By adhering to the outlined methodology, a comprehensive mechanical characterization of MEMS microthrusters is achieved. This approach strategically minimizes the duplication of measured parameters while providing a thorough assessment of essential features and properties crucial for microthruster performance.

B. Results for Mechanical Characterization

1) *Surface Morphology and Grain Structure:* Some interesting graphs from SEM imaging are shown in this section that give insights on a molecular level distribution of materials on the Silicon. The Silicon substrate and oxide layer show inherent smoothness. However, a detailed observation of the sputtered titanium layer indicates inconsistencies in deposition as shown in Figure 7.

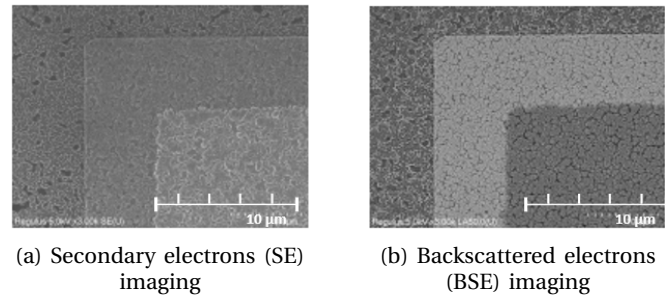


Fig. 7: SEM - Aluminium bonding pads on Titanium heater on Oxide layer

The Aluminum layer also does not exhibit its characteristic crystalline structure and is instead relatively inconsistently sputtered as shown in Figure 8

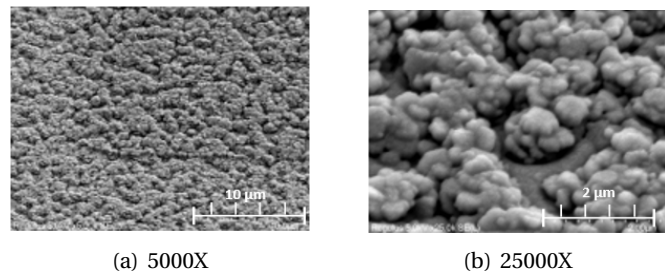


Fig. 8: Aluminum on Titanium morphology

2) *Feature Dimensions:* In this section Images of some key features are showcased. These include the heater, bonding pads, nozzle throat and serpentine channels.

A key result is visualized in Figure 9. Here an image is taken at a 45° angle of a nozzle throat. Features of note include, the scallops, clearly visible along the side walls of the etch. Another visible feature is the inclination as the etch depth increases. Lastly, some small artifacts can be noticed in the base of the structure where the throat intersects the bottom surface.

Figure 10 visualizes the serpentine channel at its inlet. It shows a tidy and accurate etch of the design in the silicon. As the image is taken at an angle, it is also possible to calculate the height as shown in the figure. This image from the test wafer gave an idea of the depth achieved with the initial recipe, which was then modified to reach a etch depth of $150 \mu\text{m}$.

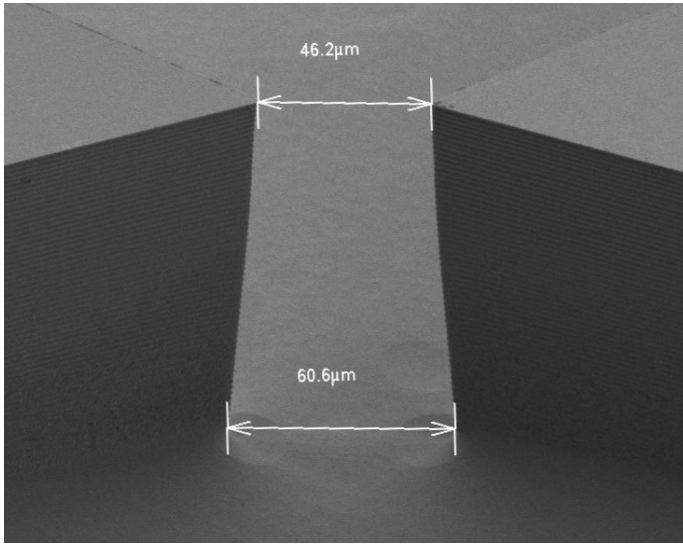


Fig. 9: Magnified view of a $50\mu\text{m}$ CD nozzle throat

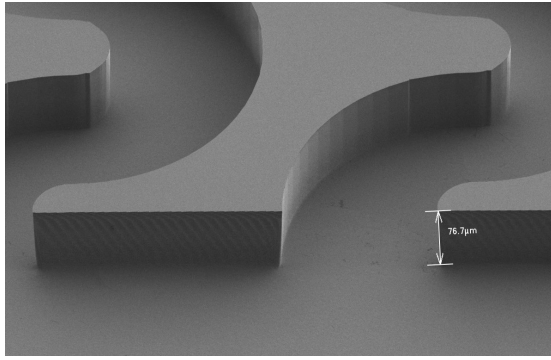
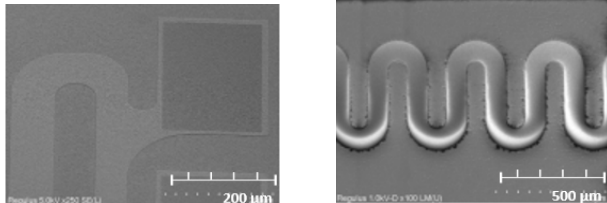


Fig. 10: A serpentine channel inlet for the test wafer observed at 35° . The true height is $76.7/\sin(35)=133.7\ \mu\text{m}$

Figure 11 shows the titanium heater and bonding pads in detail. The imaging is done at an angle, so again the layer heights can be approximated (although this was done during the fabrication process after deposition as well). The titanium was measured across 15 ample thrusters to be in a range of 440 nm to 510 nm. The Aluminium was measured to be 180 nm to 210 nm. The in-plane dimensions are extremely accurate with a standard deviation of 120 nm from the designed values.



(a) titanium heater and bonding pad

(b) Top view of heater element

Fig. 11: SEM imaging of heater features

Figure 12 shows a 3D image created by stitching together multiple layer scans. This imaging method was used to accurately measure all the actual dimensions of the thrusters.

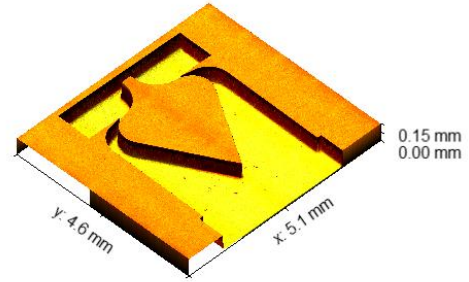


Fig. 12: Stitched 3D imaging from laser microscope (scaled in z-direction). Used for measuring all dimensions and to generate surface roughness data.

The final deviation of the fabricated dimensions from the design is showcased in Figure 13. The average standard deviation of all the measured dimensions from the nominal design was $0.8\ \mu\text{m}$. The previous study by Silva et. al. [1] achieved a 40% to 60% difference in the throat width and a -5% to 25% difference in the serpentine width. in contrast the new fabrication has a deviation of less than $\pm 5\%$ in the same features.

3) *Surface Roughness*: The surface roughness results for the various Silicon layers are noted in this section. For each wafer 5 sample points were tested. Sample 1 is near the center, Sample 2 to Sample 5 are clock wise from thrusters near the top to those near the left edge of the wafer.

	Sample 1	Sample 2	Sample 3	Sample 4	Sample 5
Wafer 1	92.5nm	90.1nm	88.8nm	92.2nm	92.3nm
Wafer 2	82.2nm	88.8nm	81.6nm	86.4nm	90.1nm
Wafer 3	91.5nm	91.1nm	90.2nm	91.2nm	93.3nm

TABLE III: Root mean Square surface roughness - Top layer of thruster (Si)

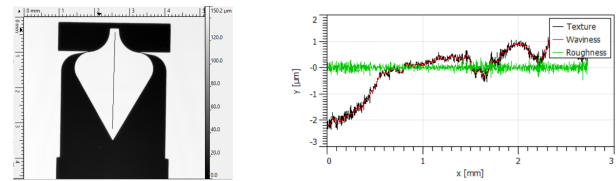


Fig. 14: Left: Measurement line on top surface; Right: Texture, waviness and Roughness measurement

The given graph elucidates the distinctions among texture, waviness, and roughness. Texture is a comprehensive descriptor of surface deviations and combines both the effects of waviness and roughness. As depicted in Figure

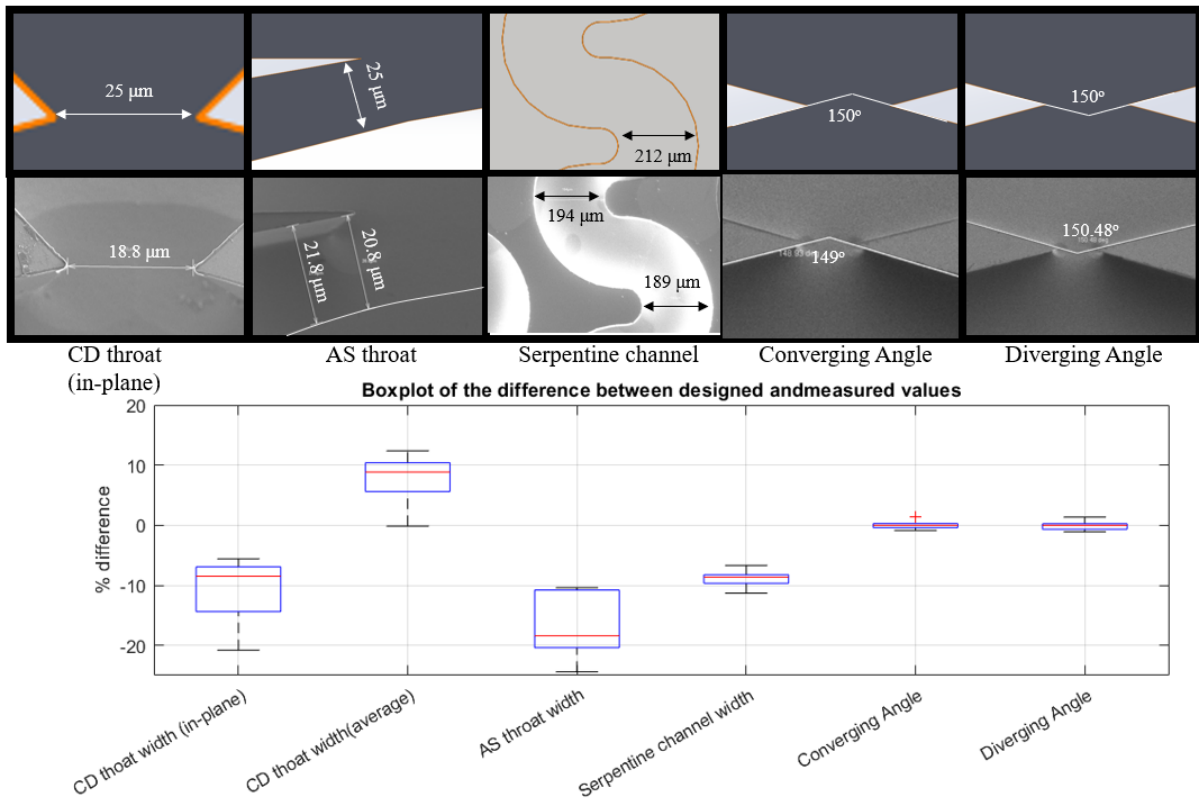


Fig. 13: Boxplot of various feature dimension differences form design (below); An illustration of each key feature design vs fabrication

Figure 14, where the texture is represented, it serves as a reflection of the overall surface variations. Waviness describes the more spaced-out and larger deviations from an ideal surface, often characterized by their longer wavelength. Factors influencing waviness can range from vibrations during the machining process to thermal effects and material warping. The waviness in Figure Figure 14 is depicted by the green line, emphasizing the broader variations across the measured distance. Roughness focuses on the closely spaced, finer surface deviations. This characteristic commonly stems from the inherent processes of material removal during manufacturing or is a result of specific material properties. In Figure Figure 14, the roughness is represented by the red line, underscoring the finer, high-frequency variations. In summary, while texture provides an overall perspective on surface deviations, waviness and roughness offer insights into broader and finer variations, respectively.

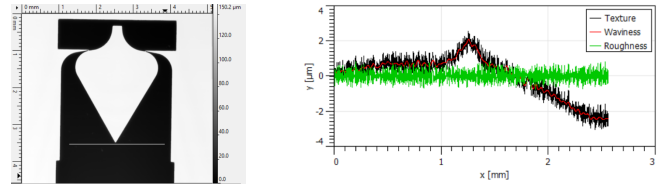


Fig. 15: Left: Measurement line in etched area; Right: Texture, waviness and Roughness measurement

The process was repeated for the etched layer of silicon. Table IV shows the values and distribution of the roughness across the wafer. Figure 15 shows the line across a sample where the measurement is taken and the

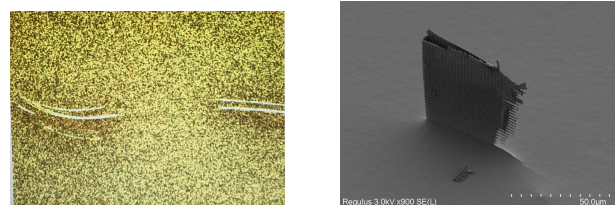


Fig. 16: Some minor defects in the Silica due to particles and handling

	Sample 1	Sample 2	Sample 3	Sample 4	Sample 5
Wafer 1	302nm	278nm	303nm	312nm	296nm
Wafer 2	28nm	306nm	303nm	297nm	294nm
Wafer 3	299nm	286nm	288nm	301nm	291nm

TABLE IV: Root mean square surface roughness - Bottom layer of thruster (Si)

4) *Presence of Defects*: In this section some minor defects noted are visualized. Each of the wafers had some handling and particulate defects, however, these were usually

not interfering with the thrusters and in inconsequential parts of the wafer. Some scratches and inconsistencies are showcased in Figure 16.

IV. ELECTRICAL CHARACTERIZATION

A. Methodology

In order to test if the resistance levels achieved are close to those designed the Manual Probe Station by Wentworth labs was utilized, the schematic for which is represented in Figure 17. It is possible to connect the bonding pads to a probe and measure individual resistances as shown in Figure 18. The sampling strategy is the same as in the previous section.

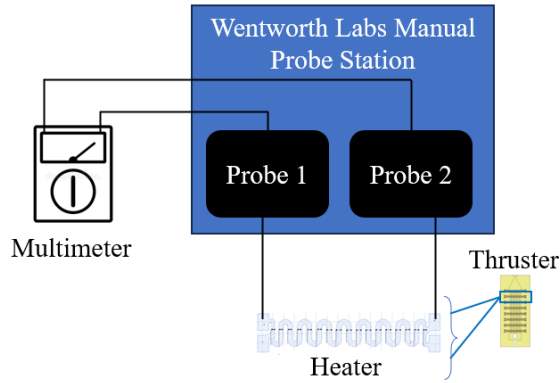


Fig. 17: Schematic working of a Probe station

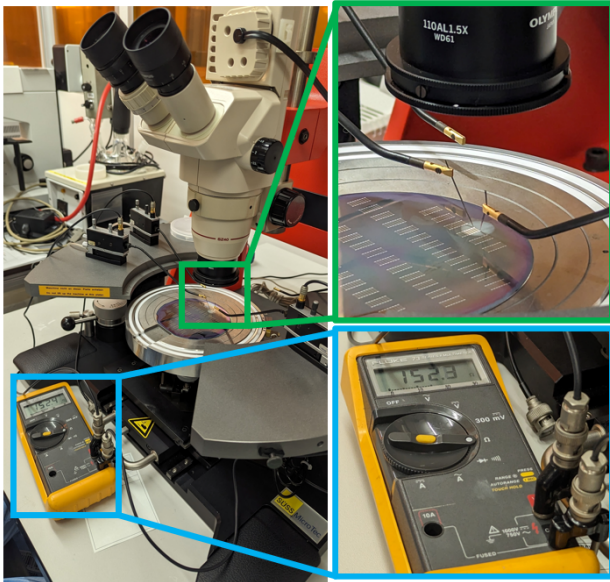


Fig. 18: Electrical characterization methodology

B. Results

The nominal resistance at room temperature was calculated as 102.5 mΩ. This is based on the minimal cross-section area where the width is 77 μm, the thickness was nominally supposed to be 500 μm. The measured results

are noted in Table V. The average measurement was 31.8% higher than the nominal value.

	Sample 1	Sample 2	Sample 3	Sample 4	Sample 5
Wafer 1	138.9mΩ	142.0mΩ	138.2mΩ	141.4mΩ	152.3mΩ
Wafer 2	132.3mΩ	136.0mΩ	131.2mΩ	129.4mΩ	134.4mΩ
Wafer 3	139.9mΩ	128.2mΩ	131.7mΩ	131.4mΩ	120.6mΩ

TABLE V: Resistance Measurement - Individual Resistors

V. DISCUSSION

Surface Morphology and Grain Structure: Microscopic evaluations affirm the inherent smoothness of the Silicon substrate and the oxide layer. A closer inspection of the sputtered titanium layer reveals non-uniform deposition, suggesting potential avenues for enhancing the metalization process. Nonetheless, the uniformity of the titanium layer is anticipated to support stable thermal distributions. Further evaluations are necessary to gauge the longevity of the titanium layer under repetitive heating. The subsequent aluminium layer displays instances of unevenness, occasionally exposing the titanium and silicon oxide layers beneath. This non-uniformity, potentially arising from inherent grain structures during deposition, is not expected to substantially compromise its role, especially in wire bonding processes.

Feature Dimensions (In-Plane and Depth): The in-plane dimensions of the thruster's surface exhibit a high level of precision, with a standard deviation of only 0.8 μm. Significantly, the nozzle throat corners have remained sharp, with any observed rounding capped at a mere 0.3μm, which can be attributed to using a hard-mask for the final etch.

Depth evaluations indicate a slight inclination in the Silicon etching for the thruster channel, which is more visible at the nozzle throat. The throat widths at the nozzles' bases are broader on average by 14 μm compared to their tops. As the mask images were designed to neutralized any throat widening effect (by being 5μm narrower than the true design target), the resultant fabricated throats are only 3.5 μm wider on average (across the entire width) than the intended designs. Such variations may however lead to very slight deviations from the simulation predictions and must be noted.

For broader etched regions, like the nozzle inlet, a variation in depth is observed. The central part of such channels exhibits slightly less etching than their edges. This can be attributed to the inherent characteristics of the DRIE process, where etching near the corners is marginally more efficient. This phenomenon accounts for the curved nature of these readings.

Surface Roughness: The surface roughness less than 500 nm is considered acceptable from a flow perspective and less than 100 nm is suitable for bonding, both of which were achieved. The bonding process should be quite robust. The flow separation should also be quite satisfactory as the etched surface is quite smooth, the only effect, if any, that must be noted is that of the scallops on the side walls.

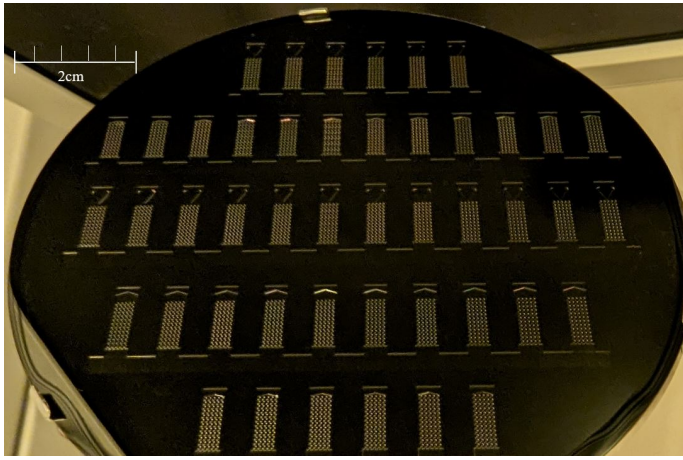


Fig. 19: Final fabricated wafer (W8)

A. Comparison to previously fabricated thrusters

In this section a quantitative comparison is drawn against the VLM thrusters previously fabricated by Silva et al. [1]. A summary is provided in Table VI.

Fabrication Efficiency: The revamped thruster design omits the need for processing a hole through the silicon substrate, culminating in a 18% reduction in the number of processing steps (and hence processing time as well). Transitioning from molybdenum to titanium introduced an additional step for aluminum pad wire bonding. However, the overarching process steps were reduced (by a further 3%), as titanium's superior adhesion negates the need for an adhesive layer and since the titanium deposition and etching processes are more straightforward compared to molybdenum.

Characterization Insights: A pivotal aspect of characterization is the nozzle throat width. In previous fabrications, designs achieved widths that were a mere 50%-60% of the desired size, accompanied by an inter-thruster variance of $\pm 3.5 \mu\text{m}$ on the same wafer [1]. The current fabrication methodology yielded an average throat width dimension spanning 104%-114% of the design value, with a lower deviation between thrusters on the same wafer of $\pm 0.5 \mu\text{m}$. An added advantage is the near-elimination of the rounding at the throat's sharp corners, a major improvement in efficiency. Surface roughness remains on par with prior iterations. Lastly, each wafer now accommodates 46 thrusters, up from 42, due to the optimized spatial allocation and the modular design methodology.

VI. CONCLUSION

This research presented a detailed examination and characterization of an advanced MEMS fabrication technique tailored for Vaporizing Liquid Micro-resistojet Microthrusters. By aligning the design considerations with MEMS fabrication nuances, a thruster design that allowed for a more streamlined and efficient manufacturing process was achieved. Following the design phase, the fabrication

was undertaken with an emphasis on process simplification, but without a trade-off in precision. Rigorous mechanical and electrical evaluations post-fabrication underscored the fidelity and reliability of the proposed methodology. Results conclusively indicated that the refined fabrication approach not only upheld standards associated with previous methods but also offered significant improvements in process efficiency. Collectively, this study signifies the successful integration of intricate MEMS design principles with an enhanced fabrication protocol, establishing a robust precedent for subsequent advancements in microthruster technology.

A. Further improvement possibilities

One promising avenue for further improvement in microthruster design involves integrating the entire system onto a single MEMS chip. This integration offers several significant advantages. It simplifies the fabrication process, making it more efficient, and ensures seamless interaction between system components, thereby optimizing overall performance. Additionally, this approach results in a more compact system, which is especially valuable for CubeSats and small satellite platforms. Moreover, the reduced number of interconnections in integrated designs enhances reliability by minimizing potential points of failure. Lastly, the singular MEMS process can lead to cost-effectiveness through reduced production costs.

- **Integrated Inlet Design:** By integrating the inlet design directly into the MEMS chip, it is possible to achieve a more consistent flow of propellant to the thruster. This would ensure optimal combustion and thrust efficiency, while also minimizing the footprint of the overall system.

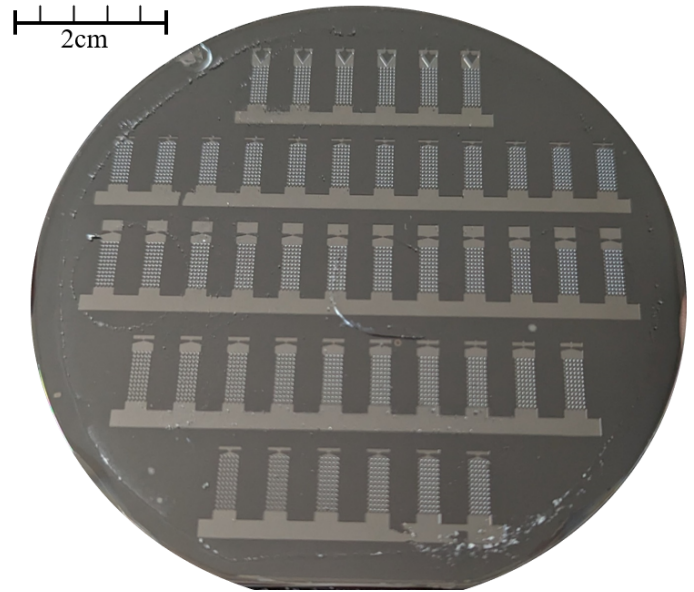


Fig. 20: Final Pilot Wafer post Glass wafer Bonding (W06)

Feature	Results		Previously Fabricated [1]	
	Design	Measured	Design	Measured
In-Plane Throat Width	25 μm	20.46 \pm 1 μm	45 μm	25.1 \pm 3.5 μm
	50 μm	46.4 \pm 1.2 μm	45 μm	26 \pm 2.8 μm
	75 μm	69.8 \pm 1.4 μm	45 μm	20 \pm 3.2 μm
Average Throat Width	25 μm	26.7 \pm 1.4 μm	NA	Not Measured
	50 μm	53.4 \pm 1.8 μm		
	75 μm	78.8 \pm 1.6 μm		
Width Inlet Channel	3000 μm	2985 \pm 4.2 μm	3000 μm	2983.3 \pm 10.2 μm
Converging Angle	Multiple	\pm 0.8 ^o	NA	Not Measured
Diverging Angle	Multiple	\pm 1 ^o	NA	Not Measured
Width Outlet	NA	Not Measured	500 μm	492.6 \pm 4.5 μm
			780 μm	777.7 \pm 1.5 μm
Resistance	102.5 $\mu\Omega$	134.6 \pm 11.2 $\mu\Omega$	3.4 Ω	8.8 Ω
			2.38 Ω	6.2 Ω

TABLE VI: Final Results of Characterization and Comparison with Previous Fabrication

- **Micro Valve Integration:** Integrating a micro valve on the same MEMS substrate would provide precise control over the propellant's flow rate. This allows for real-time thrust modulation, essential for intricate maneuvers in space missions.
- **On-chip Sensors:** Embedding temperature, pressure, and flow sensors directly into the MEMS chip provides several advantages:
 - **Real-time Monitoring:** The thruster's operation can be monitored in real-time, allowing for immediate adjustments to optimize performance.
 - **Safety:** In scenarios where anomalies are detected, such as an unexpected rise in temperature or pressure, the system can be automatically shut down or adjusted to prevent damage.
 - **Feedback Loops:** With integrated sensors, the system can be designed to have feedback loops, where the sensors' data is used to continuously adjust the thruster's operation for optimal performance.

- 8 Fredrickson, C. K. and Fan, Z. H., "Macro-to-micro interfaces for microfluidic devices," *Lab on a Chip*, vol. 4, no. 6, p. 526, 2004. [Online]. Available: <http://xlink.rsc.org/?DOI=b410720a>
- 9 Spermovasilis, G., "Design and fabrication of smart vaporizing liquid microthruster for Cubesat applications."
- 10 "Wet etching of silicon dioxide." [Online]. Available: http://www.microtechweb.com/kb/sio_etch.htm

REFERENCES

- 1 de Athayde Costa e Silva, M., "Mems micropropulsion: Design, modeling and control of vaporizing liquid microthrusters," Ph.D. dissertation, Delft University of Technology, Delft, Netherlands, 12 2018, promotor: Gill, E.K.A. and Cervone, A. [Online]. Available: <https://doi.org/10.4233/uuid:57f725e1-b3f3-455c-83ce-9156b2123c88>
- 2 Karthikeyan, K., Chou, S., Khoong, I. e., Tan, Y., Lu, C.-W., and Yang, W., "Low temperature co-fired ceramic vaporizing liquid microthruster for microspacecraft applications," *Applied Energy*, vol. 97, p. 577–583, 09 2012.
- 3 Cheah, K. H. and Low, K.-S., "Fabrication and performance evaluation of a high temperature co-fired ceramic vaporizing liquid microthruster," <https://iopscience.iop.org/article/10.1088/0960-1317/25/1/015013>, vol. 25, no. 1, p. 015013, Jan. 2015.
- 4 Silva, M. A., "MEMS micropropulsion."
- 5 Liu, B., Yang, X., Wang, Y., Li, D., Gao, G., Yang, J., and Zhou, R., "A tubular vaporizing liquid micro-thruster with induction heating," vol. 56, no. 7, pp. 2035–2043. [Online]. Available: <http://link.springer.com/10.1007/s00231-020-02836-7>
- 6 Kwan, P., Huang, X., and Zhang, X., "Design and testing of a microelectromechanical-system-based high heat flux vaporizing liquid microthruster," *Acta Astronautica*, vol. 170, 05 2020.
- 7 Fontanarosa, D., De Pascali, C., De Giorgi, M. G., Siciliano, P., Ficarella, A., and Francioso, L., "Fabrication and embedded sensors characterization of a micromachined water-propellant vaporizing liquid microthruster," <https://linkinghub.elsevier.com/retrieve/pii/S1359431121000818>, vol. 188, p. 116625, Apr. 2021.

5 | Low-Pressure Microthruster Design and Fabrication Process

“Redundancy is ambiguous because it seems like a waste if nothing unusual happens. Except that something unusual happens-usually.”

– Nassim Nicholas Taleb, *1960-Present*

5.1 Introduction to Low-Pressure Micro-resistojet Thrusters

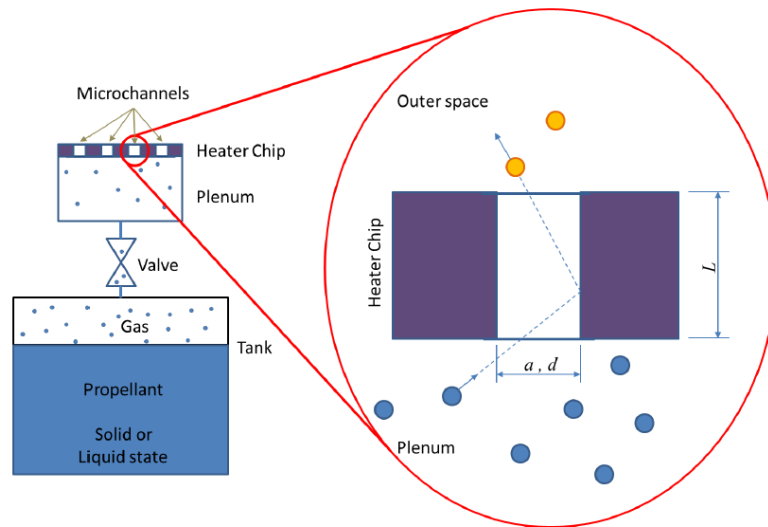


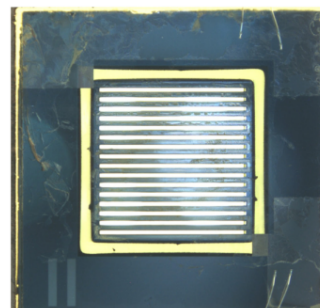
Figure 5.1: Schematic of the LPM. Left: the complete system - tank, feed system and thruster. Right: The detailed microchannel and the particle behavior

Low-pressure micro-resistojet is also known as Free Molecule Micro Resistojet (FMMR). This type of thruster works in the transitional flow regime due to the low pressure. Statistical methods (based on the gas kinetic theory) are used to model the behavior of this microthruster [14]. The devices consist of an inlet section, a plenum where the propellant enters at very low pressure, and a resistance heater chip with slots or microchannels through which the gas is accelerated to space. These components are illustrated in Figure 5.1 [15].

These devices are usually simulated or tested with inert gases or water [16]. An interesting advantage of this type of micropropulsion system is the scalability of the design. The number of channels in the heater chip can be increased or decreased as required. Each channel provides a certain amount of thrust so that the total thrust can be adjusted in the design for the particular mission by choosing the correct number of channels.



((a)) Coupled Heater LPM, 2005



((b)) silicon dioxide insulation LPM, 2013

Figure 5.2: LPM MEMS Chips

Ketsdever et al.[17] proposed the first design of the thruster in 1998. The molecules were heated before reaching the expansion slots from which they were expelled, generating thrust. In 2005 [18] the heater was coupled with the expansion slots chip (formulating a heater chip shown in Figure 5.2(a) allowing the molecules to heat up inside the slots and then be expelled. The heater chip was manufactured using MEMS technology (gold layers on Silica wafer). In 2013, Palmer et al.[19] improved the efficiency by fabricating and testing a design with silicon dioxide insulation and suspension to reduce the heat losses, shown in Figure 5.2(b)

In 2018 three different LPM devices with integrated heaters and temperature measurements were designed, manufactured, and characterized by Cordeiro Guerrieri in the Department of Space Engineering at Delft University of Technology[15]. The design with large slots is shown in Figure 5.3. This design is the basis for this report and the proposed study.

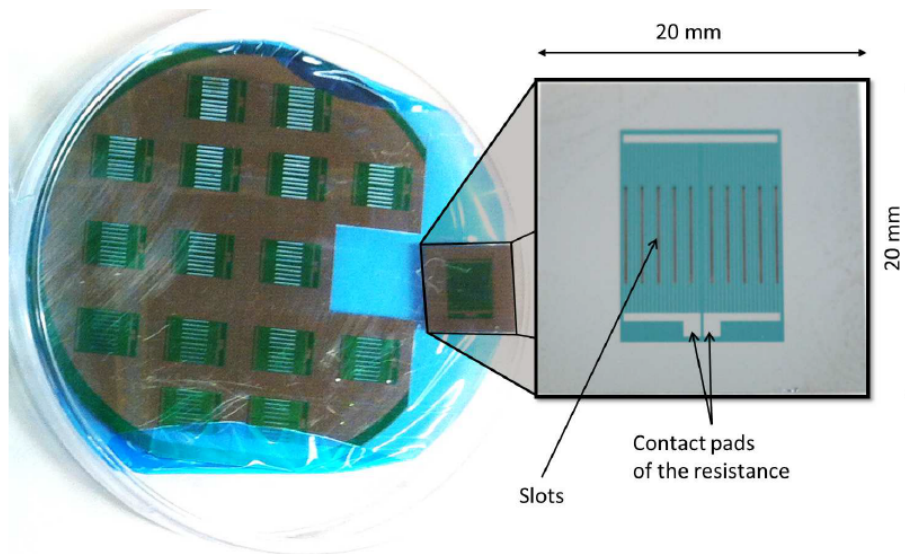


Figure 5.3: LPM Wafer with large slots chips after manufacturing and dicing process, 2018

5.2 Literature Prerequisites for Design of LPM thruster

In the molecular theory (used for the analysis of fluids in the rarefied flow regime) some assumptions are crucial for modeling gases and their interactions, but may break down under conditions of high pressure, low temperature, or strong potential fields. These assumptions are as follows:

1. Classical mechanics govern the motion of atoms and molecules.
2. A macroscopic volume contains a sufficiently large number of particles, on the order of 10^{19} molecules per cm^3 , to produce a time-independent pressure.
3. Molecular separations greatly exceed the molecular size and the range of intermolecular forces, allowing treatment as an ideal gas dominated by molecular kinetic energy. Collisions are negligible for describing equilibrium properties.
4. Molecules are usually uniformly distributed within the container, except in cases of strong external potential fields.

5. Molecule velocity directions are uniformly distributed, consistent with the hypothesis of molecular chaos.

The **Number Density** (n) is defined as the concentration of molecules in a volume:

$$n = \frac{N}{V} \quad (5.1)$$

where V is the volume of the container and N is the total number of molecules.

Molecular flux (ϕ) is defined as the number of molecules dN crossing a unit surface in one direction during a unit of time. For instance, molecular flux determines the rate of molecules striking the wall or exiting the container through a small orifice in the wall (effusion). The expression for the flux reads:

$$\Phi = \frac{dN}{dSdt} \quad (5.2)$$

where dS is the elementary surface, dN is the number of molecules within an elementary volume.

The molecular flux is proportional to the **mean molecular velocity** \bar{v} while the pressure on the walls is proportional to \bar{v}^2 . In fact, the mean velocity can be derived as:

$$\bar{v} \approx \frac{\Phi}{n} \quad (5.3)$$

The thrust can be measured by calculating the surface integral across the exit area using Equation 3.7 :

$$\mathbf{F} = - \iint_{A_e} \mathbf{V}(\rho \mathbf{V} \cdot \mathbf{n}) dA_e - \iint_{A_e} ((p - p_\infty) \mathbf{n}) dA_e + \iint_{A_e} (\boldsymbol{\tau} \cdot \mathbf{n}) dA_e \quad (5.4)$$

The given equation represents a force balance in fluid mechanics. Overall, the resultant F is the net force on the fluid within the control volume due to these effects. This equation is a manifestation of the momentum conservation principle applied to a control volume in fluid dynamics. The equation can be understood as follows:

- The first term, $\int \int_{A_e} V(\rho V \cdot n) dA_e$, represents the momentum flux due to the convective transport through the control surface. In this term, V is the velocity vector, ρ is the fluid density, and n is the unit normal vector pointing out of the control surface.
- The second term, $\int \int_{A_e} ((p - p_\infty) n) dA_e$, captures the force due to the pressure difference between the fluid pressure p and some reference pressure p_∞ acting over the control surface. In the context of the rarefied flow simulation the pressure difference between the fluid pressure $p \approx p_\infty$, hence this term tends to 0.
- The third term, $\int \int_{A_e} (\boldsymbol{\tau} \cdot n) dA_e$, represents the shear stress acting on the control surface, where $\boldsymbol{\tau}$ is the shear stress tensor. this term also tends to 0 in the context of this chapter as $\boldsymbol{\tau} \approx 0$.

5.3 Design of LPM thruster

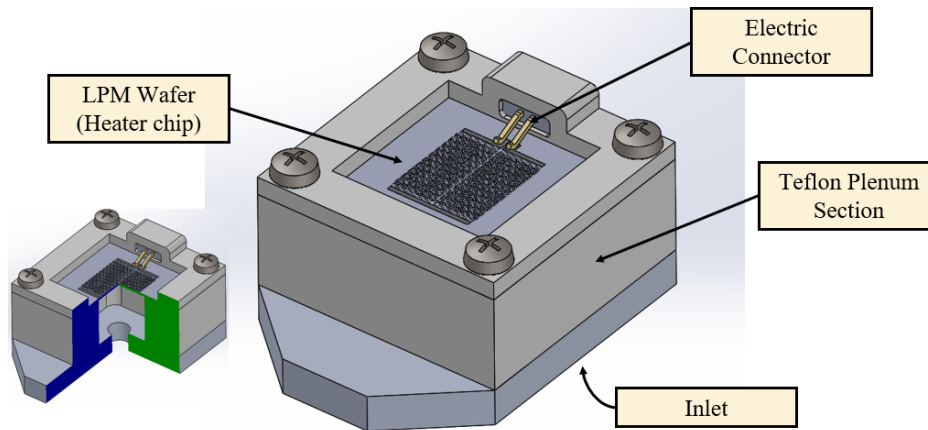


Figure 5.4: CAD model of simple LPM thruster assembly

The aim of this section is to design a Low-Pressure Microthruster (LPM) while maximizing the thrust per unit size. In order to do so, a previous, successfully tested thruster assembly created by Guerrieri et al. [15], shown in Figure 5.4, was selected. Keeping the same design, small modifications like editing the length of the plenum are tested in order to minimize the size by optimizing the fabrication and assembly process while not reducing the thrust producing characteristics.

5.4 LPM thruster - CFD modeling and analysis

Computational Fluid Dynamics (CFD) simulations were used for the analysis of fluid flow and heat transfer within the microthruster. The analysis is carried out in the rarified flow regime that is typical for these kinds of devices. The software platform employed for this purpose is COMSOL.

The meshing approach involves the use of tetrahedral elements. Near the walls, a finer mesh is applied to accurately capture boundary layer effects as well as the specifics of rarified flow behavior.

For boundary conditions, the outlet pressure is set to replicate vacuum conditions, along with theoretical wall temperatures achievable by the MEMS heater (300K to 900K). The fluid inlet is varied from 25 SCCM to 400 SCCM. For context, 100 SCCM implies an input flow rate of 7.43×10^{-7} moles/s. For water (Molecular mass 18) as a propellant each mole weighs about 18.0152 kg. Hence the input mass flow rate is approximately 1.34×10^{-6} kg/s. These conditions are particularly important for modeling the rarified flow conditions that the thruster would experience in actual use, ensuring the model's relevance and applicability.

For the computational simulations of the LPM thruster, the input is given in terms of mass flow rate (SCCM). Yet, for a coherent analysis, it's vital to establish the relationship between

the mass flow rate, \dot{m} , and the plenum pressure, P_0 . This relationship is denoted by:

$$P_0 = \frac{\dot{m}}{\alpha \sqrt{\frac{m_a}{2\pi k T_0}} A_e} \quad (5.5)$$

Where α is the velocity correction factor, m_a signifies the average molecular mass, k is the Boltzmann Constant, T_0 is the wall temperature and A_e denotes the total exit area of the nozzle. The relation in the low pressure region is shown in [Figure 5.5](#).

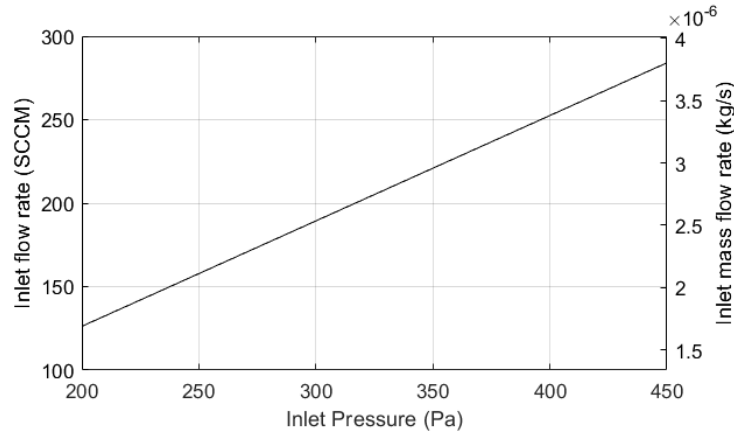


Figure 5.5: SCCM or mass flow rate vs Plenum Pressure

With this mathematical relationship established, rarified flow simulations of the LPM thruster are executed to determine thrust values versus various input pressures (converted from SCCM).

In the experimental realm, measurements were performed in a chamber that cannot achieve a true vacuum. As a result, the gathered experimental data had to be extrapolated to predict the behavior at an exit pressure of 0 Pa, resembling true vacuum conditions.

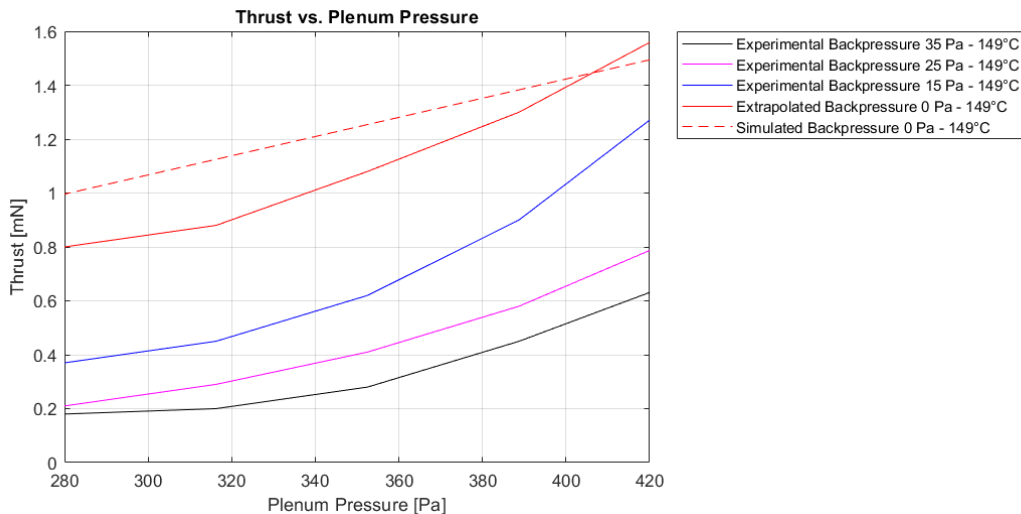


Figure 5.6: Experimental thrust ([Appendix D](#)) vs Simulated Thrust of current LPM design

After this extrapolation, a comparative analysis was initiated. The thrust values derived from the simulations are juxtaposed against the extrapolated experimental data and are shown in [Figure 5.6](#). This step ensures the validation of the computational model's accuracy and reliability in order to be used for further design optimization.

Next, a comprehensive simulation was conducted to evaluate the influence of varying plenum heights on thruster performance. The objective was to discern if alterations in the plenum dimensions would yield significant variations in the propulsion output. The results demonstrated that the reduction in thrust due to diminished plenum height was marginal and within acceptable tolerances (see [Table 5.1](#)). Consequently, it can be inferred that the design of a thruster with a reduced plenum volume will not compromise its operational efficacy.

Temp (K)	Input (SCCM)	Plenum Height 14mm		Plenum Height 5mm	
		Thrust (N)	Av. molecular flux (1/(m ² s))	Thrust (N)	Av. molecular flux (1/(m ² s))
300	50	2.46E-04	9.88E+22	2.45E-04	9.86E+22
300	100	4.91E-04	1.98E+23	4.90E-04	1.97E+23
300	150	7.37E-04	2.96E+23	7.36E-04	2.96E+23
600	50	3.47E-04	9.88E+22	3.47E-04	9.86E+22
600	100	6.95E-04	1.98E+23	6.93E-04	1.97E+23
600	150	0.0010419	2.96E+23	0.0010402	2.96E+23
900	50	4.25E-04	9.88E+22	4.25E-04	9.86E+22
900	100	8.51E-04	1.98E+23	8.49E-04	1.97E+23
900	150	0.0012761	2.96E+23	0.001274	2.96E+23

Table 5.1: Effect of reducing Plenum height

In summary, the simulation outcomes are comparable to the thrust values gathered from prior experiments. The results indicate a deviation of less than 18% from the experimental data, which is deemed acceptable for the project scope. This corroborates the credibility of the CFD model as a highly effective simulation tool, especially for studying microthrusters in rarified flow conditions. The validated model thus provides a foundation for expediting future design modifications in a cost-effective manner. Secondly, a modified, more compact assembly design is validated and can now be theorized.

5.5 Wafer Fabrication Process

The fabrication process is initiated with the creation of photolithography masks. Detailed designs of the hearers and slots are transferred as images on the mask. These masks play a pivotal role, acting as precise templates to pattern the silicon wafer. The chosen wafer is characterized by a double-side polish and a thickness of 500 μm . The silicon wafer is subjected to an extensive cleaning procedure to remove any contaminants. To achieve high-precision alignment of the layers that follow, lithographic alignment marks, commonly referred to as the zero layer, are etched onto the wafer surface. A graphical representation of the fabrication sequence sequence is provided in [Figure 5.7](#).

(a) A layer of 500 nm PECVD (Plasma-enhanced Chemical Vapour Deposition) silicon nitride is deposited, establishing an insulation barrier between the wafer and the resistance.

(b) A 500 nm layer of Titanium is deposited over the silicon nitride layer through the process of sputtering.

(c) An additional sputtering process is used to deposit a 200 nm layer of Aluminium over the Titanium layer.

(d) The surface is then treated with a spin-coated photoresist. The contact pads are subsequently exposed and developed, after which a wet etching process removes the Aluminium, leaving behind only the intended bonding pads.

(e) The heater mask is formed through a similar photoresist layer, paving the way for Titanium etching that results in the specified heater designs.

(f) For comprehensive wafer etching, one side is equipped with a hard-mask layer and the opposite with a stopping layer. Both sides are coated with a thick layer of TEOS oxide using PECVD (In the order of $5 \mu\text{m}$).

(g) A photoresist layer forms the soft-mask to etch the oxide layer hard mask. Individual mask designs, whether holes or slots, are exposed, facilitating the etching of the hard-mask oxide layer by reactive ion etching (RIE).

(h) Utilizing the hard-mask as a guide, the silicon is etched all the way through ($500 \mu\text{m}$) via anisotropic Deep Reactive Ion Etching (DRIE).

(i) Lastly, both the hard-mask and stopping layers are completely removed using Silicon oxide wet-etching.

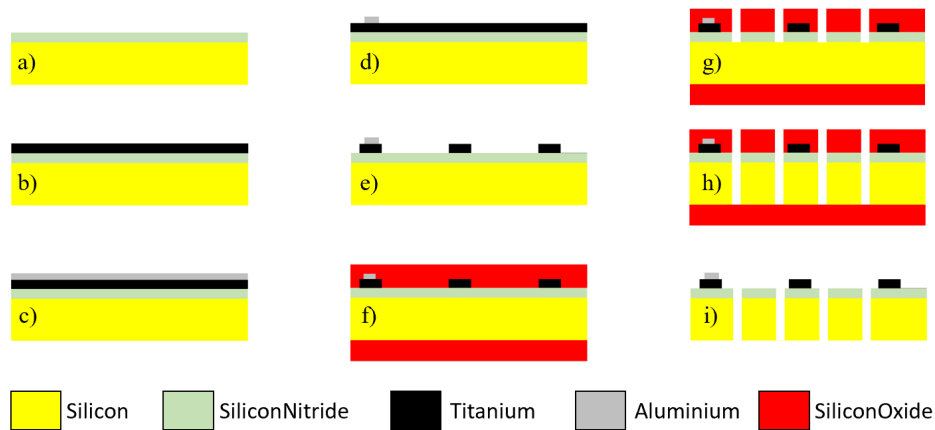


Figure 5.7: Section plane showcasing MEMS fabrication sequence for LPM thruster

Following the fabrication steps, the wafer is diced, producing 16 individual heater chips. The culmination of the fabrication process is the assembly stage, where discrete components like the LPM Chip, plenum chamber, and propellant feed system are carefully aligned and bonded, forming a cohesive thruster unit. In this new design, bonding is used instead of fastening to allow for further compactness of the design (also allowing for reduction in X and Y dimensions of assembly).

5.6 Final Design and Discussion - LPM

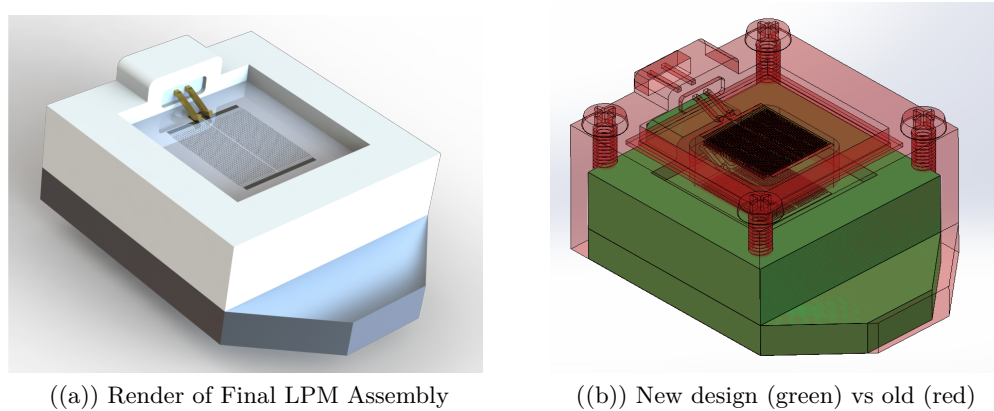


Figure 5.8: Final LPM Design

The final design is showcased in [Figure 5.8](#) and a simulation showing the molecular flux across the holes at an input of 150 SCCM and a wall temperature of 150°C is shown in [Figure 5.9](#).

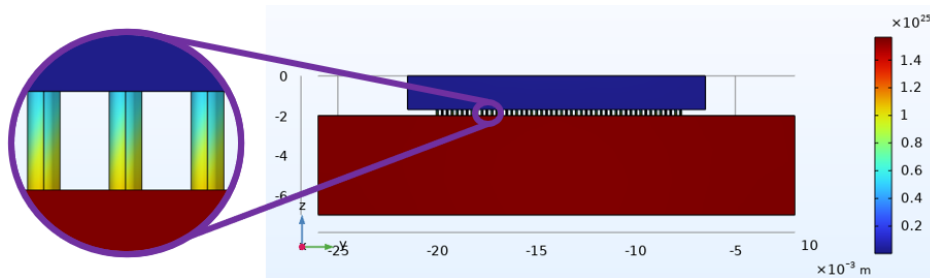


Figure 5.9: Molecular flux across the LPM holes

In summation the following targets were achieved:

- A 31% reduction in Volumetric space occupied ([Figure 5.8](#)) by the thruster with only a 0.4% reduction in calculated thrust.
- An accurate numerical model, that is parametrical created such that it can easily be used for further improvement of the thruster design.
- The new fabrication process reduces the number of steps by 4% and uses simpler metal deposition processes.

Upon fabrication of the thrusters, they must undergo a series of tests to characterize both their mechanical and electrical properties. Such tests should offer critical insights into any modifications required in the fabrication process. Thrust tests must be conducted within a vacuum chamber to emulate space-like conditions. These tests should determine the actual thrust output from the microthrusters and either validate or challenge the predictions made by the CFD model. Additionally, a flow control mechanism must be developed and integrated into the thruster system.

6 | Conclusions & Recommendations

“It will be said that the conclusion no doubt preceded its ‘proofs’. But what man can content himself with seeking out proofs for a thing that not even he himself believes in, or whose teaching he cares naught for?”

– Jorge Luis Borges, 1899-1986

6.1 Conclusions

In the journey of advancing micro-resistojet thrusters, this report has meticulously outlined a comprehensive framework. Chapter 3 introduced the design principles behind the Vaporizing Liquid Microresistojet (VLM) thruster, establishing the foundational parameters and considerations. This design phase played a pivotal role in the subsequent fabrication process detailed in Chapter 4. The unique inlet features of the VLM design streamlined the fabrication process, permitting a reduction in the number of process steps, thereby expediting the overall manufacturing timeline.

Chapter 5 introduced the Low Pressure Microresistojet (LPM) thruster and its design and fabrication intricacies. The LPM, while being a distinct entity, complements the VLM in functionality. Together, the VLM and LPM thrusters offer redundancy to the propulsion system, ensuring that even if one thruster encounters challenges, the other can seamlessly take over, thus enhancing the system's robustness and reliability.

In conclusion, these chapters cohesively advance the discourse on micro-resistojet thrusters. The innovative designs of VLM and LPM not only extend the horizons of thruster technology but also mark significant strides toward its commercial viability. The models formulated provide a direct path for further refinements, while the achievements in experimental fabrication underscore the tangible progress toward the commercialization of these propulsion systems. Collectively, this body of work significantly furthers the technical readiness and broader scope of micro-resistojet thrusters in the aerospace domain.

6.2 Evaluating Research Objectives

In order to better understand and evaluate if the thesis is a complete well rounded scientific work, we will go back to the original research question (and sub-questions):

SQ1: *What quantifiable effects do flow dynamics optimization have on the performance-to-size ratio of existing MEMS Micro-resistojet thrusters?*

Considering the VLM thrusters, a validated CFD model, corroborated by previous experimental data, was constructed. This model functioned as an evaluative tool for assessing the flow performance of both the thruster inlet and nozzle. This evaluation determined the optimal shapes and dimensions to maximize thrust for specific input power and inlet mass flow rates. As a result of this modeling, the performance-to-size ratio was notably enhanced: thrust output escalated by 18% without any alteration to the existing overall dimensions of the VLM thruster. Moreover, the modification of the inlet design bolstered the uniformity of flow distribution across the inlet by a substantial 40% while also improving the start-up conditions due to a more uniform flow delivery in comparative time-dependent simulations.

Turning to the LPM thruster, a simulation was established in the rarefied (free molecular) flow regime. This simulation too was authenticated by comparing its results to previous experimental findings. It was then used to refine the geometry of the thruster. The objective was to reduce its size while mitigating thrust loss. Through iterative design and simulation, a balanced design was achieved, culminating in a thruster that was 31% more compact (reduction in volume), with a relatively inconsequential 0.4% reduction in thrust performance under consistent input and ambient conditions.

SQ2: *What fabrication techniques can be employed to improve time-efficiency and design fidelity in MEMS Micro-resistojet thrusters?*

In light of the insights gleaned from the numerical models, certain MEMS fabrication techniques were appraised based on the duration of individual steps, the total number of steps involved, and the design fidelity attained. The adopted process for both, the VLM and the LPM is explained within the report, with a comprehensive fabrication flowchart provided in the Appendix. Marked improvements in fabrication time-efficiency emerged. The fabrication sequence for the updated VLM design was curtailed by 18% while retaining design precision, as elucidated in SQ3. During the fabrication phase, defects were negligible, resulting in geometrically consistent thrusters. Such thrusters realized through this refined process, are primed for subsequent testing phases, nozzle type validation, and potential assembly optimization in the future. The LPM fabrication process too has a slight improvement in terms of a 4% reduction in the number of fabrication steps.

SQ3: *What is the degree of deviation between the manufactured MEMS Micro-resistojet thrusters and their initial design specifications?*

Upon conducting mechanical characterization of the produced VLM thrusters, disparities in geometry between the actual outcomes and design specifications were discerned. The thrusters exhibited an average in-plane discrepancy of $0.8 \mu\text{m}$ relative to the set dimensions, with the most pronounced deviation of $1.3 \mu\text{m}$ observed at the nozzle throat. The attained surface finish met satisfactory criteria; etched areas displayed a roughness of 300 nm while the surface intended for anodic bonding reflected a 90 nm roughness. On evaluating the surface morphology of the Titanium and Aluminium layers, it became evident that these layers were not entirely crystalline, potentially posing challenges under repetitive load conditions. However, the electrical characterization of the heater yielded results ranging between $132 \text{ m}\Omega$ and $154 \text{ m}\Omega$, aligning fairly closely with the design benchmark of $142 \text{ m}\Omega$ (exhibiting a variance of -7% to $+8.5\%$).

How can the optimization of flow dynamics, time-effective fabrication techniques, and design fidelity collectively enhance the performance and manufacturing accuracy of MEMS Micro-resistojet thrusters?

The answer to the overarching research question is a summary of the answers to the sub-questions:

Flow dynamics optimization in VLM and LPM thrusters leads to a refined performance-to-size ratio. By evaluating and updating MEMS fabrication techniques, manufacturing becomes more time-efficient and the fidelity of the design is preserved. Mechanical characterization shows that the produced thrusters closely adhere to the initial design specifications. In essence, through methodical flow dynamics optimization, the adoption of streamlined fabrication methods, and strict adherence to design specifications, the performance and manufacturing accuracy of MEMS Micro-resistojet thrusters are substantially enhanced.

6.3 Recommendations

Building upon the advancements achieved in this study, several avenues for future work present themselves, offering the potential for further optimization and integration of subsystem components. Some of these which are specific to one topic are highlighted at the end of each respective chapter. However, as an integrated system, many opportunities present themselves.

The first recommendation is to further investigate alternative materials for the thruster components to achieve higher thermal resistance and mechanical strength. Integrating the learnings of this study with advanced ceramic VLM designs tested by other studies. Eventually, composite materials could also be potential candidates.

While the current study optimized the nozzle shape for an 18% increase in thrust, more complex geometries such as multi-expansion nozzles could be explored to evaluate their impact on thrust efficiency and stability. Also, other methods to fabricate nozzles may allow for more versatile 3D designs.

The introduction of an integrated control system, possibly a closed-loop feedback mechanism, would allow for more precise control of thrust levels and angles, thereby improving navigation capabilities. This is a necessity for industrial acceptance of this technology.

The integration of MEMS sensors directly into the thruster assembly has already been theorized and prototypes. This could provide real-time monitoring capabilities, improving the adaptability and responsiveness of the propulsion system. Integrating these designs into a geometrically optimized thruster would be a possible continuation of these studies.

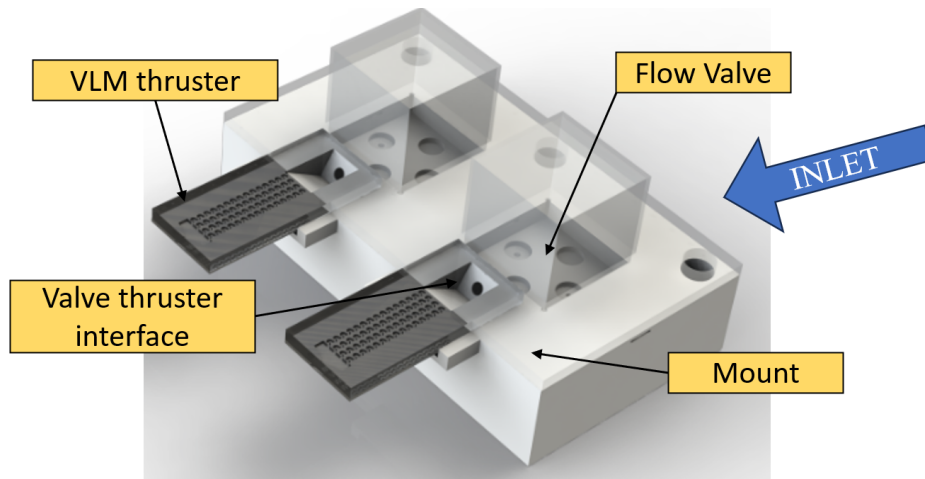


Figure 6.1: Render of possible integrated valve to inlet assembly

Another important component that is currently being researched independently is the micro-valve to control the inlet flow characteristics. A concept being developed in parallel with this study was theorized to make an integrated assembly between the VLM thruster inlet component and the valve outlet. The developed model is shown in Figure 6.1. Eventually, the target would be to integrate the valve as an electro-mechanical component of the thruster chip itself allowing for precise control, a smooth interface (with less failure points), and a

vast reduction in the assembly size. The accompanying CAD models provide a starting point for these future developments and offer a cohesive vision for a more advanced and integrated propulsion system. The realization of these recommendations will undoubtedly yield a more efficient, reliable, and versatile thruster.

Lastly, the next immediate step is the experimental validation to confirm the simulated performance gains of the fabricated thrusters. This includes testing the flow and thrust characteristics of the thrusters.

Bibliography

- [1] NASA. (n.d.). “Beginner’s Guide to Propulsion.” en. In: (), p. 1.
- [2] NASA. (n.d.). “Specific Impulse”. en. In: <https://www.grc.nasa.gov/WWW/K-12/airplane/specimp.html> (), p. 1.
- [3] R. Jahn and E. Choueiri. “Electric Propulsion”. In: *Encyclopedia of Physical Science and Technology*. 2003, pp. 125–141. DOI: [10.1016/B0-12-227410-5/00201-5](https://doi.org/10.1016/B0-12-227410-5/00201-5).
- [4] M. Ivanov et al. “Numerical study of cold gas micronozzle flows”. In: *37th Aerospace Sciences Meeting and Exhibit*. Reno,NV,U.S.A.: American Institute of Aeronautics and Astronautics, Jan. 1999. DOI: [10.2514/6.1999-166](https://doi.org/10.2514/6.1999-166).
- [5] Marsil A.C. Silva et al. “A review of MEMS micropropulsion technologies for CubeSats and PocketQubes”. en. In: *Acta Astronautica* 143 (Feb. 2018), pp. 234–243. ISSN: 00945765. DOI: [10.1016/j.actaastro.2017.11.049](https://doi.org/10.1016/j.actaastro.2017.11.049).
- [6] V Pallichadath et al. “Integration and Miniaturization Challenges in the Design of Micro-Propulsion Systems for Picosatellite Platforms”. en. In: (), p. 13.
- [7] K. Karthikeyan et al. “Low temperature co-fired ceramic vaporizing liquid microthruster for microspacecraft applications”. In: *Applied Energy* 97 (Sept. 2012), pp. 577–583. DOI: [10.1016/j.apenergy.2011.11.078](https://doi.org/10.1016/j.apenergy.2011.11.078).
- [8] Kean How Cheah and Kay-Soon Low. “Fabrication and performance evaluation of a high temperature co-fired ceramic vaporizing liquid microthruster”. en. In: *Journal of Micromechanics and Microengineering* 25.1 (Jan. 2015), p. 015013. ISSN: 0960-1317, 1361-6439. DOI: [10.1088/0960-1317/25/1/015013](https://doi.org/10.1088/0960-1317/25/1/015013).
- [9] Bendong Liu et al. “A tubular vaporizing liquid micro-thruster with induction heating”. In: *Heat and Mass Transfer* 56.7 (July 2020), pp. 2035–2043. ISSN: 0947-7411, 1432-1181. DOI: [10.1007/s00231-020-02836-7](https://doi.org/10.1007/s00231-020-02836-7). URL: <http://link.springer.com/10.1007/s00231-020-02836-7> (visited on 01/26/2023).
- [10] Pokwang Kwan, Xun Huang, and Xin Zhang. “Design and testing of a microelectromechanical-system-based high heat flux vaporizing liquid microthruster”. In: *Acta Astronautica* 170 (May 2020). DOI: [10.1016/j.actaastro.2020.01.017](https://doi.org/10.1016/j.actaastro.2020.01.017).
- [11] Donato Fontanarosa et al. “Fabrication and embedded sensors characterization of a micromachined water-propellant vaporizing liquid microthruster”. en. In: *Applied Thermal Engineering* 188 (Apr. 2021), p. 116625. ISSN: 13594311. DOI: [10.1016/j.applthermaleng.2021.116625](https://doi.org/10.1016/j.applthermaleng.2021.116625).
- [12] D C Guerrieri. “Optimum Design of Low-Pressure Micro-Resistojet Applied to Nano- and Pico- Satellites”. en. In: (), p. 10.

- [13] Loughborough University. *An Introduction to MEMS (Micro-electromechanical Systems)*. Additional details or a URL can be added here if available. Prime Faraday Technology Watch, 2002.
- [14] Zeeshan Ahmed, Sergery Gimelshein, and Andrew Ketsdever. “Numerical Analysis of Free Molecule Micro-Resistojet Performance”. In: *Journal of Propulsion and Power - J PROPULSION POWER* 22 (June 2005), p. 13. DOI: [10.2514/1.19570](https://doi.org/10.2514/1.19570).
- [15] D. Cordeiro Guerrieri. *The low-pressure micro-resistojet: Modelling and optimization for future nano- and pico-satellites*. en. OCLC: 8086875316. ISBN: 978-94-028-1157-5.
- [16] Ariel Blanco and Subrata Roy. “Numerical Simulation of a Free Molecular Electro Jet (FMEJ) for In-Space Propulsion”. In: Jan. 2013. ISBN: 978-1-62410-181-6. DOI: [10.2514/6.2013-208](https://doi.org/10.2514/6.2013-208).
- [17] Andrew Ketsdever et al. “A Free Molecule Micro-Resistojet: An Interesting Alternative to Nozzle Expansion”. In: (Jan. 1998), p. 8. DOI: [10.2514/6.1998-3918](https://doi.org/10.2514/6.1998-3918).
- [18] Andrew D Ketsdever, Riki H Lee, and Taylor C Lilly. “Performance testing of a micro-fabricated propulsion system for nanosatellite applications”. In: *Journal of Micromechanics and Microengineering* 15.12 (Dec. 1, 2005), pp. 2254–2263. ISSN: 0960-1317, 1361-6439. DOI: [10.1088/0960-1317/15/12/007](https://doi.org/10.1088/0960-1317/15/12/007). URL: <https://iopscience.iop.org/article/10.1088/0960-1317/15/12/007> (visited on 01/25/2023).
- [19] Kristoffer Palmer, Hugo Nguyen, and Greger Thornell. “Fabrication and Evaluation of a Free Molecule Micro-Resistojet with a Thick Silicon Dioxide Insulation and Suspension”. In: *Journal of Micromechanics and Microengineering* 23 (Apr. 2013). DOI: [10.1088/0960-1317/23/6/065006](https://doi.org/10.1088/0960-1317/23/6/065006).
- [20] George P Sutton and Oscar Biblarz. “Rocket Propulsion Elements”. In: ().
- [21] A.M. Si Mohammed et al. “Three-axis active control system for gravity gradient stabilised microsatellite”. In: *Acta Astronautica* 64.7 (Apr. 2009), pp. 796–809. ISSN: 00945765. DOI: [10.1016/j.actaastro.2008.12.010](https://doi.org/10.1016/j.actaastro.2008.12.010).
- [22] Teodor Bozhanov. “Analysis of Electric Propulsion Systems for Drag Compensation of Small Satellites in Low Earth Orbits”. In: <http://rgdoi.net/10.13140/RG.2.2.11090.15045> (2017). Publisher: Unpublished. DOI: [10.13140/RG.2.2.11090.15045](https://doi.org/10.13140/RG.2.2.11090.15045).
- [23] NASA earth observatory. “Achieving and Maintaining Orbit”. en. In: (2022).
- [24] NASA Goddard Space Flight Center. *James Webb Space Telescope FAQ*. en.
- [25] André Horstmann et al. “Survey of the Current Activities in the Field of Modeling the Space Debris Environment at TU Braunschweig”. In: *Aerospace* 5.2 (Apr. 2, 2018), p. 37. ISSN: 2226-4310. DOI: [10.3390/aerospace5020037](https://doi.org/10.3390/aerospace5020037).
- [26] Arthur Stinner and John Begoray. “Journey to Mars: the physics of travelling to the red planet”. In: *Physics Education* 40.1 (Jan. 1, 2005), pp. 35–45. ISSN: 0031-9120, 1361-6552. DOI: [10.1088/0031-9120/40/1/002](https://doi.org/10.1088/0031-9120/40/1/002).
- [27] Joseph N. Pelton and Scott Madry, eds. *Handbook of Small Satellites: Technology, Design, Manufacture, Applications, Economics and Regulation*. Cham: Springer International Publishing, 2020. ISBN: 978-3-030-36307-9 978-3-030-36308-6. DOI: [10.1007/978-3-030-36308-6](https://doi.org/10.1007/978-3-030-36308-6).
- [28] AMSAT. “AMSAT Live Oscar Satellite Status Page n.d.” en. In: <https://www.amsat.org/status/> ().
- [29] UTIAS-SFL. “Engineering The BRITE-Constellation satellites”. en. In: <https://brite-constellation.at/constellation/> ().

- [30] Bryce Space and Technology. *Smallsats by the numbers 2022*. en. 2022.
- [31] FAA. *The Annual Compendium of Commercial Space Transportation: 2018*. en. 2018.
- [32] Donato Fontanarosa et al. “MEMS Vaporizing Liquid Microthruster: A Comprehensive Review”. en. In: *Applied Sciences* 11.19 (Sept. 2021), p. 8954. ISSN: 2076-3417. DOI: [10.3390/app11198954](https://doi.org/10.3390/app11198954).
- [33] Jürgen Müller et al. “Design, analysis and fabrication of a vaporizing liquid micro-thruster”. In: July 1997. DOI: [10.2514/6.1997-3054](https://doi.org/10.2514/6.1997-3054).
- [34] E. V. Mukerjee et al. “Vaporizing liquid microthruster”. In: *Sensors and Actuators A: Physical* 83.1 (2000), pp. 231–236. ISSN: 0924-4247. DOI: [https://doi.org/10.1016/S0924-4247\(99\)00389-1](https://doi.org/10.1016/S0924-4247(99)00389-1). URL: <https://www.sciencedirect.com/science/article/pii/S0924424799003891>.
- [35] D K Maurya, S Das, and S K Lahiri. “Silicon MEMS vaporizing liquid microthruster with internal microheater”. In: *Journal of Micromechanics and Microengineering* 15.5 (Mar. 2005), p. 966. DOI: [10.1088/0960-1317/15/5/010](https://doi.org/10.1088/0960-1317/15/5/010). URL: <https://dx.doi.org/10.1088/0960-1317/15/5/010>.
- [36] Chia-Chin Chen et al. “Simulation and experiment research on vaporizing liquid micro-thruster”. en. In: *Sensors and Actuators A: Physical* 157.1 (Jan. 2010), pp. 140–149. ISSN: 09244247. DOI: [10.1016/j.sna.2009.10.025](https://doi.org/10.1016/j.sna.2009.10.025).
- [37] J.W. Cen and J.L. Xu. “Performance evaluation and flow visualization of a MEMS based vaporizing liquid micro-thruster”. en. In: *Acta Astronautica* 67.3-4 (Aug. 2010), pp. 468–482. ISSN: 00945765. DOI: [10.1016/j.actaastro.2010.04.009](https://doi.org/10.1016/j.actaastro.2010.04.009).
- [38] Y. Gao, Y.F. Ma, and J. T. Liu. “A review of the vaporizing liquid microthruster technology”. In: *2014 ISFMFE - 6th International Symposium on Fluid Machinery and Fluid Engineering*. 2014, pp. 1–3. DOI: [10.1049/cp.2014.1220](https://doi.org/10.1049/cp.2014.1220).

A | Literature

A.1 Assumptions

A.1.1 Propulsion calculations

Some assumptions are made to assume ideal conditions. These may not hold true for low atmosphere satellites etc. but should be close enough to look into the design of a non-specialized propulsion system. An ideal rocket propulsion unit is defined in the book "Rocket Propulsion Elements"[20] as one for which the following assumptions are valid for this report:

1. The working fluid (which usually consists of chemical reaction products) is homogeneous in composition.
2. All the species of the working fluid are treated as gaseous. Any condensed phases (liquid or solid) add a negligible amount to the total mass.
3. The working fluid obeys the perfect gas law.
4. There is no heat transfer across any and all gas-enclosure walls; therefore, the flow is adiabatic.
5. There is no appreciable wall friction and all boundary layer effects may be neglected.
6. There are no shock waves or other discontinuities within the nozzle flow.
7. The propellant flow rate is steady and constant. The expansion of the working fluid is uniform and steady, without gas pulsations or significant turbulence.
8. Transient effects (i.e., start-up and shutdown) are of such short duration that they may be neglected.
9. All exhaust gases leaving the rocket nozzles travel with a velocity parallel to the nozzle axis.
10. The gas velocity, pressure, temperature, and density are all uniform across any section normal to the nozzle axis.
11. Chemical equilibrium is established within the preceding combustion chamber and gas composition does not change in the nozzle (i.e., frozen composition flow).
12. Ordinary propellants are stored at ambient temperatures. Cryogenic propellants are at their boiling points.

A.2 Purpose of Propulsion in Micro-Spacecraft

Satellites have various requirements and functions once in space. These include orbital maneuvering, interplanetary travel and interstellar travel. Most micro-satellites are launched without any propulsion systems in such a manner that they eventually fall back down to earth at the end of their life. However adding propulsion to these devices could increase their useful life as well as augment some of their functions. The various applications of micro-propulsion systems are explained in this section.

A.2.1 Attitude control

Attitude control is the process of controlling the orientation of a satellite with respect to an inertial frame of reference (or another entity such as the earth, other satellites etc. Controlling vehicle attitude requires sensors to measure vehicle orientation and actuation devices to apply the torques needed to orient the vehicle to a desired attitude with a feedback loop connecting the two.

The actuation can be done using a variety of methods such as magnetorquer, solar pressure, gravity stabilization, etc. However, mass expulsion(using active propulsion systems) could easily be used as it would be a complete system and not require any extra elements. Propulsion controlled attitude control allows for 3 axis stabilization as well as orientation. For example if a satellite must be oriented to the earth center at all times when in an elliptical orbit as shown in [Figure A.1](#).

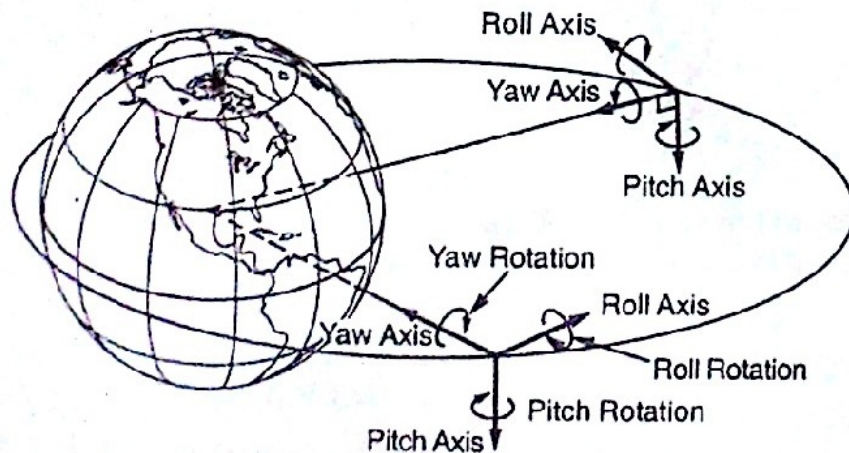


Figure A.1: Satellite orientations wrt earth center[21]

A.2.2 Drag compensation

The atmosphere is a thin layer of gases, held to the surface of the planet by gravitational attraction. The force interactions between the spacecraft and the atoms depends on the thermodynamic properties of the atmospheric gases. These gases and properties vary with gravity, planetary rotation, chemical composition, solar radiation and magnetic field.

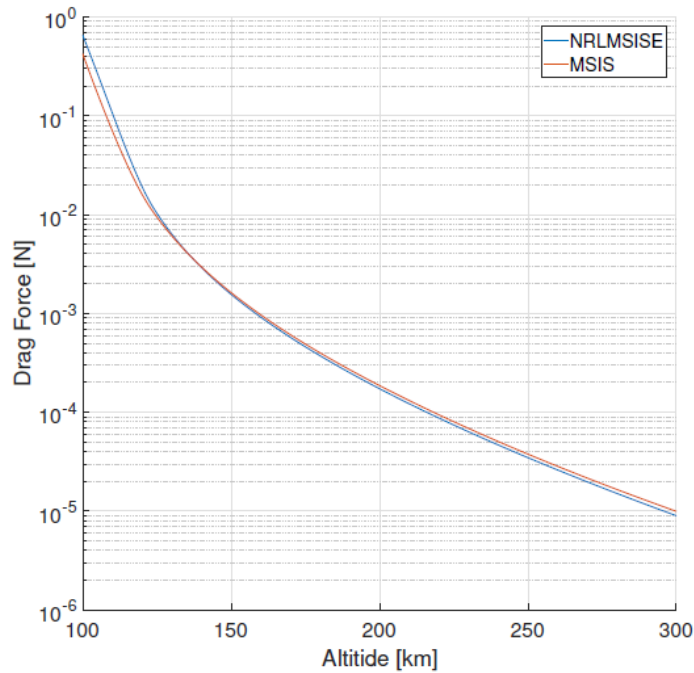


Figure A.2: Drag force vs Satellite altitude shows that low orbit satellites need higher drag compensating propulsion [22]

These effects have to be compensated for. The amount of drag acting on a satellite is approximated in Figure A.2. Periodic propulsion is required to maintain altitude and speed. When solar activity is at its greatest over the 11-year solar cycle, satellites may have to be maneuvered every 2-3 weeks to maintain their orbit [23].

A.2.3 Station keeping

Station-keeping, in astrodynamics, is maintaining a spacecraft at a fixed distance from another celestial body. This may be a planet a moon or another satellite. This is done by making a series of maneuvers using propulsion systems to keep the active craft in the same orbit as its target. An example of a macro satellite that uses intermittent station keeping is the James Web telescope to maintain its halo orbit around the Earth-Sun L2 for ten years. [24]. This same idea is also useful in small satellites that must be oriented with respect to other satellites in a cluster for communications applications. For data collection Smallsats stationkeeping for north/south orbit maintenance for a GEO spacecraft traditional station-keeping for north/south orbit maintenance for a GEO spacecraft is still required similar to larger satellites.

A.2.4 Orbit adjustment

There are quite a few situations where slight or major adjustments to the orbit may be required. These are listed below:

- To avoid other satellites without active altitude control and space Debris. Currently a very high number of satellites are orbiting the earth as shown in Figure A.3(a). There

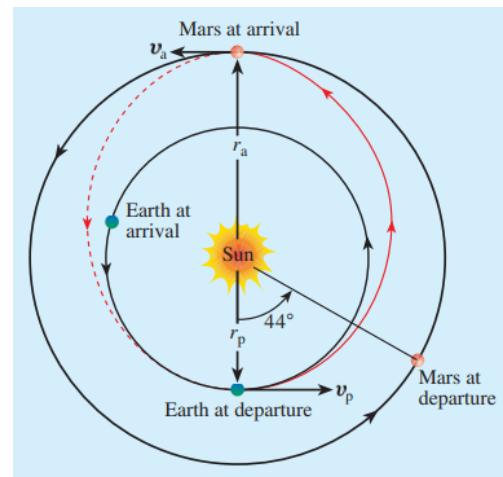
is a slight chance that flight paths interfere.

- Hohmann transfer orbit is an elliptical orbit used to transfer between two circular orbits of different altitudes, in the same plane. This maybe used by some communication minisats.
- A space rendezvous in which a satellite must approach to a very close distance (e.g. within visual contact) with a space station for visual inspection. Rendezvous may or may not be followed by docking or berthing, procedures which bring the spacecraft into physical contact and link them (usually temporarily for upgrades or repairs).

This adjustment will be carried out by various means depending on the requirement and satellite capabilities. The most common is an impulsive maneuver where a sudden change in velocity is forced upon the satellite changing its trajectory. The other possibility is low thrust propulsion for a long time period (non-impulsive maneuver). this is used usually for space rendezvous and in electrically propelled spacecraft.



((a)) Visualization of the space debris environment for objects in 2018 [25]



((b)) A Hohmann orbit transfer (HOT) trajectory [26]

Figure A.3: Orbital adjustment applications

A.3 History of Satellite miniaturization

The concept of miniaturized satellites has been around for a while. The very first satellites launched into orbit (1950s and 1960s) such as Sputnik I, Explorer 1, etc. were relatively small and their mass was only a few kilograms but were not classified as such since lift capacity of the launch vehicles in those days could not carry much payload. The power was also quite limited due to the technology of the time. From 1960s to 2010s satellites became more capable, higher-powered, and kept growing in size, while decreasing in cost.

ATK came up with the idea of small LEO satellites for message relay, and this system was known as Orbcomm. Another system called Teledesic was to have had 840 satellites plus 80 spares. More such ideas were proposed to design, manufacture, and launch a large number of “smaller” satellites into large-scale constellations – mostly in low Earth orbit (LEO). [27]

Experts worked with amateur radio operators to design and build at low cost small satellites for global radio connectivity. These satellites known as Oscar 1, Oscar 2, etc. proved that low-cost satellites were possible to design and build and that simpler methods and materials could produce viable spacecraft at lower cost[28]. NASA and other space agencies created the concept of the cubesat that was 10 cm X 10 cm X 10 cm in size. Bob Twiggs, a faculty member at Morehead State University, formally proposed a “PocketQube satellite” that was one-eighth the size of a cubesat. This “pico-sat” configuration that was 5 cm X 5 cm X 5 cm in size was first flown in November 2013 with four PocketQube satellites packaged together with the Unisat-4 launch. [27]

The predominant source of these new smallsat deployments has been from start-ups who have embraced entirely new models of how to design, test, launch, and operate smallsat system. Planet and Spire Global, two smallsat start-ups, have been responsible for about 40% of the over 1000 smallsats launched, while the much longer established Orbcomm network deployed less than 2% in 2019.[27] Today most of the smallsat launches are for communications and are predominantly part of the Starlink and OneWeb systems as shown in Figure A.5

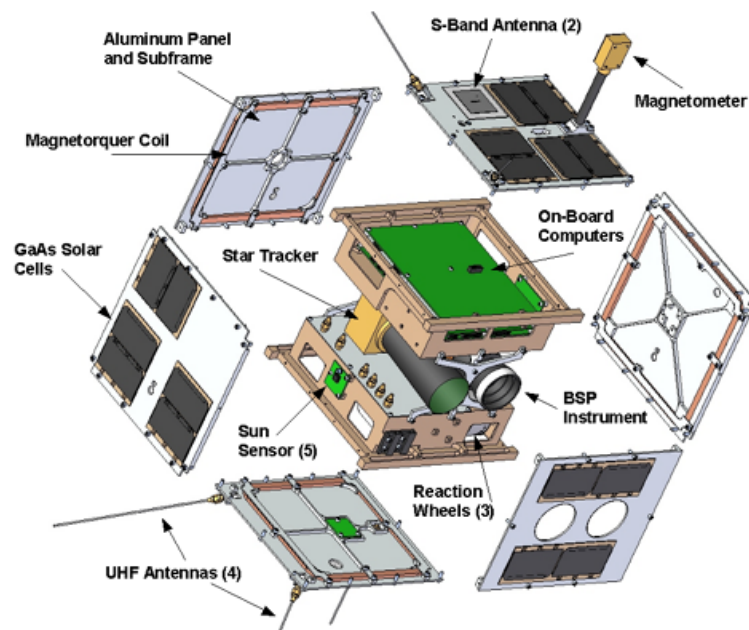


Figure A.4: Exploded view of basic components of a “cubesat”[29]

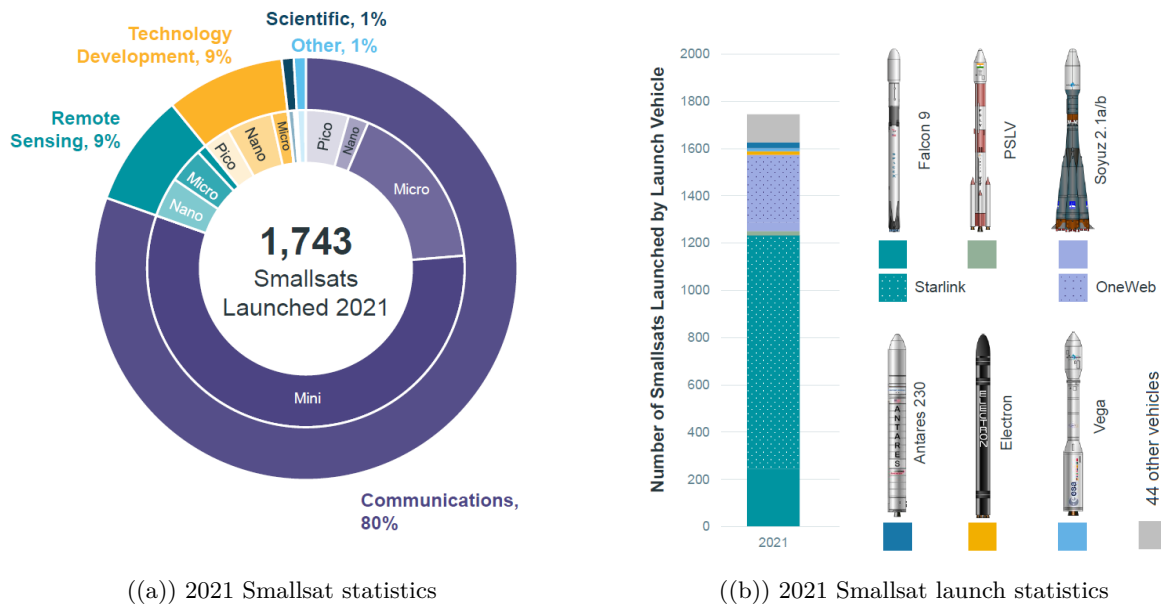


Figure A.5: Smallsat statistics for 2021 [30]

As of today the classification of spacecraft mass classes used by FAA AST is shown in Table A.1

Class	Weight (kg)
Femto	0.01 – 0.1
Pico	0.09 – 1
Nano	1.1 – 10
Micro	11 – 200
Mini	201 – 600
Small	601 – 1,200
Medium	1,201 – 2,500
Intermediate	2,501 – 4,200
Large	4,201 – 5,400
Heavy	5,401 – 7,000
Extra Heavy	> 7,001

Table A.1: Spacecraft mass classes[31]

A.4 History of VLM Development

VLMs are the most common microresistojet concepts. It is generally manufactured using MEMS processes in silicon or ceramic wafers. The propellant is fed through an inlet into a accelerating chamber with a heater, it undergoes phase change and accelerates into a convergent-divergent nozzle where it achieves supersonic velocities.

Fontanarosa et al.[32] have created a comprehensive overview of experimental VLMs designed and fabricated till date. The first concept of a silicon-based MEMS VLM developed by Mueller's studies[33] in the 1990s. Mukerjee et al. [34] developed a MEMS-based VLM using

water as the fuel heated externally producing a 0.46mN of thrust. Maurya et al.[35] integrated a micro-heater. Chen et al.[36] evaluated 4 flow patterns: snake flow, vapor-droplet flow, vapor-droplet-jet flow, and vapor flow. Cen and Xu[37] fabricated thruster with parallel microchannels found a new performance limit - flow boiling instabilities. Next, different configurations, materials, and manufacturing technologies were investigated, explained by Gao et al.[38]. This brings us to the current state of the art continued in subsection 2.3.1.

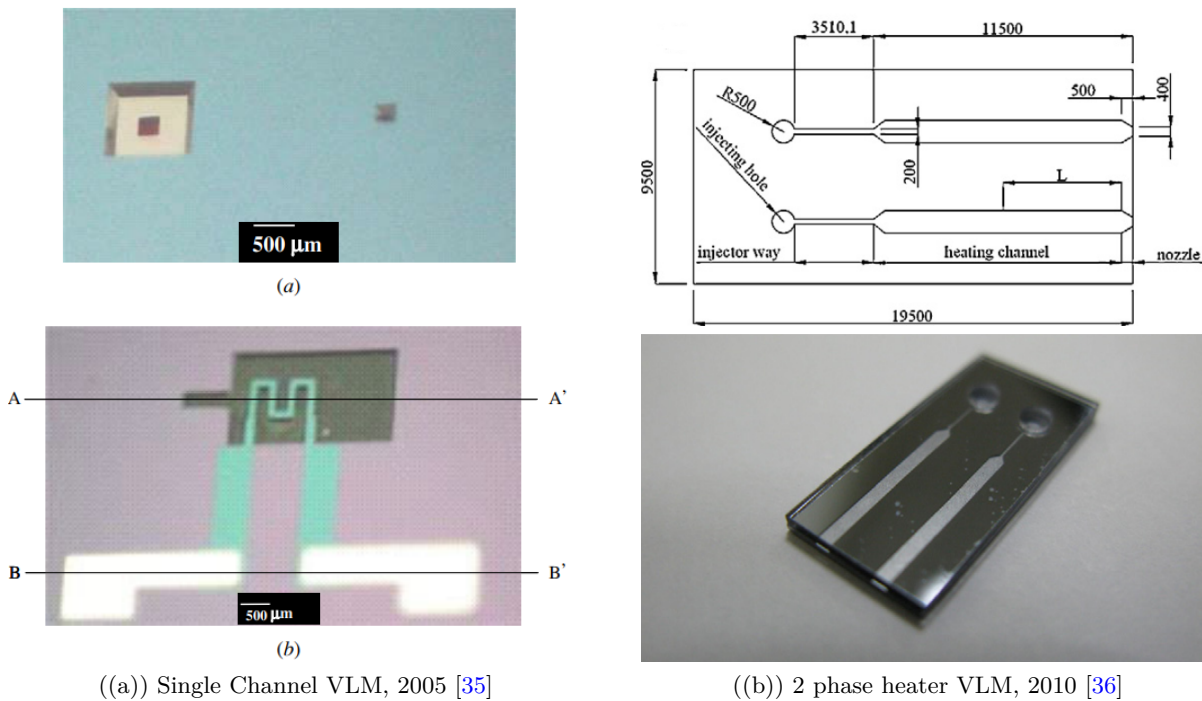


Figure A.6: Chemical Propellant systems

B | Fabrication

B.1 Complete Fabrication Flowchart - New VLM Design

this section includes the final flowchart for fabrication of the new thruster design. For other flow charts (such as old VLM thruster design or LPM thruster) please contact Dr. Henk van Zeijl or Dr. Angelo Cervone.

VLM Wafer Manufacturing New Inlet

FLOWCHART

VERSION 1

2023

BATCH INFORMATION			
NAME OF OWNER :	Sampuran Singh	MASK SET :	MICROT
NAME OF MENTOR :	Henk van Zeijl	MASK BOX :	MICROT2
RUN NUMBER :	1	DIE SIZE :	Custom (7mmX1.28mm)
WAFER AMOUNT :	5	START DATE :	18/08/2023
SUBJECT TO PCC :		PCC APPROVED :	

**DELFT UNIVERSITY OF TECHNOLOGY ELSE
KOOI LABORATORY**

Adress : Feldmannweg 17, 2628 CT Delft, The Netherlands
P.O. Box : 5053, 2600 GB Delft, The Netherlands
Phone : +31 - (0)15 - 2783868
Fax : +31 - (0)15 - 2622163
Website : www.tudelft.nl/ewi/onderzoek/faciliteiten/else-kooi-lab

© Copyright EKL - Delft University of Technology

STARTING MATERIAL

Use **SINGLE SIDE** polished **LOW RESISTIVITY (LRES)** wafers,
with the following specifications:

Type:	NA
Orientation:	<100>
Resistivity:	1-5 Ω cm
Thickness:	300 \pm 10 μ m
Diameter:	100 mm



- *SiO₂ deposition top side STEP 10-11*



- *SiO₂ backside deposition STEP 12-13*



- *Metal Stacking STEP 14-17*



- *Aluminium pads STEP 18-24*



- *Titanium heaters STEP 25-31*



- *SiO₂ Hard mask etch STEP 32-38*



- *Protective photoresist and Si etch 39-41*



- *SiO₂ & Photoresist removal STEP 42-43*



- *Anodic Bonding – Glass Wafer STEP 44*



- *Dicing STEP 45*



ZERO LAYER

1. CLEANING: HNO₃ 99% and 69.5%

Clean 10 minutes in fuming nitric acid at ambient temperature. This will dissolve organic materials.

Use wet bench "HNO₃ 99% (Si)" and the carrier with the white dot.

Rinse Rinse in the Quick Dump Rinser with the standard program until the resistivity is 5 MΩ.

Clean 10 minutes in concentrated nitric acid at 110 °C. This will dissolve metal particles.

Use wet bench "HNO₃ 69,5% 110C (Si)" and the carrier with the white dot.

Rinse Rinse in the Quick Dump Rinser with the standard program until the resistivity is 5 MΩ.

Dry Use the "Avenger Ultra-Pure 6" rinser/dryer with the standard program, and the white carrier with a red dot.

2. COATING

Use the coater station of the EVG120 system to coat the wafers with photoresist. The process consists of:

- A treatment with HMDS (hexamethyldisilazane) vapor, with nitrogen as a carrier gas, to improve resist adhesion.
- Spin coating of Shipley SPR3012 positive resist, dispensed by a pump.
- A soft bake (a.k.a. pre-bake) at 95 °C for 90 seconds.
- An automatic Edge Bead Removal (EBR) with a solvent.

Always check the relative humidity ($48 \pm 2\%$) in the room before coating, and follow the instructions for this equipment.

Default use program "1 - Co - 3012 - zero layer", which has a larger Edge Bead Removal (EBR) than standard, or use program "1 - Co - 3012 - 1.4 - noEBR" when the EBR option is out of order.

3. ALIGNMENT AND EXPOSURE

Processing will be performed on the ASML PAS5500/80 automatic wafer stepper. Follow the operating instructions from the manual when using this machine.

Expose **mask COMURK** with job **Litho\epi 0.0**. Use the correct exposure energy (check the energy table). This results in stepper alignment markers and verniers for wafers which will not get an Epitaxy (EPI) layer.

4. DEVELOPING

Use the developer station of the EVG120 system to develop the wafers. The process consists of:

- A post-exposure bake at 115 °C for 90 seconds, to prevent *standing waves* on the sidewalls of the resist structures.
- Developing with Shipley MF322 with a single puddle process.
- A hard bake (a.k.a. post-bake) at 100 °C for 90 seconds. Always follow the instructions for this equipment.

Use program "1 - Dev - SP".

5. INSPECTION

Visually inspect the wafers through a microscope:

- Check if the correct mask is exposed.
- Check if there are no resist residues; these are NOT allowed.
- Check the linewidth of the structures.
- Check the overlay of the exposed pattern (if the mask was aligned to a previous pattern on the wafer).

6. WAFER NUMBERING

Use the glass pen in the lithography room to mark the wafers with the **BATCH** and **WAFER** number.

Write the numbers in the photoresist, just above the waferflat. Always do this after exposure and development ! It is **NOT** allowed to use a metal pen or a scribe (pen with a diamond tip) for this purpose.

7. PLASMA ETCHING: Alignment markers (URK's) into Silicon

Use the Trikon Ωmega 201 plasma etcher.

Follow the operating instructions from the manual when using this machine.

It is **not** allowed to change the process conditions and times from the etch recipe!

Use sequence **URK_NPD** (with a platen temperature of **20 °C**) to etch 120 nm deep ASM URK's into the Si.

Process conditions from chamber recipe URK_ETCH:						
Step	Gasses & flows	Pressure	Platen RF	ICP RF	Platen temp.	Etch time
1. breakthrough	CF ₄ /O ₂ = 40/20 sccm	5 mTorr	60 W	500 W	20 °C	0'10"
2. bulk etch	Cl ₂ /HBr = 80/40 sccm	60 mTorr	20 W	500 W	20 °C	0'40"

8. LAYER STRIPPING: Photoresist

Strip resist Use the Tepla Plasma 300 system to remove the photoresist in an oxygen plasma. Follow the instructions specified for the Tepla stripper, and use the quartz carrier. Use **program 1**: 1000 watts power and automatic endpoint detection + 2 min. overetching.

9. CLEANING: HNO₃ 99% and 69.5%

Clean 10 minutes in fuming nitric acid at ambient temperature. This will dissolve organic materials. Use wet bench "HNO₃ 99% (Si)" and the carrier with the white dot.

Rinse Rinse in the Quick Dump Rinsers with the standard program until the resistivity is 5 MΩ.

Clean 10 minutes in concentrated nitric acid at 110 °C. This will dissolve metal particles.

Use wet bench "HNO₃ 69,5% 110C (Si)" and the carrier with the white dot.

Rinse Rinse in the Quick Dump Rinsers with the standard program until the resistivity is 5 MΩ.

Dry Use the "Avenger Ultra-Pure 6" rinsers/dryer with the standard program, and the white carrier with a red dot.

Oxide Layer deposition on both sides

10. PECVD DEPOSITION: 500 nm Silicon oxide (TEOS) on the front side of the wafer.

Use the Novellus Concept One PECVD reactor. Follow the operating instructions from the manual when using this machine. It is **not** allowed to change the process conditions and time from the deposition recipe!

Use recipe ".xxx_nm_teos" to deposit a 500 nm thick layer.

Process conditions from recipe .xxx_siostd:					
Gasses & flows	Pressure	HF power	LF power	Temperature	Time
N ₂ /SiH ₄ /N ₂ O = 3150/205/6000 sccm	2.2 Torr	1000 W	0 W	350 °C	16 sec

Note: ▪ The layer thickness depends on the station deposition time (SDT), which can be calculated from the average deposition rate during recent recipe usage. This can be found in the logbook of the system.

11. MEASUREMENT: Oxide thickness

Use the Woollam Ellipsometer system for layer thickness measurements on 1 wafer from each process. Follow the operating instructions from the manual when using this equipment. Expected layer thickness: 500 nm

12. Backside PECVD DEPOSITION: 4000nm Silicon oxide (TEOS) on the back side of the work.

Use the Novellus Concept One PECVD reactor. Follow the operating instructions from the manual when using this machine. It is **not** allowed to change the process conditions and time from the deposition recipe!

Use recipe ".xxxnm_teos" to deposit a 4000 nm thick layer.

Process conditions from recipe .xxx_siostd:					
Gasses & flows	Pressure	HF power	LF power	Temperature	Time
N ₂ /SiH ₄ /N ₂ O = 3150/205/6000 sccm	2.2 Torr	500 W	500 W	350 °C	140 sec

Note: ▪ The layer thickness depends on the station deposition time (SDT), which can be calculated from the average deposition rate during recent recipe usage. This can be found in the logbook of the system.

▪ An extra test wafer can be deposited for measurements and etch tests.

13. MEASUREMENT: Oxide thickness

Use the Woollam Ellipsometer system for layer thickness measurements on 1 wafer from each process. Follow the operating instructions from the manual when using this equipment.
Expected layer thickness: 4000nm

Metal Layer Stack

Front-Side of Wafer

14. **CLEANING: HNO₃ 99% and 69,5%**

Clean 10 minutes in fuming nitric acid at ambient temperature. This will dissolve organic materials.
Use wet bench "HNO₃ 99% (Si)" and the carrier with the white dot.

Rinse Rinse in the Quick Dump Rinser with the standard program until the resistivity is 5 MΩ.

Clean 10 minutes in concentrated nitric acid at 110 °C. This will dissolve metal particles.

Use wet bench "HNO₃ 69,5% 110C (Si)" and the carrier with the white dot.

Rinse Rinse in the Quick Dump Rinser with the standard program until the resistivity is 5 MΩ.

Dry Use the "Avenger Ultra-Pure 6" rinser/dryer with the standard program, and the white carrier with a red dot.

15. **METALLIZATION: 500 nm Ti**

Use the TRIKON SIGMA 204 sputter coater for the deposition of an Titanium metal layer on the wafers.

The target must exist of 100% Ti , and deposition must be done at 350 °C with an Ar flow of 100 sccm. Follow the operating instructions from the manual when using this machine.

Use recipe **Ti 500nm @ 350C** to obtain a 500 nm thick layer.

16. **METALLIZATION: 200 nm Al (with 1%Si)**

Use the TRIKON SIGMA 204 sputter coater for the deposition of an aluminium metal layer on the wafers.

The target must exist of 99% Al and 1% Si, and deposition must be done at 50 °C with an Ar flow of 100 sccm. Follow the operating instructions from the manual when using this machine.

Use recipe **AlSi 200nm @ 50C** to obtain a 200 nm thick layer.

17. **CLEANING: HNO₃ 99% metal**

Clean 10 minutes in fuming nitric acid at ambient temperature. This will dissolve organic materials.

Use wet bench "HNO₃ 99% (**metal**)" and the carrier with a red and white dot.

Rinse Rinse in the Quick Dump Rinser with the standard program until the resistivity is 5 MΩ.

Dry Use the "Avenger Ultra-Pure 6" rinser/dryer with the standard program, and the white carrier with a black dot.

Aluminium Bonding Pads

Front Side of Wafer

18. **COATING**

Use the coater station of the EVG120 system to coat the wafers with photoresist. The process consists of:

- A treatment with HMDS (hexamethyldisilazane) vapor, with nitrogen as a carrier gas, to improve resist adhesion.
- Spin coating of Shipley SPR3012 positive resist, dispensed by a pump.
- A soft bake (a.k.a. pre-bake) at 95 °C for 90 seconds. Always check the relative humidity (48 ± 2 %) in the room before coating, and follow the instructions for this equipment.

Use program "**1 - Co - Nlof - 1.5um--noEBR**",.

19. ALIGNMENT AND EXPOSURE

Processing will be performed on the ASML PAS5500/80 automatic wafer stepper. Follow the operating instructions from the manual when using this machine.

Expose mask **MICROT2** (box 502) with job **Job special/2023_Jobs/3ME_MiTh (Layer ID ALUPADS)**. Use the correct exposure energy (150).

20. DEVELOPING

Use the developer station of the EVG120 system to develop the wafers. The process consists of:

- A post-exposure bake at 115 °C for 90 seconds, to prevent *standing waves* on the sidewalls of the resist structures.
- Developing with Shipley MF322 with a single puddle process.
- A hard bake (a.k.a. post-bake) at 100 °C for 90 seconds. Followed by a Hard Bake.

Use program "x-Henk_DEVNLOF-1.5um_PB_HB".

21. INSPECTION

Visually inspect the wafers through a microscope:

- Check if the correct mask is exposed.
- Check if there are no resist residues; these are NOT allowed.
- Check the linewidth of the structures.

22. ALUMINIUM ETCHING

Moisten Rinse for 1 minute in wet bench "H₂O/Triton X-100 tvb Al. Ets". Use the carrier with the yellow dot. The bath contains 1 ml Triton X-100 per 5000 ml deionized water.

Etching Use wet bench "Al. ets 35°C", and the carrier with the yellow dot.
1 liter buffered aluminium etch fluid contains:
770 ml concentrated phosphorus acid (H₃PO₄ 85%), 19 ml concentrated nitric acid (HNO₃ 65%),
140 ml concentrated acetic acid (CH₃COOH 100%) and 71 ml deionized water.

Etch time 2min (slight overetch)

QDR Rinse in the Quick Dump Rinser with the standard program until the resistivity is 5 MΩ.

Drying Use the "Avenger Ultra-Pure 6" rinser/dryer with the standard program, and the white carrier with a black dot.

23. LAYER STRIPPING: Photoresist

Strip resist Use the Tepla Plasma 300 system to remove the photoresist in an oxygen plasma. Follow the instructions specified for the Tepla stripper, and use the quartz carrier. Use **program 4**: 1000 watts power for 15 minutes.

24. CLEANING: HNO₃ 99% metal

Clean 10 minutes in fuming nitric acid at ambient temperature. This will dissolve organic materials.
Use wet bench "HNO₃ 99% (metal)" and the carrier with a red and white dot.

Rinse Rinse in the Quick Dump Rinser with the standard program until the resistivity is 5 MΩ.

Dry Use the "Avenger Ultra-Pure 6" rinser/dryer with the standard program, and the white carrier

with a black dot.

Titanium Heating elements

Front-Side of Wafer

25. COATING

Use the coater station of the EVG120 system to coat the wafers with photoresist. The process consists of:

- A treatment with HMDS (hexamethyldisilazane) vapor, with nitrogen as a carrier gas, to improve resist adhesion.
- Spin coating of Shipley SPR3012 positive resist, dispensed by a pump.
- A soft bake (a.k.a. pre-bake) at 95 °C for 90 seconds. Always check the relative humidity ($48 \pm 2\%$) in the room before coating, and follow the instructions for this equipment.

Use program "1 - Co - Nlof - 1.5um--noEBR",.

26. ALIGNMENT AND EXPOSURE Ti Layer

Processing will be performed on the ASML PAS5500/80 automatic wafer stepper. Follow the operating instructions from the manual when using this machine.

Expose **mask MICROT2** (box 502) with job **Job special/2023_Jobs/3ME_MiTh (Layer ID HEATER)** Use the correct exposure energy (150).

27. DEVELOPING

Use the developer station of the EVG120 system to develop the wafers. The process consists of:

- A post-exposure bake at 115 °C for 90 seconds, to prevent *standing waves* on the sidewalls of the resist structures.
- Developing with Shipley MF322 with a single puddle process.
- A hard bake (a.k.a. post-bake) at 100 °C for 90 seconds. Followed by a Hard Bake.

Use program "x-Henk_DEVNLOF-1.5um_PB_HB".

28. INSPECTION

Visually inspect the wafers through a microscope:

- Check if the correct mask is exposed.
- Check if there are no resist residues; these are NOT allowed.
- Check the linewidth of the structures.

29. Titanium REMOVAL

Use the Trikon Omega 201 plasma etcher.

Follow the operating instructions from the manual when using this machine.

It is **not** allowed to change the process conditions and times from the etch recipe!

Use sequence Ti_500nm (with a platen temperature of **XXX °C**) to etch 500nm deep into the Ti layer.

Process conditions from chamber recipe Ti_500nm:						
Step	Gasses & flows	Pressure	Platen RF	ICP RF	Platen temp.	Etch time
1. breakthrough						15 s
2. bulk etch						1 m 05s
3. overetch						20 s

30. **LAYER STRIPPING: Photoresist**

Strip resist Use the Tepla Plasma 300 system to remove the photoresist in an oxygen plasma. Follow the instructions specified for the Tepla stripper, and use the quartz carrier. Use **program 4**: 1000 watts power for 15 minutes.

31. **CLEANING: HNO₃ 99% metal**

Clean 10 minutes in fuming nitric acid at ambient temperature. This will dissolve organic materials. Use wet bench "HNO₃ 99% (**metal**)" and the carrier with a red and white dot.

Rinse Rinse in the Quick Dump Rinsers with the standard program until the resistivity is 5 MΩ.

Dry Use the "Avenger Ultra-Pure 6" rinser/dryer with the standard program, and the white carrier with a black dot.

Silicon Oxide and Silicon etching of acceleration chamber, nozzle and new inlet and old inlet

Back-Side of Wafer

32. **COATING**

Use the coater station of the EVG120 system to coat the wafers with photoresist. The process consists of:

- A treatment with HMDS (hexamethyldisilazane) vapor, with nitrogen as a carrier gas, to improve resist adhesion.
- Spin coating of Shipley SPR3012 positive resist, dispensed by a pump.
- A soft bake (a.k.a. pre-bake) at 95 °C for 90 seconds. Always check the relative humidity (48 ± 2 %) in the room before coating, and follow the instructions for this equipment.

Use program **1 - Co - 3012 - 1.4 – noEBR**

33. **ALIGNMENT AND EXPOSURE**

Processing will be performed on the ASML PAS5500/80 automatic wafer stepper. Follow the operating instructions from the manual when using this machine.

For wafer 6 -Expose **mask MICROT2** (box 502) with job **Job special/2023_Jobs/3ME_MiTh/Wafer 6(Layer ID W06)**. Use the correct exposure energy (150). Similarly for wafer 7 – 10 use **Wafer 7-10 (Layer ID W07-10)**

34. **DEVELOPING**

Use the developer station of the EVG120 system to develop the wafers. The process consists of:

- A post-exposure bake at 115 °C for 90 seconds, to prevent **standing waves** on the sidewalls of the resist structures.
- Developing with Shipley MF322 with a single puddle process.
- A hard bake (a.k.a. post-bake) at 100 °C for 90 seconds. Followed by a Hard Bake.

Use program **"1 - Dev – SP"**

35. **INSPECTION**

Visually inspect the wafers through a microscope:

- Check if the correct mask is exposed.
- Check if there are no resist residues; these are NOT allowed.
- Check the linewidth of the structures.

36. **PLASMA ETCHING: 4000 nm oxide**

Use the Drytek Triode 384T plasma etcher. Follow the operating instructions from the manual when using this machine. It is **not** allowed to change the process conditions from the etch recipe, except for the etch time!

Use recipe **STDOXIDE** to etch the oxide layer. Set the Helium flow to 35. **Set the etch time to 200 seconds, then 200 seconds then 160 seconds.** 3 times to avoid burning of PR, instead of 1 long etch.

Process conditions from recipe STDOXIDE:					
Step	Gasses & flows	Pressure	RF power	He pressure	Etch time
1. bulk etch (RIE)	C ₂ F ₆ /CHF ₃ = 36/144 sccm	180 mTorr	300 W	12 Torr	variable

INSPECTION: No oxide residues are allowed on the etched areas.

37. LAYER STRIPPING: Photoresist

Strip resist Use the Tepla Plasma 300 system to remove the photoresist in an oxygen plasma. Follow the instructions specified for the Tepla stripper, and use the quartz carrier.

Use **program 1:** 1000 watts power and automatic endpoint detection + 2 min. overetching.

38. CLEANING: HNO₃ 99% metal

Clean 10 minutes in fuming nitric acid at ambient temperature. This will dissolve organic materials.

Use wet bench "HNO₃ 99% (**metal**)" and the carrier with a red and white dot.

Rinse Rinse in the Quick Dump Rinser with the standard program until the resistivity is 5 MΩ.

Dry Use the "Avenger Ultra-Pure 6" rinser/dryer with the standard program, and the white carrier with a black dot.

39. COATING front side (hater side) to protect it with Photoresist

Use the coater station of the EVG120 system to coat the wafers with photoresist. The process consists of:

- A treatment with HMDS (hexamethyldisilazane) vapor, with nitrogen as a carrier gas, to improve resist adhesion.
- Spin coating of Shipley 10XT positive resist, dispensed by a syringe.
- A soft bake (a.k.a. pre-bake) at 95 °C for 90 seconds. And hard bake for the thick layer

Use program "**1 - Co -Syr-10XT-6um-noEBR**",.

40. PLASMA ETCHING: Silicon Channels

Use the Rapier Omega i2L DRIE etcher.

Use sequence **EKL_FlatBottom_xxx** (with a platen temperature of **20 °C**) to etch 150um microthruster into the Si.

Parameter	Units	d1	E1	E2
Time	s	3	3	3
Primary Power	V	2200	2200	2200
Secondary Power	V	-	-	-
Platten Power	A	0	100	30
Coil Current	A	10	10	10
Pressure	torr	60	60	60
He Pressure	torr	8	8	8
SF ₆	sccm	1	450	450
C ₄ F ₈	sccm	350	1	1
O ₂	sccm	0	0	0
Ar	sccm	0	0	0

Etching Rate, Si	µm/cycle	2.41
	µm/m	10.5
Selectivity, Si/SiO ₂ ,		300
Sidewall angle (°)		90.5
Undercut (nm)		0

Sidewall	380nm scallops
Wafer Uniformity (%)	1
Ramping	No
Temperature (Å°C)	-10

41. INSPECTION

- Inspect using the Keyence VK-X250
- Check the depth of the etch
- Check the surface finish

42. Wet ETCHING: remove all remaining TEOS oxide from wafer

Moisten - Rinse for 1 minute in wet bench "H2O/Triton X-100 tbv BHF 1:7". Use the carrier with the blue dot. The bath contains 1 ml Triton X-100 per 5000 ml deionized water.

Etch - Use wet bench "BHF 1:7 (SiO2-ets)" at ambient temperature, and the carrier with the blue dot. The bath contains a buffered HF solution.

Time - Etch until the windows on the front side are hydrophobic, plus an extra 30 seconds. The required etch time depends on the layer thickness and composition. The etch rate of TEOS is 250-300 nm/min at 20 °C.

Rinse - Rinse in the Quick Dump Rinser with the standard program until the resistivity is 5 MΩ.

Dry - Use the "Avenger Ultra-Pure 6" rinser/dryer with the standard program.

Inspection - Visually, through a microscope: All the windows must be open and the hydrophobic test may be applied.

43. LAYER STRIPPING: Photoresist

Strip resist Use the Tepla Plasma 300 system to remove the photoresist in an oxygen plasma.
 Follow the instructions specified for the Tepla stripper and use the quartz carrier.
 Use **program 4**: 1000 watts power for 15 minutes.

Add borosilicate glass wafers for anodic bonding the glass wafers (double side and 500 μm thick)

44. ANODIC WAFER BONDING

Use the AML wafer bonder, follow the tool specific procedures for anodic bonding.

Anodic bonding will be performed with graphite sheets added to the wafer stack? 2 sheets sizes are available, 100 mm diameter and approximately 90 mm diameter. Note that the smallest sheet should be placed on the glass.

Load a graphite sheet on the cathode.

Load the silicon wafer on the sheet with the channels facing up.

Load the glass wafer.

Load the graphite sheet on the glass.

Wafer bonding conditions:

Vacuum

Load force = 4 kN.

Temperature = 400 °C.

Band voltage = 800 V.

Current ----- = 10 mA.

Time = 10 min.

Total charge > 2.3 Coulomb.

45. WAFER DICING

Leave Cleanroom to go do Dicing

The wafers must first be partially dices to remove unwanted Silicon

Then the complete dicing into 46 wafers can be done.

C | Characterization

C.1 Backup SEM Images

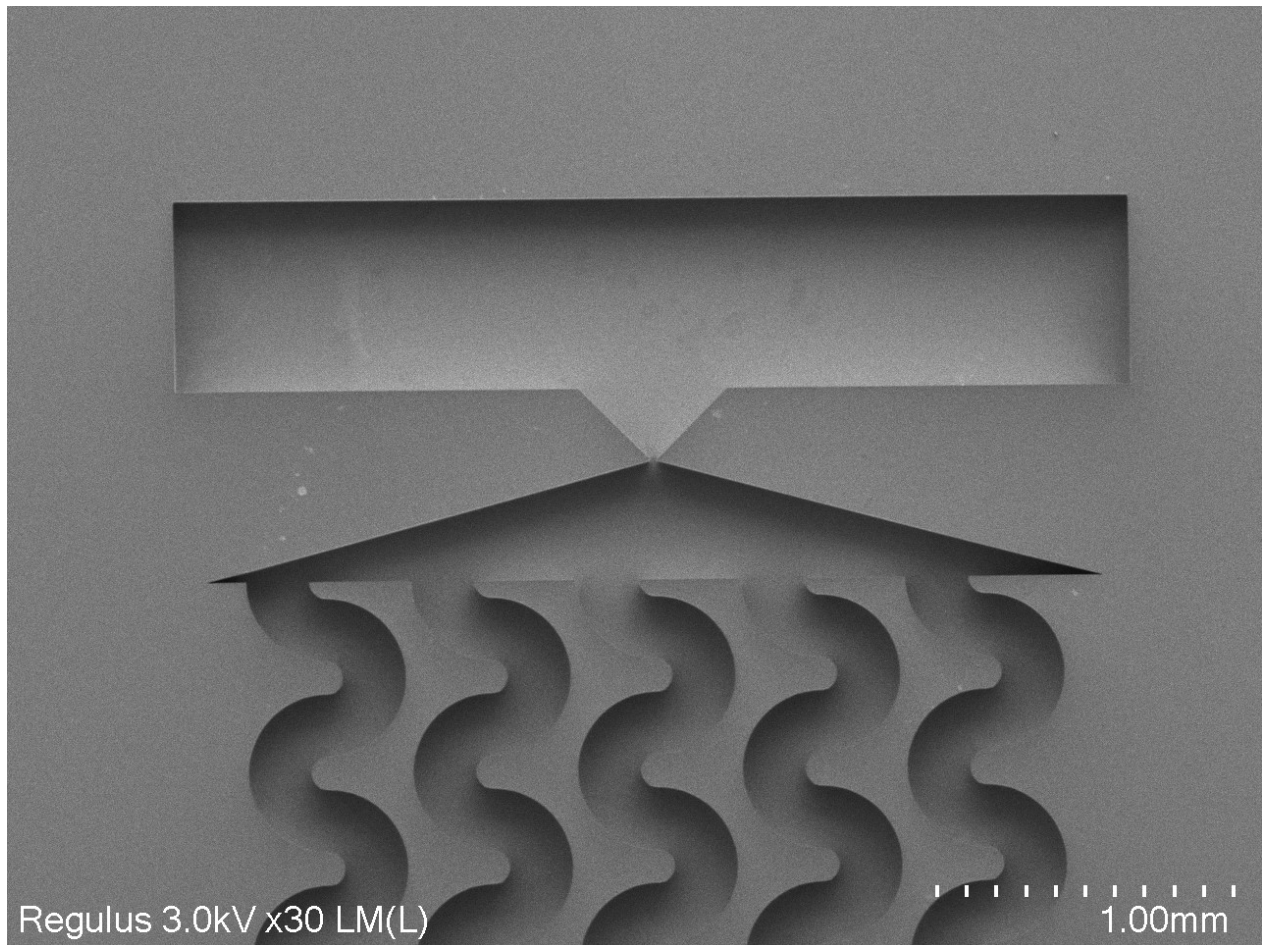


Figure C.1: 25 μm CD thruster

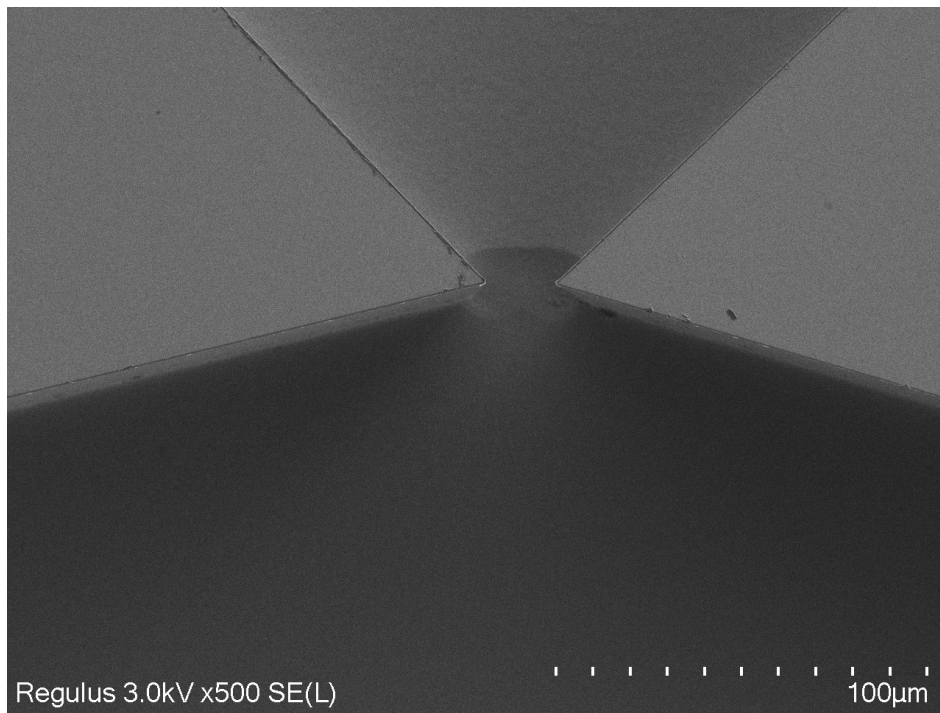


Figure C.2: 25 μm CD nozzle top view

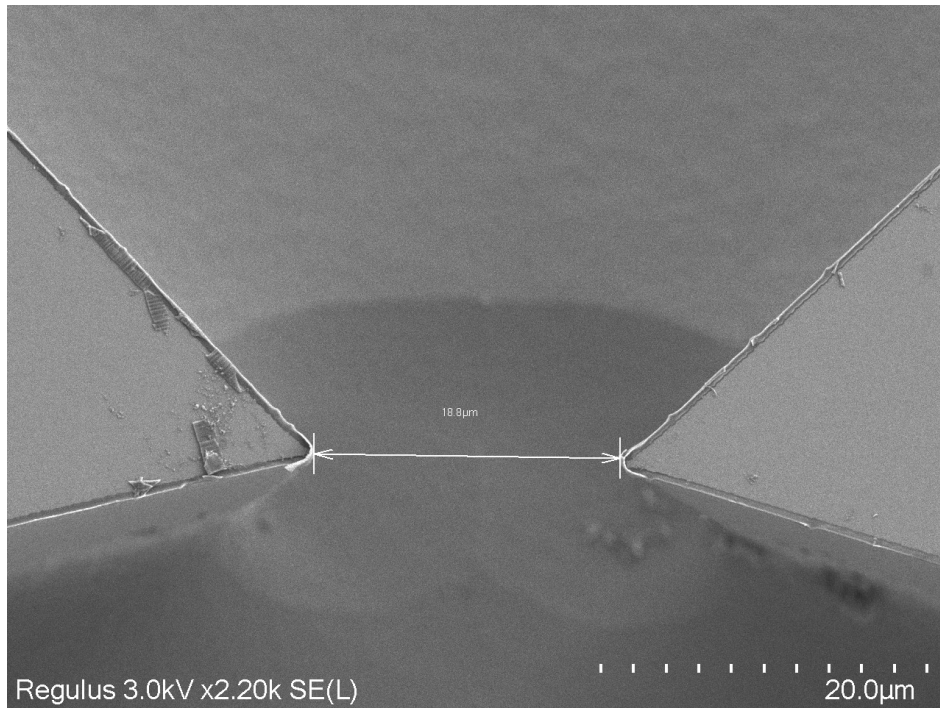


Figure C.3: 25 μm CD nozzle detailed top view- throat width

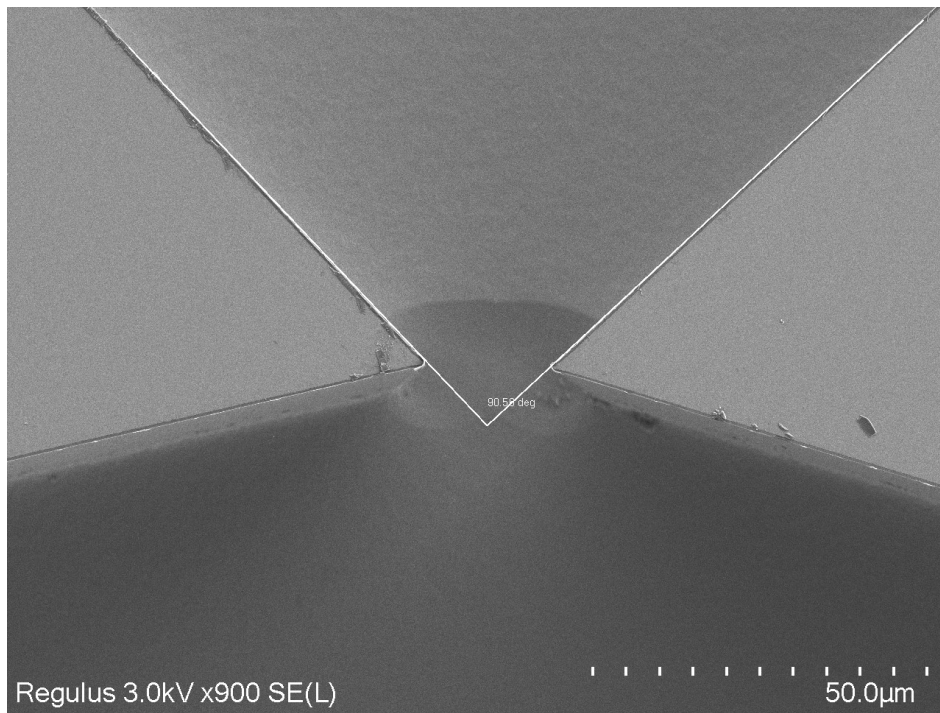


Figure C.4: 25 μm CD nozzle detailed top view- diverging angle

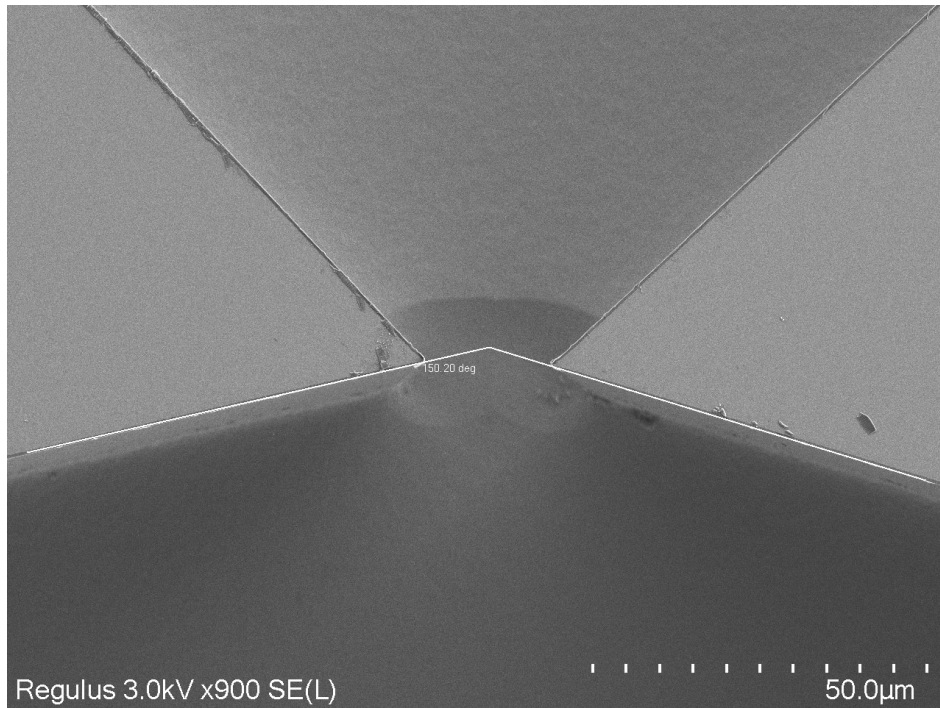


Figure C.5: 25 μm CD nozzle detailed top view- converging angle

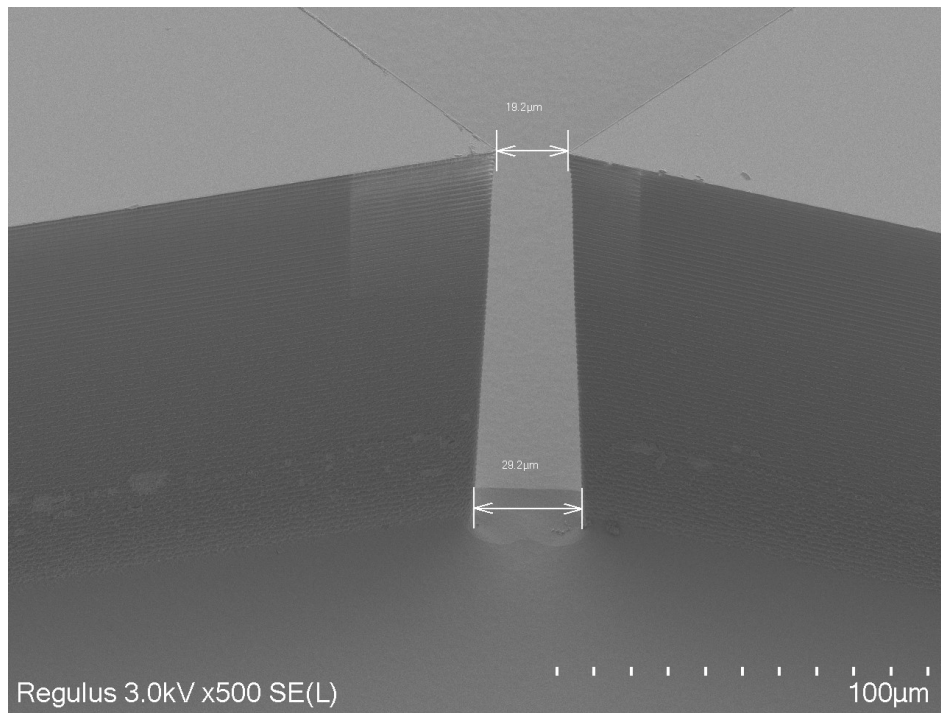


Figure C.6: 25 μm CD nozzle detailed angled view showing increase in throat width

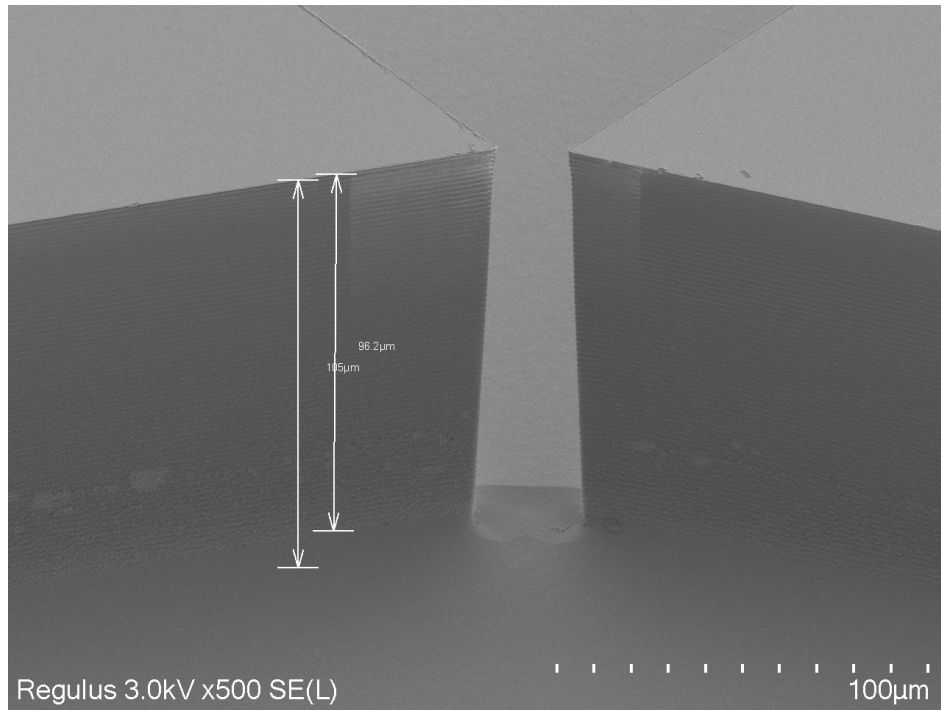


Figure C.7: 25 μm CD nozzle rounding at bottom Part 1

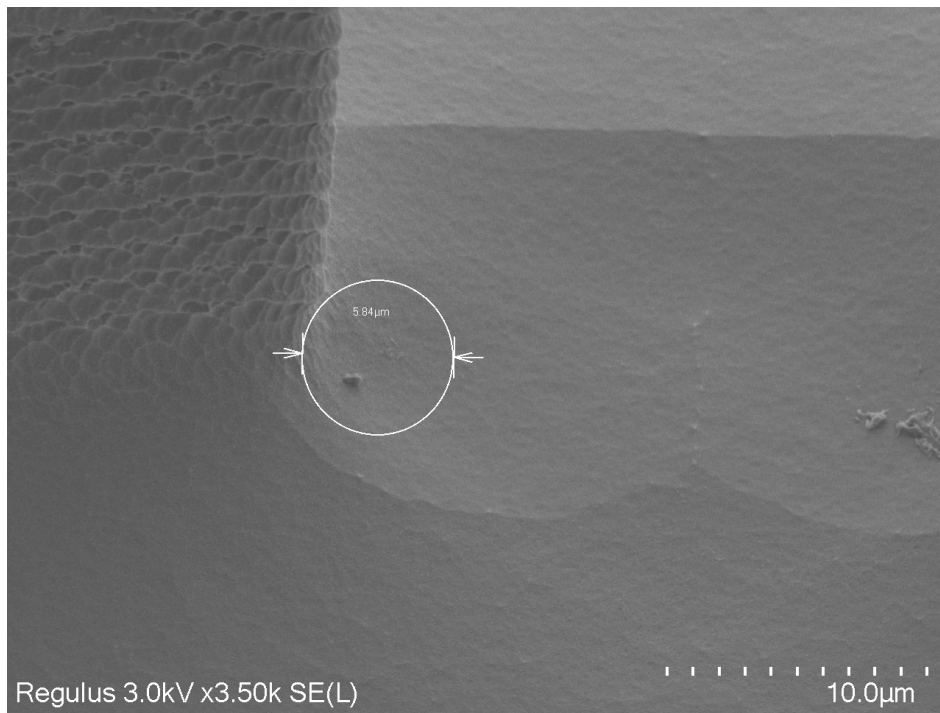


Figure C.8: 25 μm CD nozzle rounding at bottom Part 2

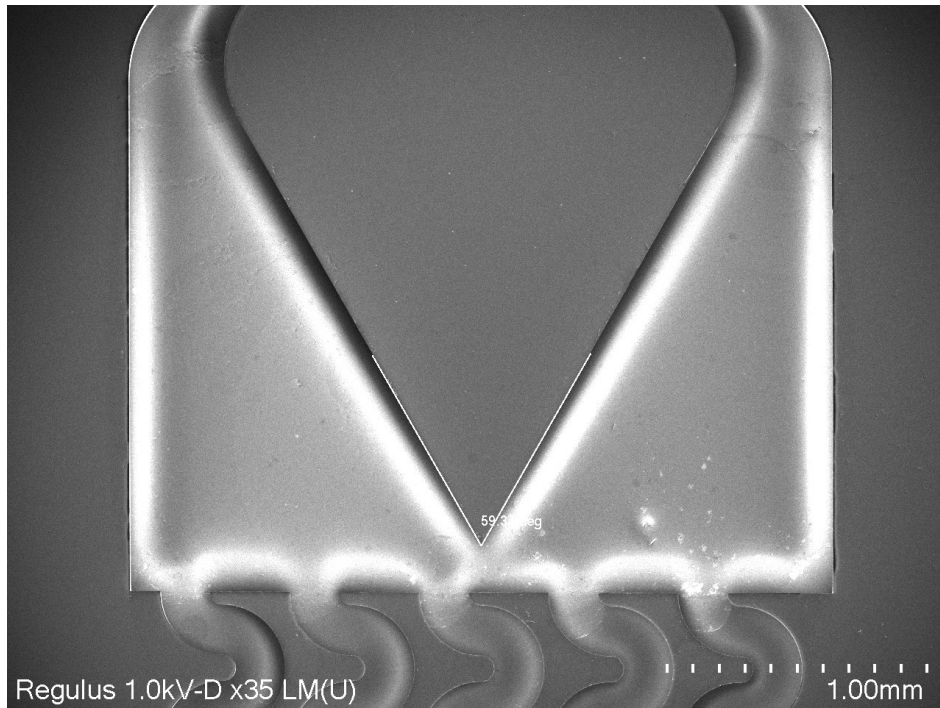


Figure C.9: 25 μm AS nozzle

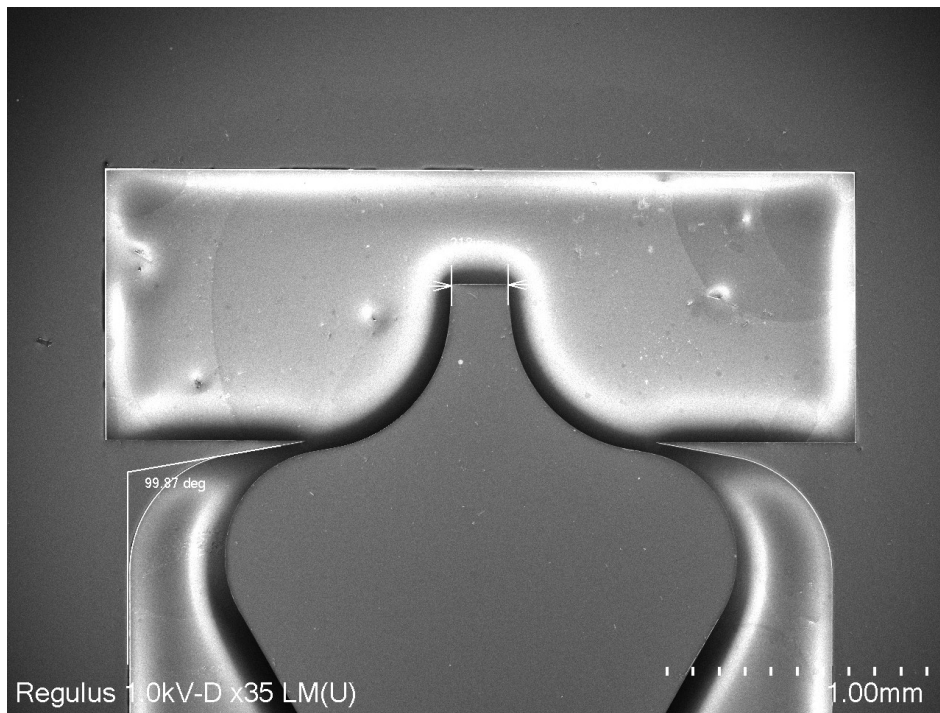


Figure C.10: 25 μm AS nozzle

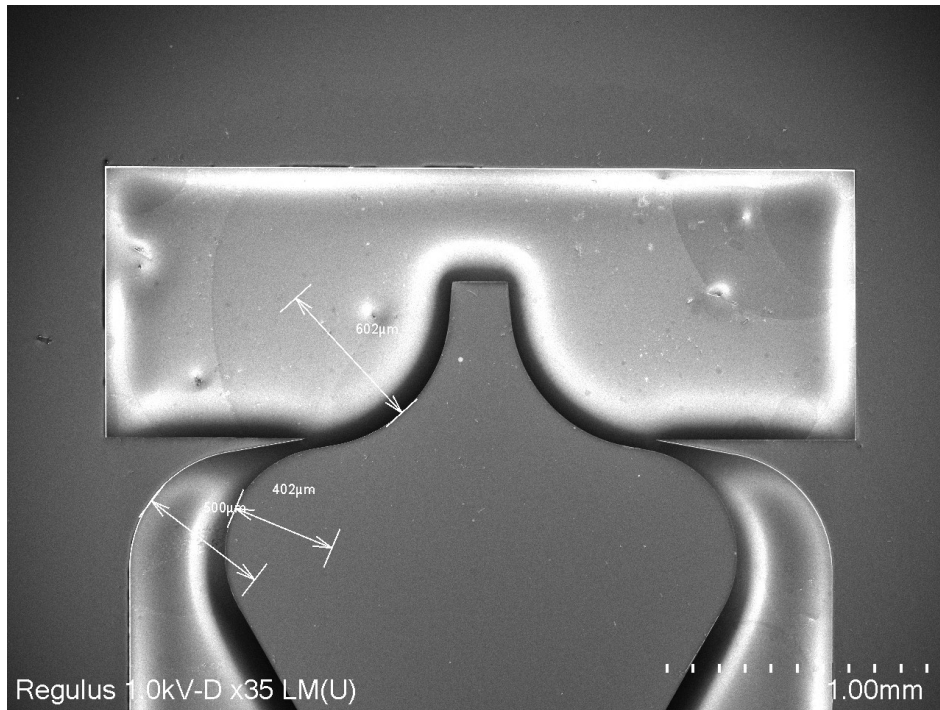


Figure C.11: 25 μm AS nozzle

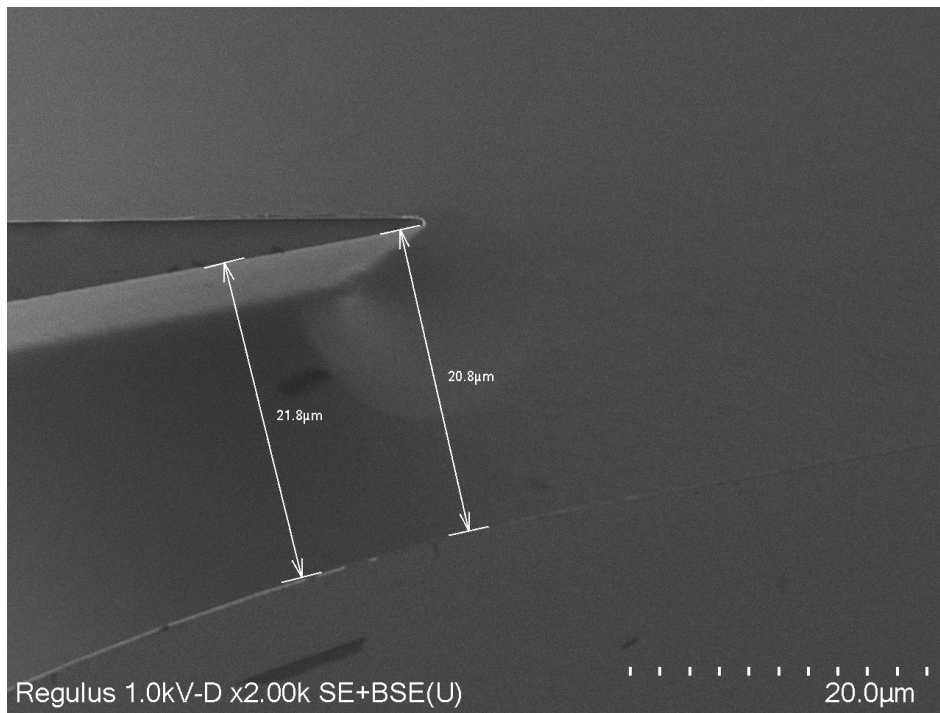


Figure C.12: 25 μm AS nozzle throat

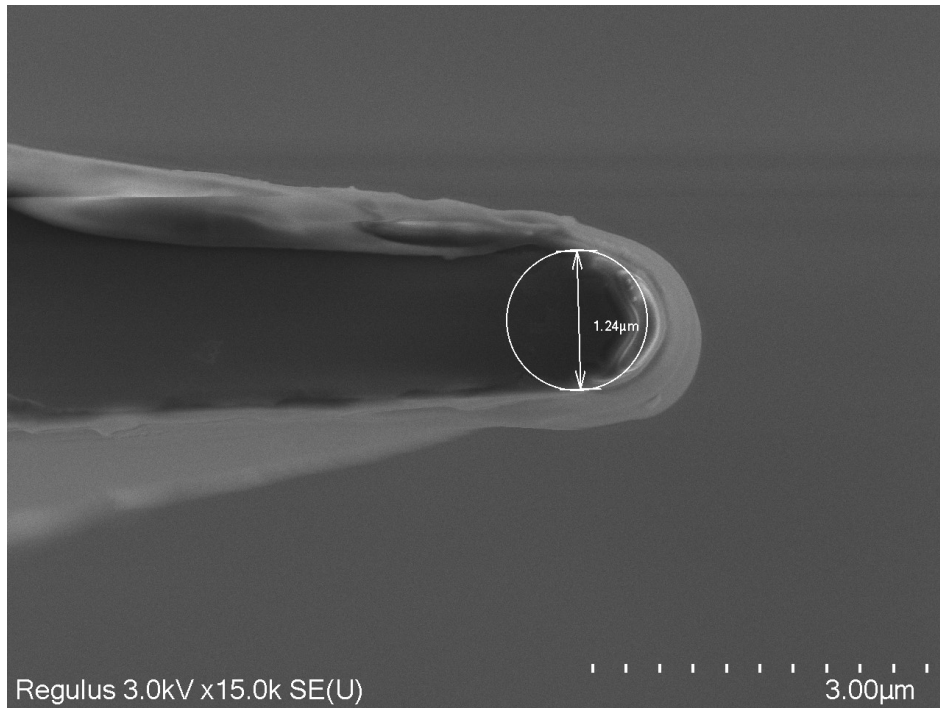


Figure C.13: 25 μm AS nozzle throat rounding off

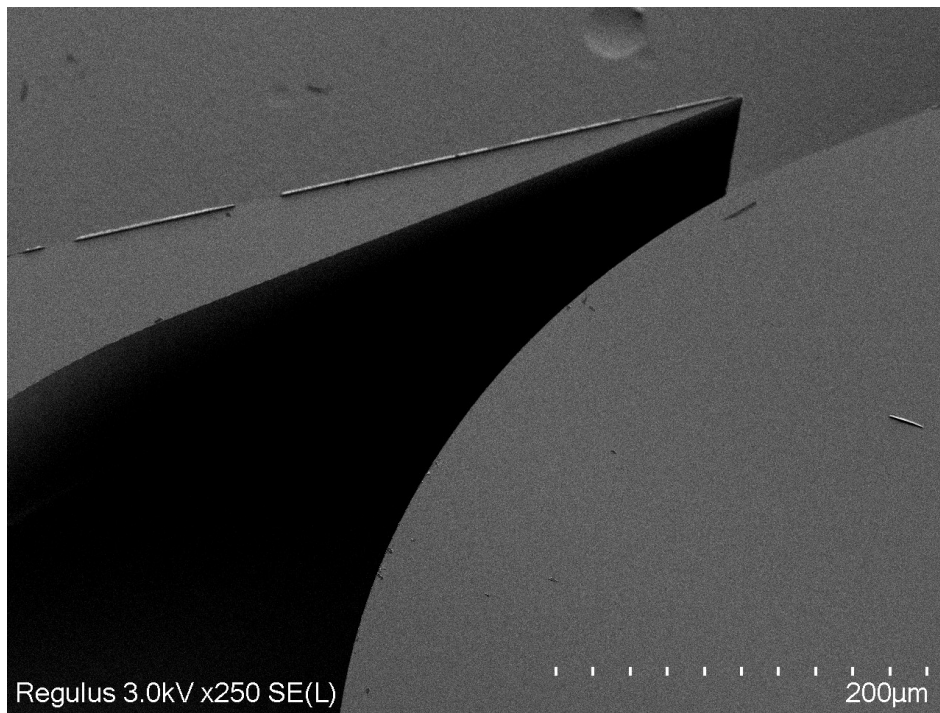


Figure C.14: 25 μm AS nozzle 3D illustration f throat

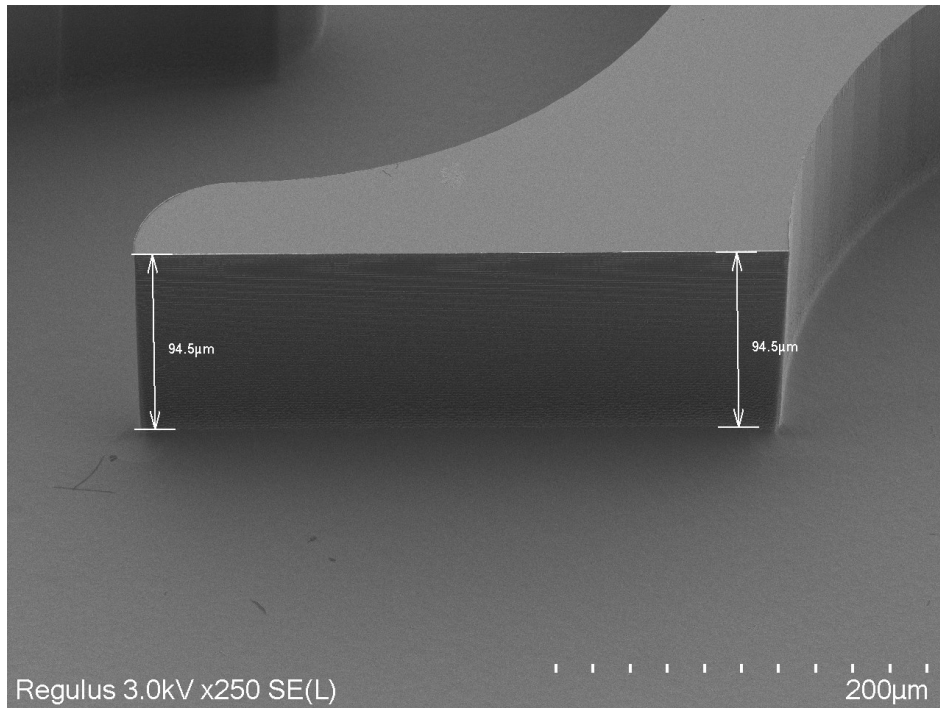


Figure C.15: Serpentine micro-channel inlet viewed at 45°

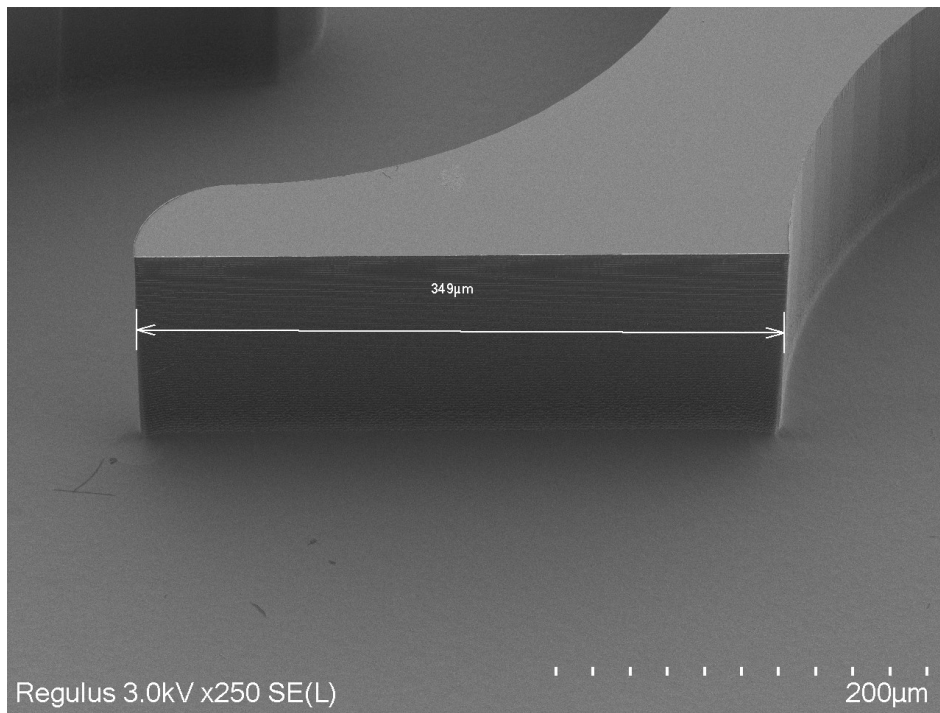


Figure C.16: Serpentine micro-channel inlet viewed at 45°

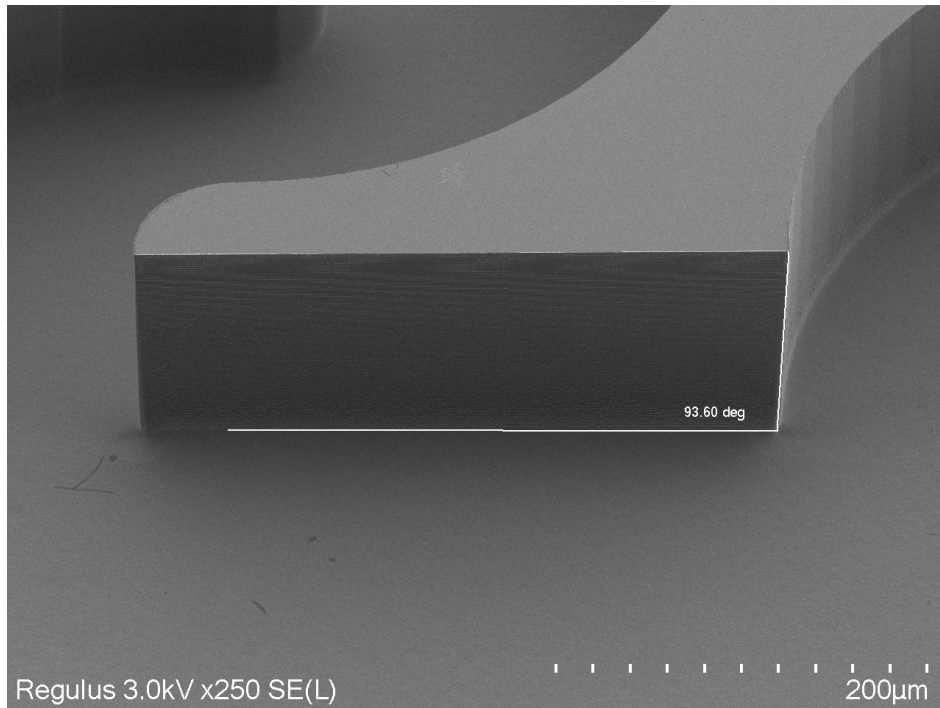


Figure C.17: Inclination of Serpentine micro-channel wall viewed at 45°

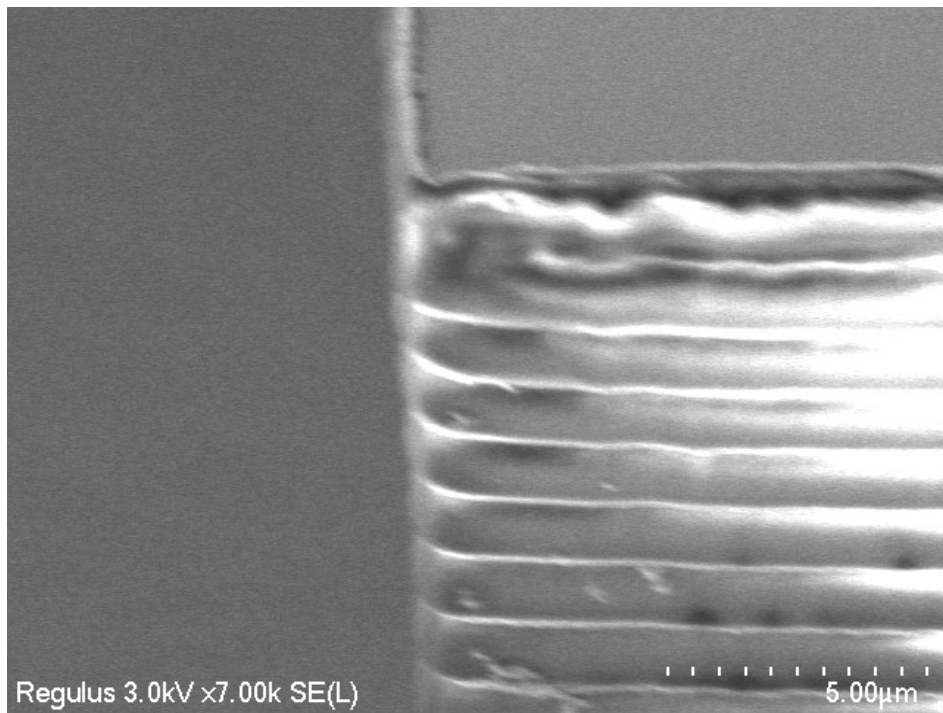


Figure C.18: Scallops on Serpentine micro-channel wall

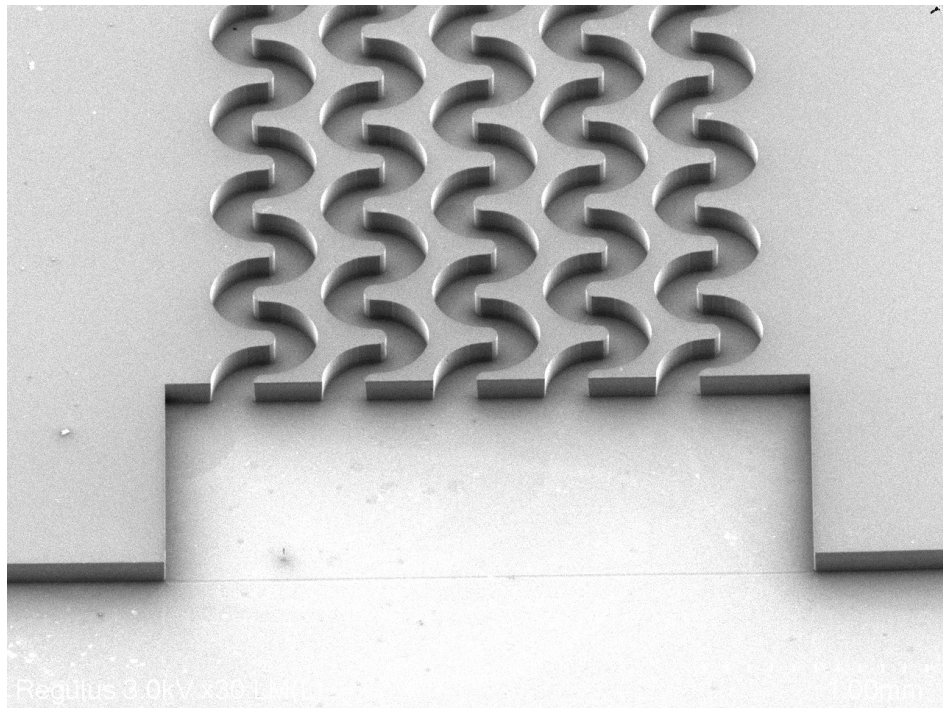


Figure C.19: Inlet to Serpentine micro-channel viewed at 45°

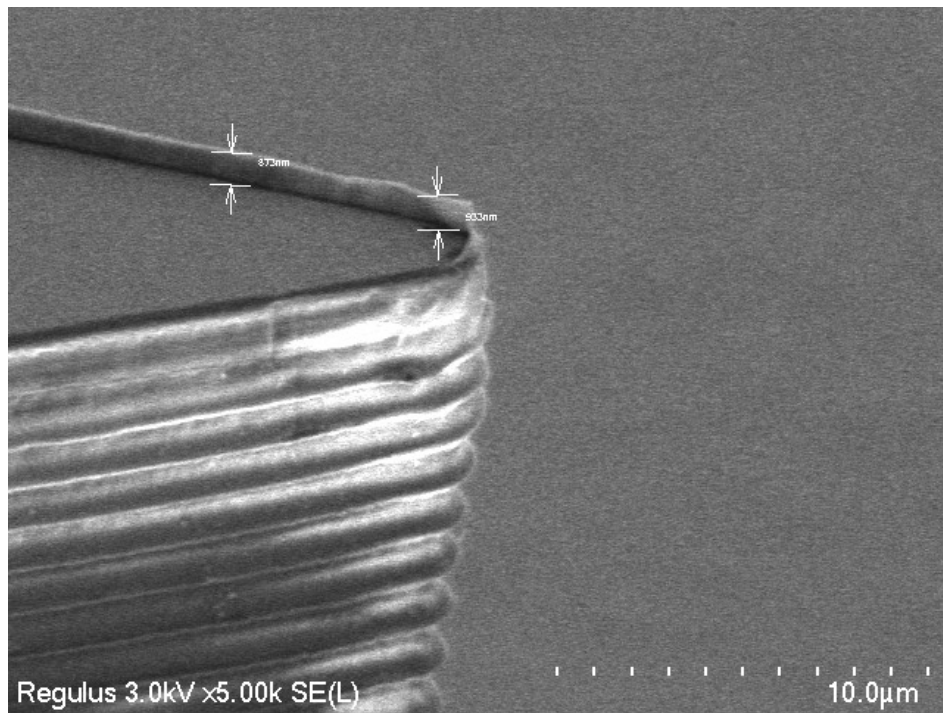


Figure C.20: Detailed view of Nozzle with scallops and some profile on the exit side

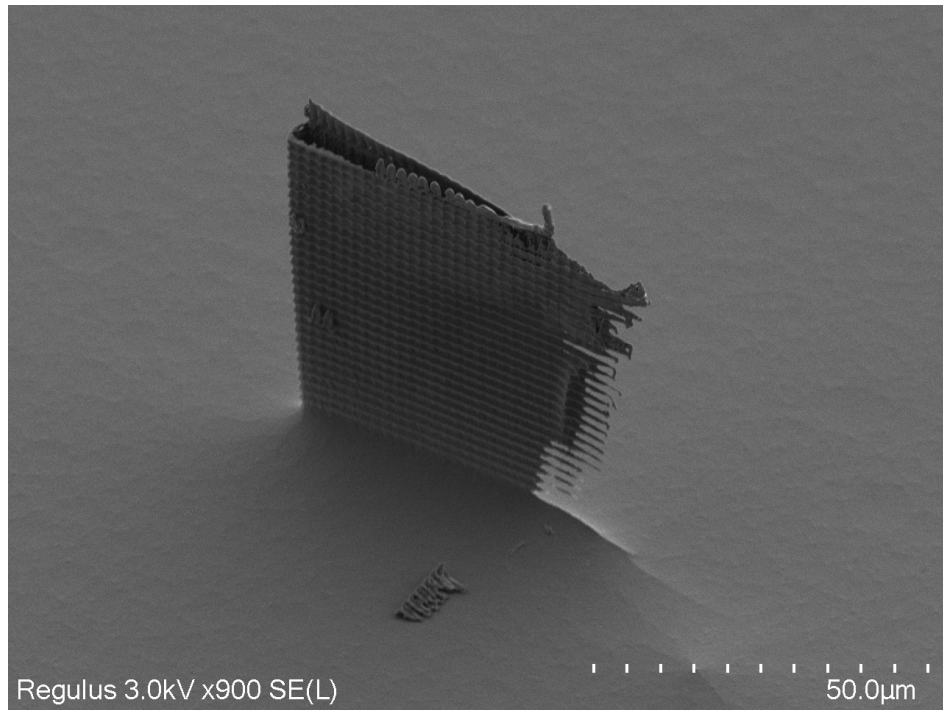


Figure C.21: Detailed view of etching artifact in Silicon

D | LPM and VLM previous Results

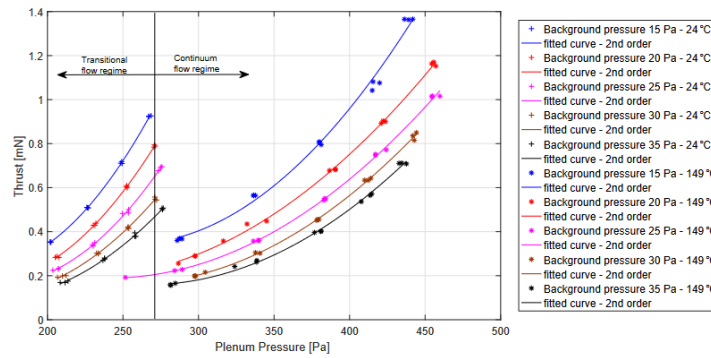


Figure D.1: Relationship between the plenum pressure and the thrust for different background pressure and different heater chip temperature for GLS chip by Gurrierri et al.[15]

P_0 [Pa]	T_w [°C]	\mathcal{Q} [mN]	I_{sp} [s]
200	24	0.6	53
200	149	0.7	63
300	24	0.9	53
300	149	1.1	63

Figure D.2: Thrust performance achieved by Gurrierri et al.[15]

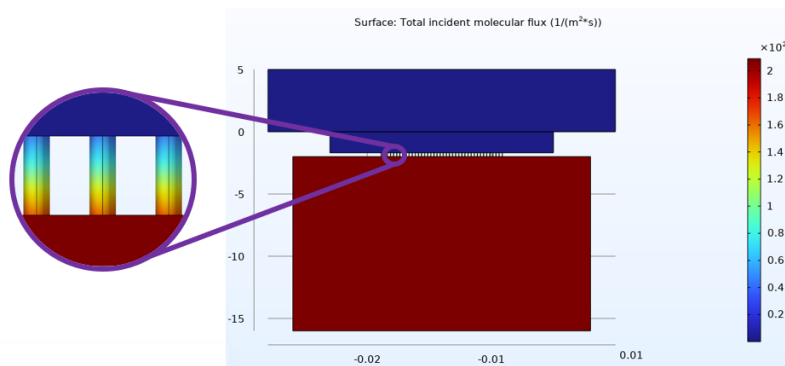


Figure D.3: Initial design Simulation result based on design of Gurrierri et al.[15]

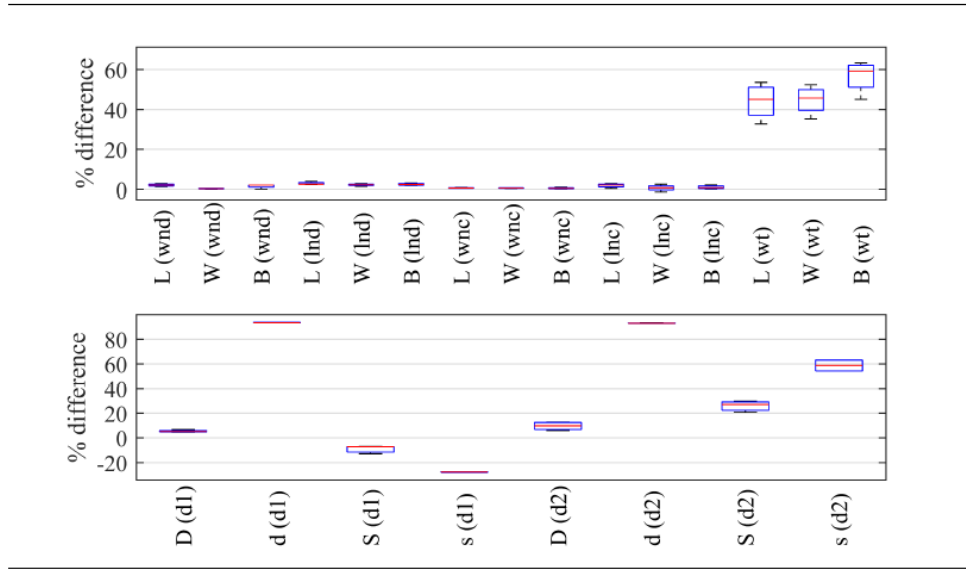


Figure D.4: VLM dimensional characterization by Silva et al.[5]

Table 3.7: Average measured values of the dimensions of the thrusters in μm . Design values are in brackets.

Type	w_{nd}	l_{nd}	w_{nc}	l_{nc}	w_t
L	489.2 ± 2.7 (500)	626.0 ± 4.2 (645)	2979.0 ± 5.6 (3000)	2549.2 ± 22.9 (2600)	25.1 ± 3.5 (45)
W	777.7 ± 1.5 (780)	643.6 ± 2.9 (660)	2980.4 ± 4.9 (3000)	1489.5 ± 20.9 (1500)	26.0 ± 2.8 (45)
B	492.6 ± 4.5 (500)	486.9 ± 2.3 (500)	2983.3 ± 10.2 (3000)	1581.3 ± 13.0 (1600)	20.1 ± 3.2 (45)
	d_1	d_2			
d	10.3 ± 0.3 (160)	2.8 ± 0.1 (40)			
D	547.7 ± 4.9 (580)	144.3 ± 4.7 (160)			
s	76.6 ± 0.1 (60)	8.2 ± 0.9 (20)			
S	289.7 ± 7.2 (266)	39.9 ± 2.1 (54)			

Figure D.5: VLM performance characterization by Silva et al.[5]

Table 3.4: List of selected thrusters. Test 1 is the mechanical test, test 2 is the electrical test, and test 3 is the operational test. The codes are presented according to the description given in Table 3.3

Thruster	Code	Test 1	Test 2	Test 3	Detail
1	00-LD1-01	×	×		no inlet
2	00-Ld1-01	×	×		no inlet
3	00-WD2-01	×	×		no inlet
4	00-Bd2-01	×	×		no inlet
5	01-LS1-01	×	×	×	
6	01-BD1-01	×	×		nozzle blocked
7	01-BS2-01	×	×	×	
8	01-WS2-01	×	×		nozzle blocked
9	01-Ld1-01	×	×	×	
10	01-WD2-01	×	×	×	
11	01-Ws1-01	×			
12	01-Bs2-01	×			

Figure D.6: VLM mechanical characterization by Silva et al.[5] showing failed fabrication

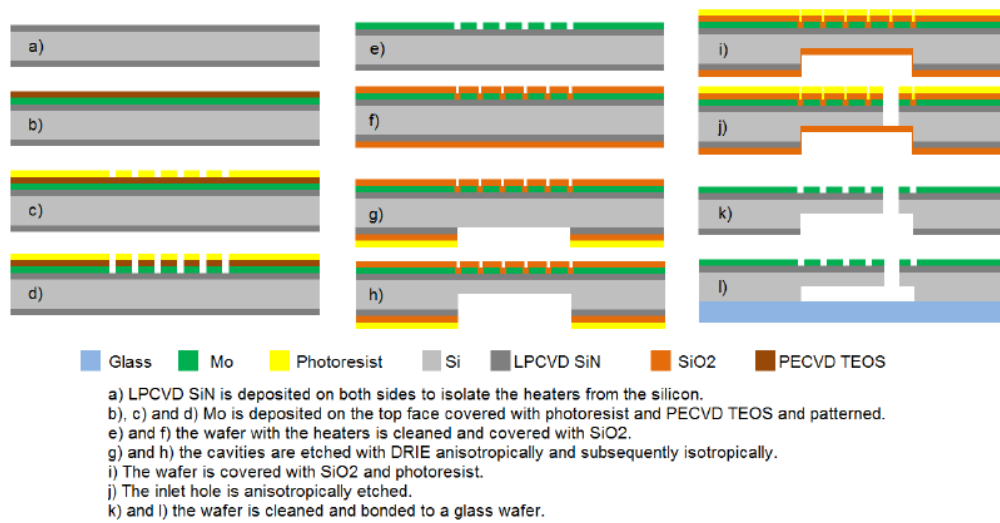


Figure D.7: VLM fabrication process overview for Silva et al. [5]